Influence of Nozzle Material and Spray Parameters on Pure Aluminum and Aluminum 7075 coatings using Cold Gas Dynamic Spray

By
Samuel Leblanc Robert

Thesis submitted to the Department of Mechanical Engineering in
conformity with the requirements for the degree of
Master in Applied Science (Engineering)

University of Ottawa

Ottawa, Ontario, Canada
April 20th, 2016

Abstract

Commercial airplanes are still using aluminum alloys as their primary structural material. Even if the used carbon fiber reinforced polymers is becoming more popular due to their extremely high strength to weight ratio, the majority of the existing flying fleet is still made out of aluminum alloys. This material was primarily used due to its high strength to weight ratio, ease to machine, excellent corrosion resistance properties and its high crash energy absorption. Aircraft components made of aluminum alloys are subjected to high stresses and harsh environments during flight, potentially leading them to crack and/or corrode. Presently, there is no industrial approved method to repair these components. Recycling damaged aircraft parts by repairing them would result in large cost savings for the industry.

The present study was motivated by the potential use of the cold gas dynamic spray (CGDS) process to repair damaged aluminum 7075-T6 aircraft components. Two feedstock materials were used to repair this alloy in this research: pure aluminum and aluminum 7075. Pure aluminum is used in the aircraft industry on non-bearing components due to its extremely high corrosion resistance properties. Aluminum 7075 is the material of choice for structural applications due to its high strength.

The results of this study show that CGDS could be potentially used to repair aluminum components on aircrafts. However, this research demonstrated that new commercially available equipments need to be further developed to successfully produce repaired components that meet the industry standards.

Acknowledgements

I would like to take a brief moment to tank my supervisor, Dr. Bertrand Jodoin for helping me to achieve my master degree at the University of Ottawa Cold Spray Lab. Thanks for the weekly meeting that helped me guiding my research project as well as expending my knowledge. It has been an honor working with you and your reputed cold spray team.

I would like to thank Dr. Mohammed Yandouzi his patience and leadership with all the training sessions you offered. You were always available for help and guidance and it has been a grateful experience working with you.

I would like to thank also the entire cold spray lab for helping me throughout my master degree: Dr. Antoine Bacciochini, Yannick Cormier, Philippe Dupuis, Daniel MacDonald, Ruben Fernandez, Patrick Trahan, Guillaume Archambault, Daniel Cormier, Leon Guo, Tyler Samson, Aleksandra Nastic and Eugeniu Celac. I have learnt so much working with all of you.

I would to thank all the machinists for your hard work and friendship. Thanks to John Perrins for the helpful trainings.

Finalement, j'aimerais remercier mes parents, ma chère sœur et tous mes amis. Merci pour tous les encouragements, je ne serais jamais où je suis sans vous.

Table of Contents

List of Tables

List of Figures

1. Introduction

1.1. Background

The aerospace industry is growing at a fast pace and aircrafts manufacturers consistently keep improving the performance of their airplanes in order to reduce their operating costs. Aircrafts have become extremely sophisticated and a lot more importance are given to details these days in order to get the edge over competitors [1]. A field that has been lagging in development is the restoration of damaged parts on airplanes. These gigantic flying mechanical devices are subjected to high structural and aerodynamic loads during their life. They are also exposed to rough environmental conditions that can enhance corrosion formation. These circumstances eventually lead to damaged parts on aircrafts and result in high replacement costs. The aerospace industry has shown interest in several methods used to restore damaged aircraft parts. Some of these methods include plasma spray, HVOF (high velocity oxyfuel) or electric arc spray [2].

Even if aircraft manufacturers are slowly replacing aluminum for carbon fibers reinforced polymer (CFRP) parts, the vast majority of commercial airplanes currently in service are mostly made out of aluminum alloys. Aluminum alloys have been the primary material for structural components for more than 80 years due to their relatively low cost, high strength to weight ratio and ease to be manufactured [3]. Figure 1.1 shows the proportion of weight of structural materials in few commercial aircrafts.

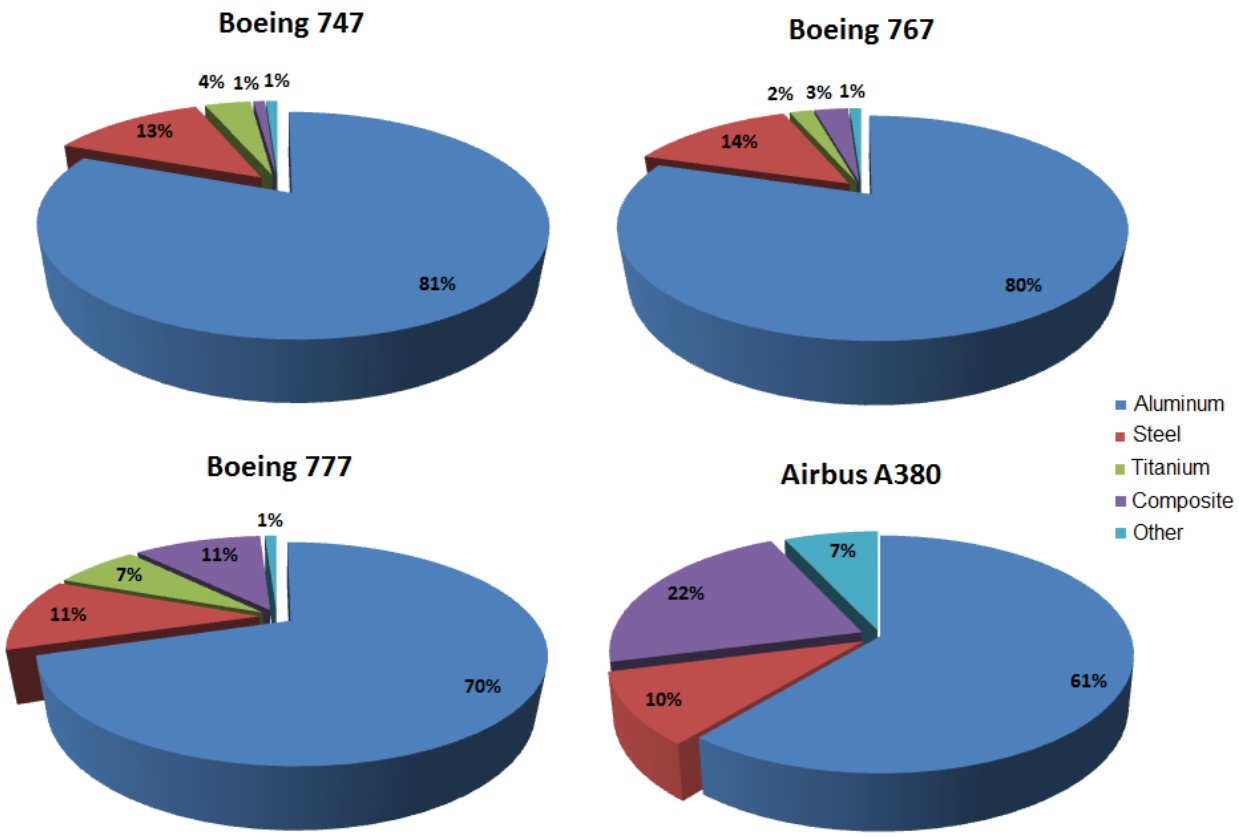

Figure 1.1: Proportion of weight of structural materials in commercial aircrafts (adapted from [4])

It is observed that aluminum is still widely used for structural components on aircrafts. As such, the restoration of damaged aluminum parts is important for airplane manufacturers.

One of the methods investigated to perform the restoration of damaged parts it the cold gas dynamic spray process (CGDS). This process consists in accelerating metallic particles (ranging from 1 to 50 μm typically) to high velocities and produce coatings. A pressurized gas expands in a converging/diverging nozzle to reach supersonic speed. The particles are injected in the gas stream to be accelerated. Particles gain high kinetic

energy in the process. When they hit the substrate to be coated, they deform and adhere to the surface [5]. The process will be discussed in more details in chapter 2. The purpose of the coating is to protect a surface from wear, oxidation and corrosion or to restore cracks and missing material.

1.2. Objectives and Problem Description

The present study was driven by the potential of the CGDS process to be used as a revolutionary method to repair damaged metallic components. The main research objective is to develop pure aluminum and aluminum 7075 coatings with high mechanical properties to successfully repair aluminum 7075 aircrafts' components. It is to be mentioned that pure aluminum is mainly used to restore the geometry of non-bearing parts as well as providing great corrosion protection and wear resistance properties (when anodized). Particularly in this industry, any micro fractures or small defect located in a component is detrimental. CGDS process could restore these components to avoid throwing them away. Although, in the past years, many studies have demonstrated the feasibility of CGDS in manufacturing pure aluminum and aluminum alloys coatings, mechanical properties still have to be improved in order to meet industry standards.

1.3. Arrangement of the Thesis

This thesis is arranged in six chapters. Chapter 1 presents general information on the research project as well as a brief background leading to objectives and problem description.

Chapter 2 provides a relevant literature review on the aluminum alloys used in the aerospace industry, the thermal spray processes and a detailed section on the CGSD process.

A detailed description of the research objectives is presented in Chapter 3. This section includes the work previously completed for this project as well as new goals to improve previous unsuccessful results.

Chapter 4 describes the experimental research approach and the equipment used throughout the project.

Chapter 5 provides results of the feasibility study using the new CGDS SST-EP system. It presents the parameters used to develop the coatings as well as the tests and standards used to qualified the repairs.

Chapter 6 details the investigation of the nozzle material. It also provides the experimental tests and results that validate the final theory.

Chapter 7 provides a general discussion of the results obtained in Chapter 5 and Chapter 6. It also presents the future work that should be undertaken.

2. Literature Review

2.1. Preamble

Chapter 2 provides a review of the relevant literature for this research project. First, it details the aluminum alloys used in the aerospace industry. It shows the different treatments that can be perform on aluminum alloys to improve their mechanical properties. The second section will discuss about the principal thermal spray processes used to produce aeronautic coatings and finally the last sections will provide a detailed analysis of the CGDS process. The gas dynamic involved in the CGDS process will be discussed as well as particle critical velocity and the bonding mechanism.

2.2. Aluminum in the Aerospace Industry

2.2.1. Introduction

Aluminum alloys are widely used in the manufacturing of aircrafts as discussed in the previous chapter. Their high strength to weight ratio and high corrosion resistant properties make aluminum alloys the preferred structural material on commercial airplanes. These days, the industry seems to opt for even higher strength to weight ratio materials like carbon fiber reinforced composite. For instance, approximately 50% of the Boeing 787 Dreamliner structural components are made of composite materials. By reducing the aircraft's weight, a smaller force is needed to keep it flying in the air (lift force). Airfoils size can be reduced resulting in less drag on the plane. By reducing the drag on the plane, less trust is required to maintain the aircraft's cruising speed. This results in a more efficient airplane to operate [6].

The main advantages of aluminum alloys over titanium and carbon fiber reinforced composites are their lower cost and manufacturing (for instance machining) fee. Figure 2.1 shows a comparison of aerospace materials strength with respect to their density.

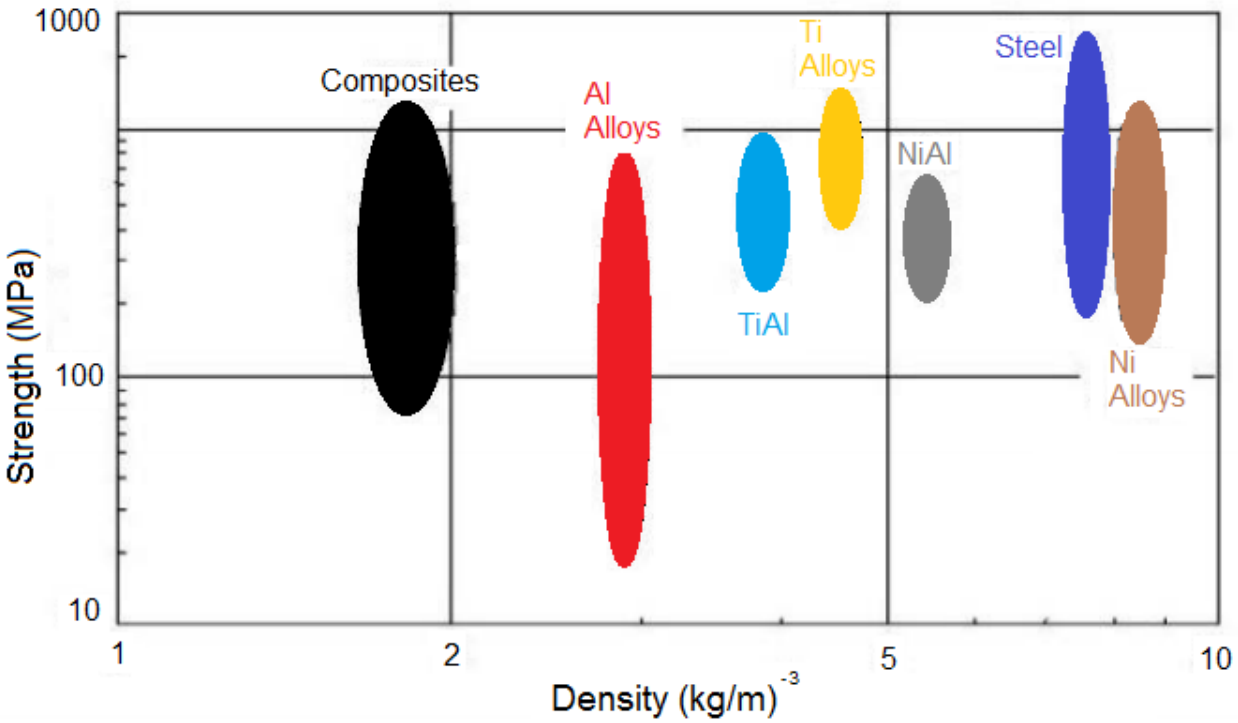

Figure 2.1: Strength with respect to density of commonly used aerospace material (adapted from [7])

It is observed that by dividing the strength of aluminum alloys (like 7075-T6) and titanium alloys by their density, comparable values are obtained. However, the low melting temperature of aluminum can restrict its application. Fiber reinforced composites have the highest strength to weight ratio as mentioned previously. This is one of the main reason modern aircrafts have their structural components built out of fiber reinforced composites.

2.2.2. Aluminum and its Alloys

Aluminum and its alloys are defined by a low density (2.7 g/cm^3) and are corrosion resistant in common environments [8]. These environments include both atmospheric and marine conditions as well as fresh water. Aluminum and its alloys are corrosion resistant due to the formation of a passive oxide film when exposed to a neutral range of pH. The thickness of the oxide layer is below 10 nm but can be increased through anodization process [9].

The mechanical properties of aluminum can be improved by cold working or alloying which consists of modifying the microstructure of aluminum by adding alloying elements such as copper, magnesium, silicon, manganese and zinc. These processes tend to reduce the corrosion resistance properties of aluminum. Table 2.1 shows the compositions and mechanical properties of common aluminum alloys.

Table 2.1: Compositions and Mechanical Properties for Common Aluminum Alloys (Adapted from [8], [10], [11])

Aluminum Association Number	*Composition (wt%)*	*Condition (Temper Designation)*	*Tensile Strength (MPa)*	*Yield Strength (MPa)*	*Ductility (%EL in 50mm bar)*
Pure Aluminum	Min 99.0 Al	Annealed (O)	69 to 186	7-11	11-12
3003	0.12 Cu,1.2 Mn, 0.1Zn	Annealed (O)	110	40	30-40
5052	2.5 Mg, 0.25 Cr	Strain hardened (H32)	230	195	12-18
2024	4.4 Cu, 1.5 Mg, 0.6 Mn	Heat treated (T4)	470	325	20
6061	1.0 Mg, 0.6 Si, 0.3 Cu, , 0.2 Cr	Heat treated (T4)	240	145	22-25
7075	5.6 Zn, 2.5 Mg, 1.6 Cu, 0.23 Cr	Heat treatment (T6)	570	505	11

It is observed that alloying elements change the mechanical properties of aluminum. It is to be noted that pure aluminum is mostly used to produce protective coatings due to its high corrosion resistant property. Aluminum 6061 is one of the most common alloys on the market. It is used to manufacture railroads, pipelines or automobiles. Aluminum 7075 and 2024 are the major aluminum alloys used in the aerospace industry. Their high specific strength is ideal for structural components [8],[12].

2.2.3. Heat Treatments of Aluminum Alloys

The mechanical properties of aluminum can be improved by precipitation hardening. This technique consists in the formation of small uniformly dispersed particles of a second phase within the original matrix. This is completed by phase transformations that are induced by specific heat treatments. Some aluminum series are non-heat-treatable like (1xxx) series, (3xxx) series, (4xxx) series and (5xxx) series. Another way to modify the microstructure of aluminum and changing its mechanical properties is by applying solid-solution strengthening and cold working [8]. Table 2.2 shows the suffix used to indicate the treatment condition of the aluminum alloys.

Table 2.2: Temper designations for aluminum alloys (adapted from [11])

Suffix Letter and digit	***Designation***
F	As-fabricated
O	Annealed-wrought products only
H	Cold worked, strain hardened
W	Solution heat treated
T1	Cooled from an elevated-temperature shaping operation + natural aged
T2	Cooled from an elevated-temperature shaping operation + cold worked + natural aged
T3	Solution treated + cold worked + natural aged
T4	Solution treated + natural aged
T5	Cooled from an elevated-temperature shaping operation + artificial aged
T6	Solution treated + artificial aged
T7	Solution treated + overaged
T8	Solution treated + cold worked + artificial aged
T9	Solution treated + artificial aged + cold worked
T10	Cooled from an elevated-temperature shaping operation + cold worked + artificial aged

(2xxx) series, (6xxx) series, (7xxx) series and (8xxx) series are heat treatable aluminum alloys. Different mechanical properties can be obtained by using specific heat treatments. For example, aluminum 7075 that is subjected to a T6 treatment is heated to 480°C and rapidly cooled upon quenching in a solid solution treatment (W). The solid solution is then rapidly aged at 120°C for 24 hours to grow precipitates in the aluminum grain structure. The precipitates in the grain boundary increase the mechanical properties of the resulting aluminum alloy.

Figure 2.2 shows the effect of precipitation heat treating on aluminum 7075 and 2024 mechanical properties.

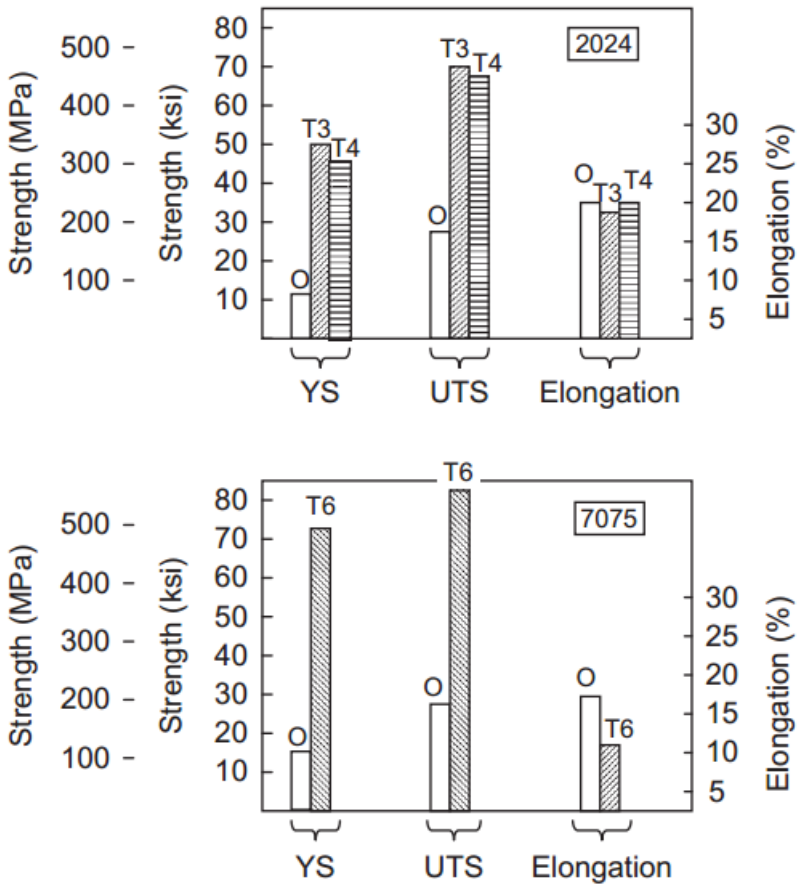

Figure 2.2: Effect of heat treatments on aluminum 2024 and 7075 [11]

2.2.4. Anodizing Process

The aerospace's demand on components' surface finish keeps increasing. The oxide layer formed with the anodizing process provides high corrosion and abrasion resistance and is therefore used widely in the aeronautic industry [13].

The process consists on using electrical current flowing through an electrolytic solution in which aluminum acts as the anode and carbon as the cathode. Hydrogen is released at the cathode and oxygen is released at the surface of the anode creating the build-up of aluminum oxide. The acid dissolves the oxide layer creating nanopores. These pores allow the electrolytic solution to reach the aluminum substrate and continue growing the coating (aluminum oxide film) to greater thickness. The schematic of the process is showed in Figure 2.3.

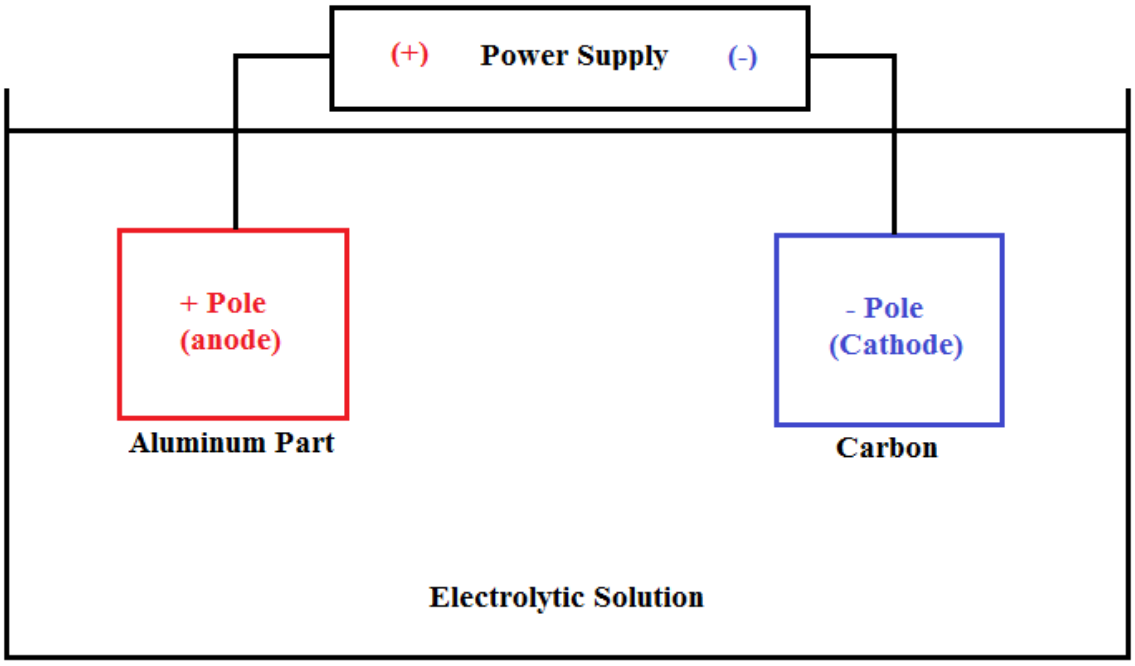

Figure 2.3: Schematic of the anodizing process for an aluminum component

Few methods are used, each using a different source of electrolyte and operation parameters. These parameters influence de properties of the oxide film formed on the component [14], [15].

The three most important electrolytes are the chromic acid, sulfuric acid ad phosphoric acid. Chromic acid is utilized mostly for structural joints protection. It provides excellent corrosion protection mostly due to denser and softer oxide film formed. This process however produces a light opaque gray oxide layer that can be easily damaged.

Sulfuric acid anodizing is divided in two categories: Type II coatings for decorative purposes and Type III coatings for engineering applications. Type III, also known as hard coat oxide film, produces a hard film that is property dependant to each aluminum alloy.

Phosphoric acid anodizing is the third most popular anodizing process. It is known for its structural adhesive bonding property in humid environments. The morphology of the oxide film gives its adhesive characteristic. It produces a film of pores with whiskers on the top surface [13], [16].

2.3. Thermal Spray Processes

Thermal spray processes are a group of technologies used to produce coatings. The aerospace industry is using these technologies to produce a wide variety of protective layers on aircraft's components. New applications for thermal spray processes have

been investigated in recent years. One of these applications is the restoration of damaged/corroded parts on aircrafts using CGDS. A review of the main thermal spray processes used in the aerospace industry is presented in this section as well as a detailed description of the CGDS process.

Thermal spray processes have in common the use of a concentrated source of heat to melt or soften feedstock materials while accelerating them towards a substrate. When high energy particles hit a substrate, they rapidly deform and solidify. A coating builds up as subsequent particles hit the surface. Particles are accelerated in a similar way in each process. It usually consists of injecting the feedstock material in a gas stream before or after it has traveled through a nozzle. Thermal spray processes are characterized by their particle velocity and operating temperature [17].

The main difference between each thermal spray process is their source of energy to generate heat. Thermal energy can be generated from a chemical reaction, for example the combustion of fuels with oxygen or from electrical energy. Radiofrequency (RF) plasma torches are also used to generate heat by imposing an RF field onto the gas stream. This process is plasma spray (Other types of plasma torches are available) [5]. Different thermal spray processes have been classified in different categories according to their way to generate thermal energy. The following paragraphs describe in further details the particularities of each thermal spray process. Figure 2.4 shows the large family of thermal spray processes and their particularities. It is to be noted that kinetic

spraying does not use heat to melt or soften feedstock materials. It is nevertheless considered a thermal spray process [5],[18].

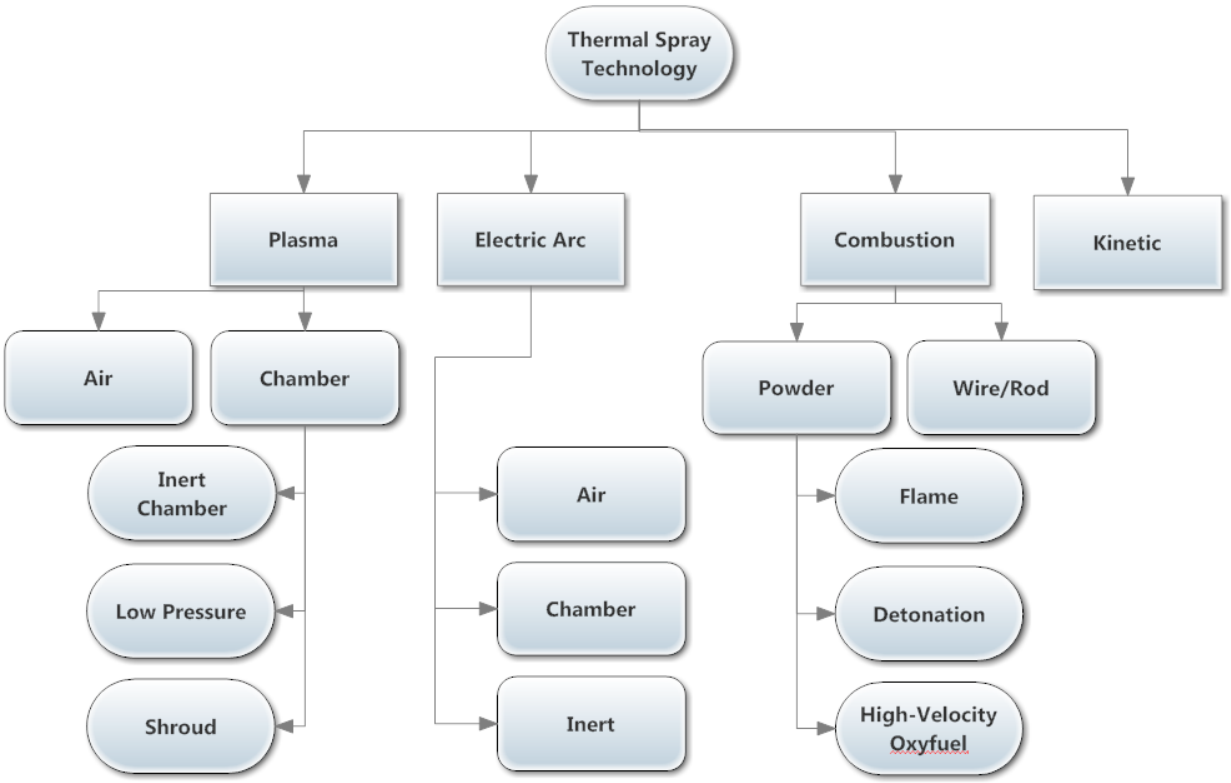

Figure 2.4: Thermal spray processes (adapted from [5])

2.3.1. Plasma Spraying

A plasma is created by transferring enough energy to a gas to induce its ionization. When the energy input is removed, the electrons and ions merge together again to release light and heat. Energy sources commonly used in plasma spray are direct current (DC), radiofrequency (RF) microwaves or alternating current (AC) [19].

Direct current plasma spray is one of the most common plasma spray process due to its extremely high temperature generated. It allows a large variety of material to be sprayed effectively [20]. Figure 2.5 shows the cross-section of a typical plasma spray torch. DC

plasma arc involves typically a tungsten cathode axially aligned with a copper anode. The really high flame temperature of plasma spray (5000 - 25000°C [18]) allows high melting point materials, like ceramics, to be deposited. However, an intensive water cooling system has to pass through the gun to avoid damaging its components. Feedstock material is usually injected in the plasma jet after it has passed through a converging or converging-diverging nozzle. The molten particles are accelerated by the gas until they hit the substrate (particle velocity ranging from 80 to 300 m/s).

Different environments are used for plasma spray. The most economical and commonly used is Air-Plasma spraying. However, it is possible to spray in a controlled environment (chamber) surrounded by inert gases to reduce formation of oxides in coatings [5].

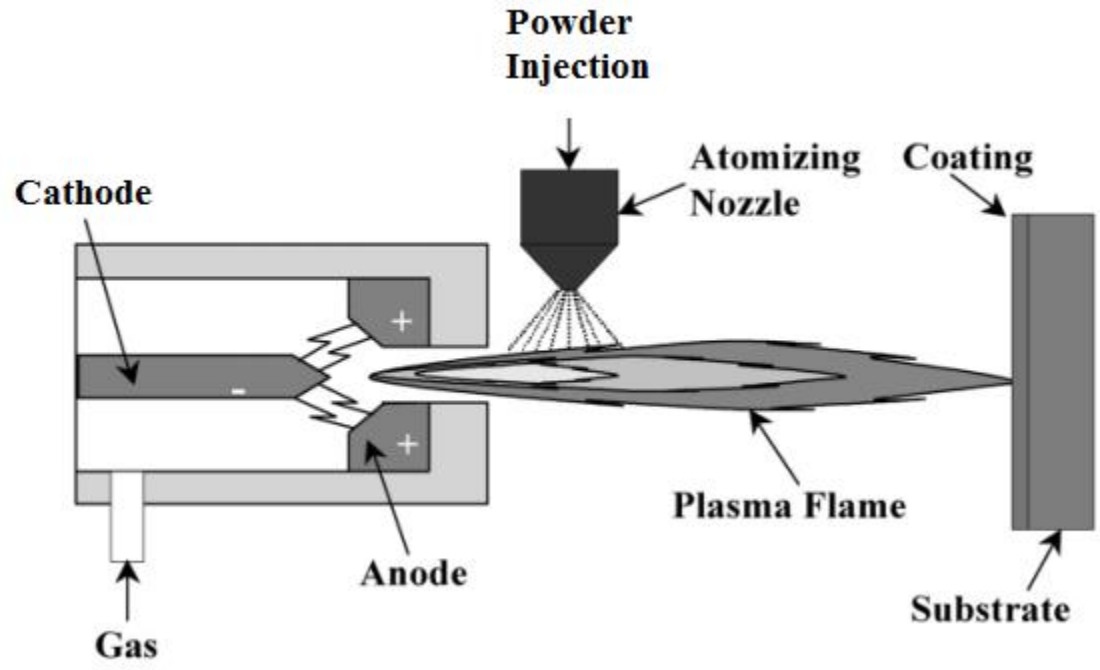

Figure 2.5: Schematic of a standard plasma spray torch [21]

2.3.2. Electric-Arc Spraying

This process consists of running direct current in two consumable wires in order to form an electric arc in the gap separating them (as seen in Figure 2.6). Simultaneously, a high-velocity gas jet is flowing through the arc to atomize the molten particles and accelerate them towards the substrate [22]. The particles hit the substrate with high thermal and kinetic energy, deform and solidify to produce coatings. The efficiency of this process is higher than other thermal spray processes due to the wires being melted directly by the arc. This characteristic results in the substrate to be located closer to the gun than in other processes because the particles start cooling down right after they leave the electric-arc zone. The variety of materials that can be sprayed efficiently is usually limited to metals due to the flame temperature of the process (3000-6000°C [18]) and also due to the necessity of the feeding conductive wire materials [5].

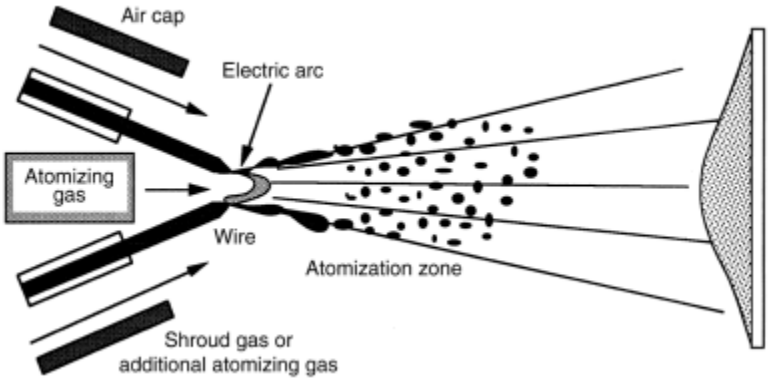

Figure 2.6: Schematic of the electric-arc spraying process [5]

2.3.3. Combustion Spray (High-Velocity Oxyfuel Spray)

High-Velocity Oxyfuel Spray (HVOF) process is characterised by the burning of fuel mixed with oxygen in a confined combustion chamber (shown in Figure 2.7). The combustion product gases have high energy and are used to heat up and accelerate feedstock materials injected behind the torch. The mixture passes through a nozzle that accelerates the particles to high velocities (400-800 m/s [18]) towards a substrate. Upon impact, the particles deform, spread out and bond to the surface upon solidification [23].

The flame temperature (around 3000°C) of HVOF combined with high particle impact velocity allows hard material to be deposited and produces dense coatings. These coatings also exhibits higher bond strength than other coatings produced with other thermal spray processes [5], [24].

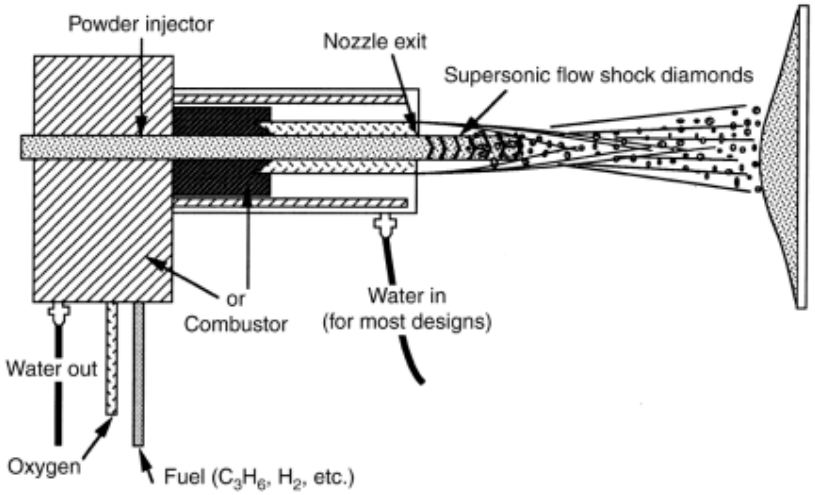

Figure 2.7: Schematic of HVOF process [5]

2.3.4. Kinetic Spraying

There are four main type of kinetic spraying process; kinetic powder deposition, kinetic spraying, high-velocity powder deposition and Cold Gas Dynamic Spraying (CGDS). Kinetic spraying is considered as part of thermal spray processes even though heat is not used to melt or soften feedstock materials. Heat is rather utilized to increase the driver gas stagnation temperature (up to 1100°C). The driver gas rapidly expands through a de Laval nozzle and accelerates to supersonic speeds. The gas temperature drops drastically as its velocity increases. Powder is injected in the cold gas jet, minimizing heat transfer to it. Particles reach high velocities, typically between 300 to 1200 m/s. [5], [25]. The CGDS process will be discussed in details in the following section.

2.4. Cold Gas Dynamic Spraying

The following section presents the CGDS process and its characteristics. This section includes the historical background of the process, an overview of the particles - substrate bonding mechanisms, the particles critical velocity theory and the gas dynamic principle of CGDS.

2.4.1. Historical Background

Cold Gas Dynamic Spraying (CGDS) was discovered in the mid-1980s by Professor Anatolii Papyrin and his colleagues at the Institute of Theoretical and Applied Mechanics of the Siberian division of the Russian Academy of Science in Novosibirsk. The group of scientists were conducting a study on models subjected to a supersonic

two-phase flow (gas and solid particles) in a wind tunnel. They noticed that certain materials were depositing on the models instead of eroding it. Afterward, they demonstrated the feasibility of the CGDS coating process resulting in development of the method, technologies and equipment [26]. Moreover, the gas dynamics involve in CGDS has been studied extensively to help researchers having a better understanding of the process. Advances in CGDS led to a US patent in 1994 and a European patent in 1995 [27]. Since then, companies have shown interest in the technology resulting in the development of new research centers and new equipment providers around the world [23], [28]. In the last decade, the cold spray technology has grown exponentially and led to a large amount of information available in a short period of time [29]. Nowadays, thousands of scientific papers can be found on very detailed characteristics of the process. Researchers have showed the feasibility of depositing various materials by CGDS and it keeps growing every year.

2.4.2. Process Overview

Figure 2.8 shows a schematic of a typical cold-spray system. This innovative technology uses a high-pressure gas supply to produce a supersonic driving gas flow. Powder is injected in the flow to be accelerated towards the substrate to produce a coating. It is to be noted that the driving gas flow can be heated with the assistance of an electric gas heater to a temperature up to 1100°C [5]. Thermal energy is added to the driving gas prior to its expansion. The energy in converted in kinetic energy and high gas velocity is reached at the nozzle exit. This characteristic differentiates CGDS from other thermal spray processes where thermal energy is mainly used to soften or melt particles. In

CGDS, a supersonic flow is generated after the driving gas pass through a converging/diverging de-Laval type nozzle [30].

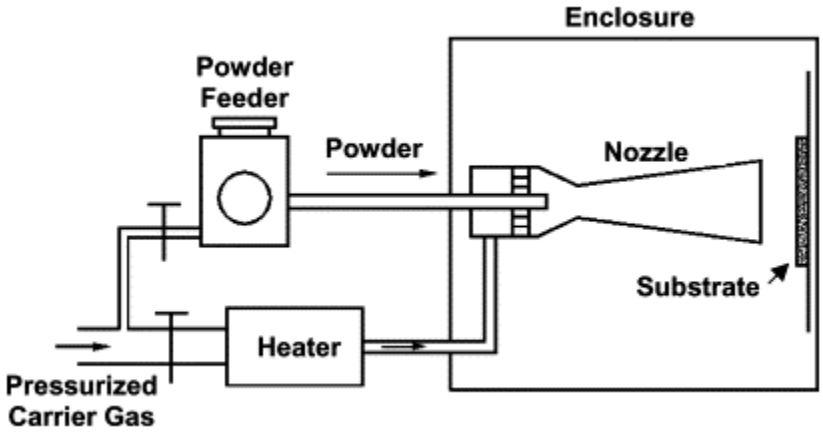

Figure 2.8: Schematic of a typical cold-spray system [31]

A coating is achieved by injecting powder in the driving gas, before or after the nozzle`s throat, allowing particles to gain enough kinetic energy to plastically deform when they hit the substrate. Various parameters can affect the particles velocity and therefore coatings microstructures. These parameters will be discussed in further details in the next chapter [32].

2.4.3. Critical Velocity

The CGDS process relies on high-velocity particles to deform, adhere and create coatings. However, it has been shown that deposition only occurs if the impact velocity of the particles surpasses the critical velocity, unique to each material. Figure 2.9 represents the correlation between the particles velocity and the deposition efficiency (DE) for a certain impact temperature. It is to be noted that the deposition efficiency is

defined as mass of the feedstock material deposited on the substrate over the mass of the feedstock material consumed.

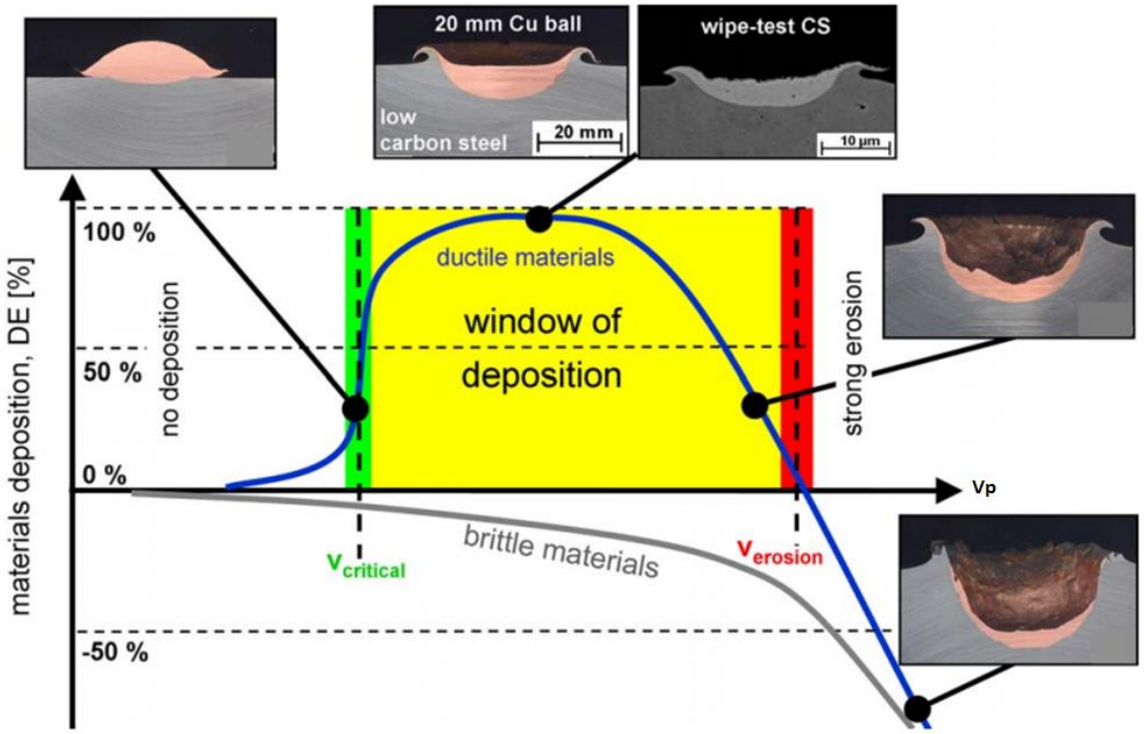

Figure 2.9: Schematic correlation between the particle velocity and DE(%) [33]

It also shows a simulation of a 20 mm spherical copper (Cu) particle hitting a steel substrate at different velocities. It can be observed that deposition occurs when the particles reach the critical velocity and the DE increases until the particle velocity reaches the saturation limit. Afterwards, the DE decreases with particle velocity due to erosive effects. Moreover, when a certain erosion velocity is reached, deposition stops occurring while particles keep eroding the substrate. Brittle materials are usually avoided in cold spray because they don't deform to adhere to the surface. Their melting temperature is also never reached in the process preventing them from sticking to the substrate. These materials tend to erode the surface at any given velocity [34].

Table 2.3 shows the experimental values of critical velocity for diverse materials. It is to be noted that the critical velocity does not directly correlate with the melting temperature of the material. Copper for instance has a much higher melting temperature than aluminum, but requires less kinetic energy to produce a coating. It is rather the result of the interaction between the material strength and the heat generation caused by plastic deformation that affects the critical velocity.

Table 2.3 : Experimentally evaluated values of critical velocity for various metallic materials (adapted from [33])

Material	*Melting Point (°C)*	*Critical Velocity (m/s)*
Aluminum	660	620-660
Titanium	1670	700-890
Tin	232	160-180
Zinc	420	360-380
Stainless steel (316L)	1400	700-750
Copper	1084	460-500
Nickel	1455	610-680
Tantalum	2996	490-650

Equation (2.1) presents a simple energy-balance relationship:

$$C_p(T_m - T) + L = \frac{1}{2} v_m^2 \quad \textbf{(2.1)}$$

where T_m is the melting temperature of the material, T is the impact temperature, L is the latent heat of fusion and v_m is the velocity that cause complete melting of the particle

("melting" velocity) under the assumption of T = 25°C. Figure 2.10 shows the correlation between the "melting" velocity and the critical velocity of certain materials.

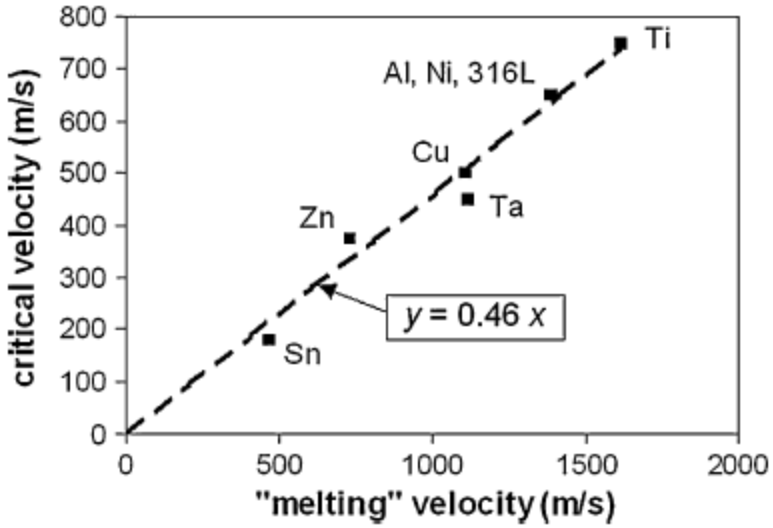

Figure 2.10: Correlation between the critical velocity and melting velocity [33]

It is observed that the critical velocity is almost half its "melting" velocity. This reveals that the kinetic energy required for bonding is not even close to melt an impinging particle [33].

The reason particles adhere to a surface was not explained in the previous chapter. This topic will be explicated in detail after reviewing the gas dynamics involved in CGDS.

2.4.4. Gas Dynamics in CGDS

A major factor influencing the CGDS process is the behavior of the driving gas throughout the process. A strong understanding of the gas dynamics involved in the process is therefore mandatory in order to optimize the CGDS system output. This section will present proper assumptions, compressible flow concepts, , gas stagnation properties and gas flowing in a converging/diverging nozzle.

2.4.4.1. Assumptions for Gas Dynamics Principles

CGDS has been the focus of multiple studies in the last the decade that conducted to a much better understanding of the process. Assumptions are used to simplify the complex fluid mechanics involved in the process. First, the flow is assumed to be one-dimensional meaning that the gas properties remain the same throughout the cross-section in the nozzle. Moreover, inert gases, like nitrogen and helium, are used in the process and can be assumed as calorically perfect gases. These gases have negligible intermolecular forces and the specific heat is assumed to be constant ($E=C_vT$ and $h=C_pT$). The flow is also assumed to be adiabatic, neglecting heat losses through the nozzle and progressing at a steady-state. It is also considered to be inviscid meaning that the viscous forces are neglected in the nozzle resulting in reversible gas expansion. In thermodynamics, adiabatic and reversible systems are considered isentropic. This simplifies calculations while maintaining a reasonable margin of error between theoretical and experimental results.

2.4.4.2. Compressible Flow Concepts

The analysis of compressible flows is complex and can be counter intuitive. First of all, sound is produced when molecules in a certain medium collide and transfer energy to each other. Infinitesimal pressure waves are induced and propagate at a certain velocity. Energy propagates through the wave causing a variation in pressure, density and temperature. These pressure waves travel through a medium at the speed of sound *c.* This property is important when analyzing compressible flows. Figure 2.11 shows the schematic of a pressure wave propagating through an arbitrary medium where *c* is the velocity, p is the pressure, *ρ* is the density and T is the temperature.

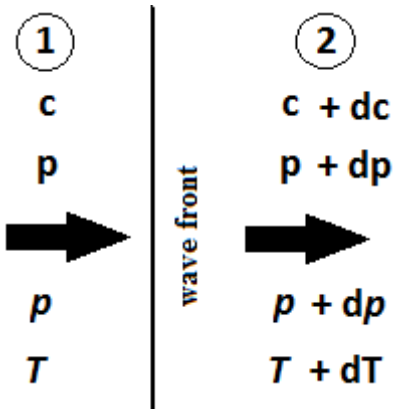

Figure 2.11 : Schematic of a sound wave (adapted from [35])

From the equation of the conservation of momentum, the following equations can be obtained:

$$c = -\rho \frac{dc}{d\rho} \tag{2.2}$$

and

$$c^2 = \frac{dP}{d\rho} \tag{2.3}$$

It can be observed from these equations that the speed of sound *c* is directly related to the rate of change of pressure with respect to density. A large change in pressure is therefore required to increase the density of fluids with high speed of sound. Equation (2.3) can be reworked for the case of a calorically perfect gas undergoing an isentropic evolution:

$$c = \sqrt{kR_sT} \tag{2.4}$$

where *k* is the gas specific heat ratio (C_p/C_v), R_s is the specific gas constant and T is the medium temperature. R_s is obtained by dividing the molar mass constant *R* by the molar mass of the fluid *M*. Equation (2.4) shows that sound travels at a faster rate in fluids with low molar weight. It also demonstrates that for a certain medium, the speed of sound is a function of the local temperature only. Table 2.4 represents the speed of sound of few different gases at standard atmospheric condition.

Table 2.4: Speed of sound of different gasses under standard atmospheric condition

Gas	***Speed of sound (m/s)***
Air	346
Nitrogen	351
Helium	1016
Hydrogen	1315

The effect of the gas molar weight on its speed of sound is showed in this table. Fluids can reach a higher velocity than its speed of sound when subjected to certain nozzle designs. The Mach number *M* can be varied by changing the nozzle geometry. Further information on nozzle designs will be discussed in the following section. The Mach number is defined in equation (2.5) as the gas velocity *u* over its speed of sound *c*:

$$M = \frac{u}{c} = \frac{u}{\sqrt{kR_cT}} \quad \textbf{(2.5)}$$

The Mach number is used as a reference to characterize the flow regime. The first flow regime is defined as **subsonic** when *M*<1. This regime is defined by smooth streamlines and continuously varying properties. When M>1, the flow is considered **supersonic**. A supersonic flow that encounters an object produces normal or oblique shockwaves reducing its velocity and increasing its pressure, temperature and density. When the Mach number reaches approximately 5, these increases become severe enough to dissociate or even ionize the gas. This regime is called **hypersonic** [35]**,** [36].

2.4.4.3. Flow in a Converging/Diverging Nozzle

As discussed in section 2.4, CGDS uses a converging/diverging nozzle to accelerate the driving gas and the feedstock material. The gas velocity can reach supersonic speeds in this process by varying the cross-section of the nozzle.

By combining and simplifying (using assumptions of section 2.4.4.1) the conservation of energy, the equation of continuity, the two laws of thermodynamics and the Mach number equation, the following equation can be obtained:

$$\frac{du}{u}(1 - M^2) = -\frac{dA}{A} \quad \textbf{(2.6)}$$

where u is the gas velocity and A is the cross-section area of the nozzle. It is observed that the Mach number influences the flow velocity in two different ways. When the Mach number is lower than 1, the gas velocity increases as the cross-section area decreases.

When the Mach number is greater than 1, the opposite phenomenon occurs. Figure 2.12 shows the effect in the converging and diverging nozzles.

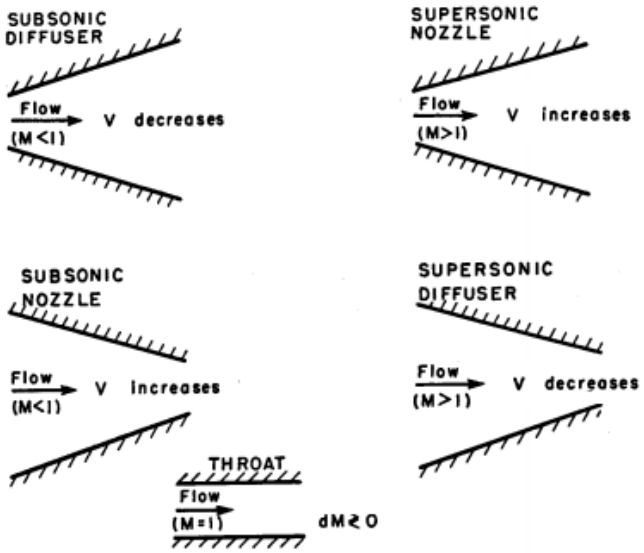

Figure 2.12: Effect of area change on velocity in subsonic and supersonic flow (adapted from [36])

It can be observed that the flow has to reach sonic speed at the nozzle throat in order to keep accelerating in the diverging section, else the flow velocity will decrease. To reach sonic speed at the throat, the gas stagnation pressure has to be high enough to get a choked flow. Stagnation properties will be discussed in more details in the following section [37].

2.4.4.4. Gas Stagnation Properties

Once the nozzle geometry is designed in CGDS, there are only two other major parameters that will influence the flow: the stagnation pressure and temperature of the gas. These parameters are defined as the temperature or pressure that would exist if the fluid elements were brought to zero velocity under isentropic conditions. Equations

(2.7) and (2.8) provide means for which the gas pressure P and temperature T can be calculated for given parameters P_0, T_0 and M at any points in the nozzle.

$$\frac{P_0}{P} = (1 + \frac{k-1}{2} M^2)^{\frac{k}{k-1}} \quad \textbf{(2.7)}$$

$$\frac{T_0}{T} = 1 + \frac{k-1}{2} M^2 \quad \textbf{(2.8)}$$

2.4.4.5. Compressible Flow in a Converging/Diverging Nozzle

Figure 2.13 shows the evolution of an isentropic flow in a converging/diverging nozzle for a certain stagnation pressure P_0 and a varying back pressure P_b.

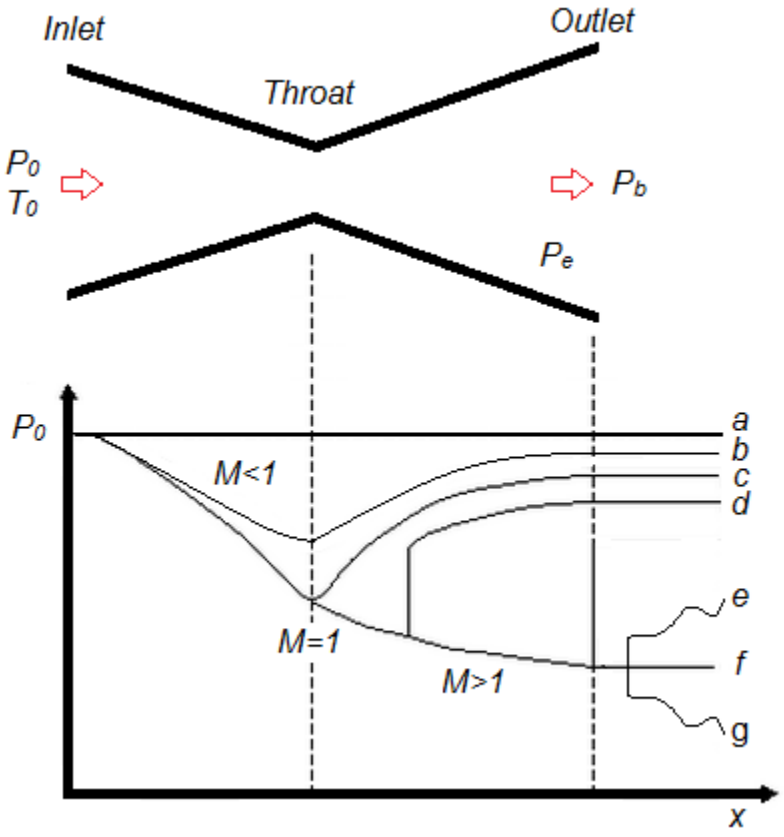

Figure 2.13: Schematic of an isentropic flow in a converging/diverging nozzle (adapted from [38])

The previous figure illustrates seven different cases that can occur in a converging/diverging nozzle. The first scenario “a” happens when the back pressure P_b is equal to the stagnation pressure P_b. The gas does not encounter any acceleration throughout the nozzle. In the second case “b”, P_b is lower than P_0, but the difference in pressure is not substantial enough to choke the flow and reach sonic speed at the throat. The gas decelerates in the diverging section of the nozzle. The third case “c” occurs when the back pressure is low enough to choke the flow at the throat and reach sonic speed. However, the pressure ratio is too low to sustain supersonic flow in the diverging section of the nozzle. Lowering the back pressure furthermore results in case “d” where the supersonic regime is reached in the diverging section. However, a shockwave occurs in the nozzle resulting in a sudden increase of pressure, temperature and density of the flow while decelerating. Previous cases would all results in a low gas exit velocity and would not be beneficial for CGDS applications. Cases “e”, “f” and “g” happen when the pressure ratio is high enough to sustain a supersonic regime throughout the diverging part of the nozzle while avoiding shockwaves inside the nozzle. Shockwaves can occur when the supersonic flow exits the nozzle if the exit pressure P_e is lower than the back pressure P_b (case “e”). This type of flow is referred to as an over-expanded flow. In an ideal nozzle design, the exit gas pressure P_e is equal to the back pressure P_b to avoid shock waves or expansion waves (case “f”). If the gas exiting the nozzle is under-expanded, expansions waves and oblique shock waves will occur in order to bring the gas pressure to the back pressure P_b. This phenomenon can be observed in Figure 2.14.

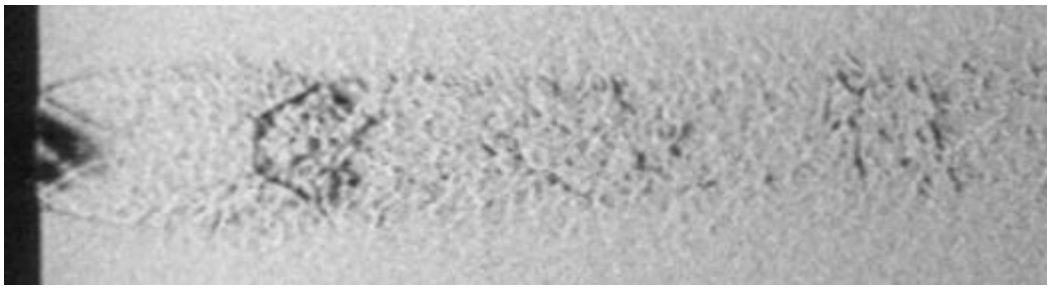

Figure 2.14: Supersonic flow exiting a nozzle [39]

2.4.4.6. Acceleration Principles of Feedstock Material in CGDS

Once the fluid dynamics involved in CGDS is understood, it is critical to analyze the interaction between the particles and the driving gas. In this process, feedstock material is accelerated by the gas stream. The drag force applied on the particles by the driving gas can be expressed by equation (2.9):

$$F_{drag} = ma = m\frac{dV_p}{dt} = mV_p\frac{dV_p}{dx} = \frac{C_d A_p \rho (V - V_p)^2}{2} \quad \textbf{(2.9)}$$

where C_d is the drag coefficient, A_p is the projected cross-section area of the particle, ρ is the gas density and V and V_p are the gas and particle velocity respectively. It is to be observed that the maximum particle velocity that can be reached is the gas velocity. Moreover, equation (2.9) can be rearranged to find the particles velocity with respect to the gas velocity:

$$V_p = V\sqrt{\frac{C_d A_p \rho x}{m}} \quad \textbf{(2.10)}$$

It is observed in equation (2.9) and (2.10) that the particle velocity is a function of the gas velocity, the gas density, the drag coefficient (related to the shape of the particle), particle cross-section area, particle mass and the length of the acceleration zone. In

CGDS, the gas stagnation temperature and pressure can be increased to raise particle velocity. The temperature increases the gas velocity and the pressure increases the gas density which results in higher particle velocity. However, by increasing the gas temperature, its density lowers. An equilibrium between both parameters have to be established to optimize particle velocity.

2.4.5. Bonding Mechanism

In CGDS, particles are accelerated at high velocity towards a substrate, deform upon impact and adhere to the surface to produce a coating. The theory of the critical velocity was previously discussed in order to identify the amount of kinetic energy required to produce a coating. Previous section also described how the CGDS process accelerates particles to such velocities. This section will present the bonding mechanisms between particles as well as the bonding mechanisms between the particles and the substrate.

The actual mechanisms by which solid state particles deform and adhere have not been completely well understood yet in CGDS. An interesting hypothesis states that plastic deformation of impacting particles breaks the surface oxide layer and provides intimate conformal contact under high local pressure, thus allowing bonding to occur [40]. It is believed that adiabatic shear instability at the interface during impact creates a metal jet between the particles and the substrate [41], [42]. Adiabatic shear instability is associated with high strain rate deformation. High strain rates caused by the high impact velocities lead the material deformation mechanism to change from plastic to viscous flow. The assumption that the interaction between particles and the substrate is

adiabatic is based on the short contact time. It is to be mentioned that adiabatic shear instability occurs at the interface when particles hit the substrate at their critical velocity. Figure 2.15 presents the evolution of an aluminum particle contacting a copper substrate and a copper particle hitting an aluminum substrate at four different times [43].

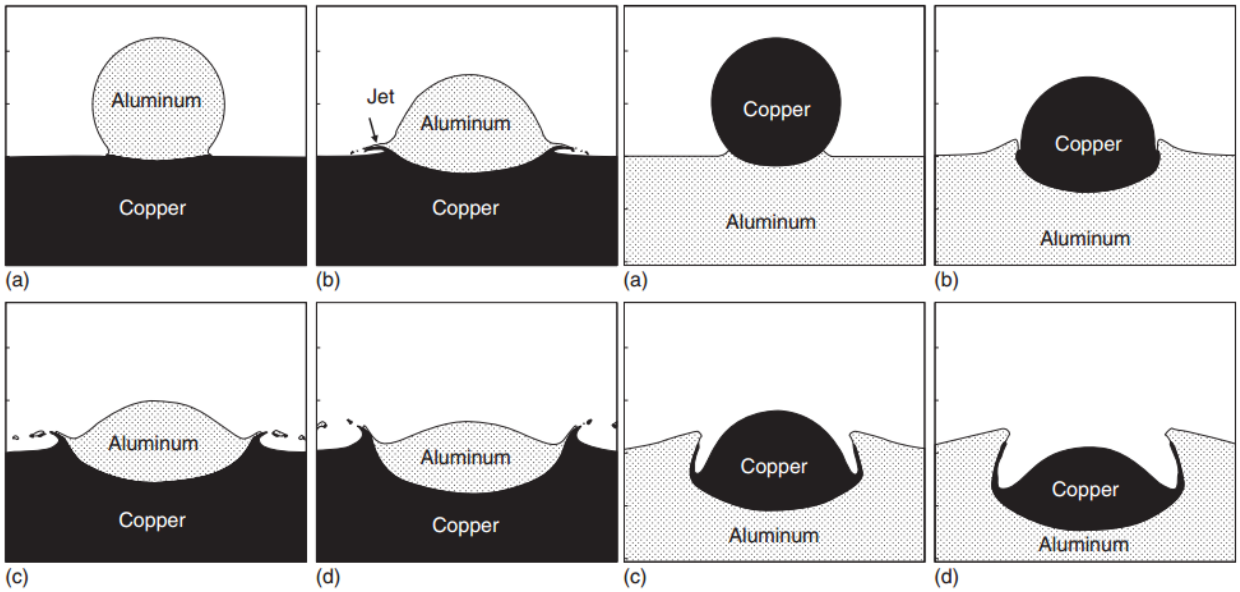

Figure 2.15: Evolution of a 20 µm diameter aluminum particle (left) and a copper particle (right) impacting a substrate at 650 m/s at the following times: (a) 5 ns; (b) 20 ns; (c) 35 ns; (d) 50 ns (adapted from [40])

The jetting effect is observed causing the particle oxide layer to break and adhere to the substrate. The copper particle penetrates further in the aluminum substrate than the aluminum particle mainly because of its higher hardness value. Figure 2.16 presents a SEM image of a copper particle after hitting a copper substrate. The measured particle velocity was ranging between 550 m/s and 670 m/s [44].

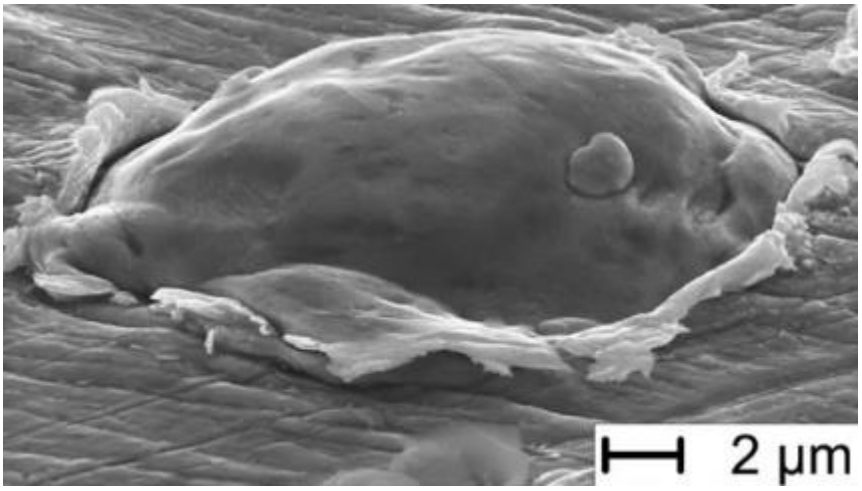

Figure 2.16: SEM image of a copper particle on a copper substrate showing substrate's jetting [44]

3. Research Objectives

3.1. Introduction

This research project started five years ago when the aerospace industry was investigating economical methods to restore damaged aluminum parts on aircrafts. Even up to today, the industry has not developed yet an efficient technique to perform this task. This deficiency results in throwing away large and expensive damaged metallic parts. Previous research projects have shown the efficiency of CGDS to fill gaps or cracks and the purpose of this research is to pursue McDonald's work [45] into verifying if these coatings can meet specific ASTM standards established by the industry. This restoration method could become industrially accepted if all standards are met.

3.2. Previous Work completed on the Project

It was showed by McDonald's previous work that coatings of pure aluminum and aluminum 7075 on aluminum 7075-T6 substrates could be produced using the industrial cold spray system (SST-P System) manufactured by Centerline (Windsor) Ltd. However, these coatings failed at meeting some of the ASTM standards specified by the aerospace company. The quality of the coatings had to be improved before being validated and used to repair aircraft parts. Table 3.1 presents the qualification plan and industry's specifications for aluminum coatings. It also shows whether the specifications were met or not.

Table 3.1: Qualification plan for Pure Aluminum and Aluminum 7075 Coatings

Standards and Specifications	***Pure Aluminum on 7075-T6***	***Aluminum 7075 on 7075-T6***
Bond Strength of 13.79 MPa (2000 psi) (ASTM C-633)	Succeeded	Succeeded
Corrosion Testing (ASTM B117)	Succeeded	Succeeded
Taber Abrasion Test (ASTM D4060)	Failed	Failed
Nitrogen as Driving Gas	Succeeded	Failed
Maintain the Heat Treatment of the Substrate	Succeeded	Succeeded

It is observed that the pure aluminum and aluminum 7075 coatings produced by McDonald [45] did not pass the Taber abrasion test. Moreover, the industry required using nitrogen as the driving gas. The use of helium was discarded due to its high cost and rarity. It is to be noted that the aluminum 7075 coatings were produced using helium as the driving gas because nitrogen did not provide acceptable deposition efficiency for the application. The spraying time required to build the coating was too extensive to prevent the temper or heat treatment condition of the substrates to be affected.

3.3. Research Goals

The goal of this thesis is to build 1 to 1.5 mm thick coatings of pure aluminum on aluminum 7075-T6 and aluminum 7075 on aluminum 7075-T6 substrates in order to meet all industry requirements. The coatings' quality will have to be improved in order to pass the Taber abrasion test (ASTM D4060-10). It was observed on Taber abrasion panels produced by MacDonald that the aluminum oxide film did not grow uniformly on the coating. MacDonald mentioned that this was caused by the high porosity in the coating. Lowering the porosity in the coatings should results in a denser and more uniform oxide layer when anodized. Moreover, the aluminum 7075 coatings will have to be produced with nitrogen as the driving gas without affecting the heat treatment of the aluminum 7075-T6 substrate. Finally, the bond strength of the improved coatings will have to be evaluated again to meet the specification (ASTM C-633).

3.4. Feasibility of Pure Aluminum and Aluminum 7075 CGDS Coatings using SST-EP System

In order to improve the quality of the coatings, a new commercial CGDS system was installed at the University of Ottawa Cold Spray Laboratory. The more powerful Centerline SST-EP system offers more features than the previous Centerline SST-P system. It is to be mentioned that McDonald's work was accomplished using the SST-P System. Table 3.2 shows a comparison between the old SST-P System and the new SST-EP System.

Table 3.2: Comparison of the SST-P system and the new SST-EP system

Features	***SST-P System***	***SST-EP System***
System Maximum Stagnation Temperature (°C)	500	500
System Maximum Stagnation Pressure (psi)	250 (1.72 MPa)	500 (3.45 MPa)
Powder Preheating (°C)	N/A	500
Nozzle	Polymer (1st gen)	Polymer (2nd gen)
Polymer Nozzle Maximum Temperature (°C)	350	500

The SST-EP system is equipped with a more powerful electric gas heater to be capable of heating denser gases (caused by a stagnation pressure of 3.45 MPa) to 500°C. Before improving the coatings quality, it was mandatory to demonstrate the feasibility of

producing pure aluminum coatings on aluminum 7075-T6 substrates and aluminum 7075 coatings on aluminum 7075-T6 substrates with the new SST-EP system.

3.5. Optimization of CGDS Parameters

Once it is shown that the new SST-EP system can produce pure aluminum and aluminum 7075 coatings on aluminum 7075-T6 substrates, multiple tests will be performed modifying spray parameters in order to optimize the quality of the coatings. This study focuses on optimizing the coating density while maintaining the heat treatment of the substrates and keeping the adhesion strength above the industry requirement (13.79 MPa). The procedure used for optimizing the CGDS parameters will be explained in details in chapter 5.

3.6. Investigation of Coatings Abrasion Resistance

McDonald [45] investigated the possibility of using aluminum coatings produced with CGDS to repair damaged parts on aircrafts. However, his work was not implemented by the industry due to poor results obtained on the Taber abrasion test (ASTM D4060-10). It was observed that the aluminum coatings produced with CGDS were not effectively forming a dense and uniform oxide layer when anodized. This defect resulted into large material loss during the Taber abrasion test. It was determined during the analysis of the anodized coatings cross-sections that the density and uniformity of the oxide layer could be improve by producing denser coatings.

4. Experimental Apparatus

4.1. Introduction

This chapter describes the equipment used to produce the various aluminum coatings. It is followed by a description of the apparatus used to prepare and analyze coatings' microstructure. Finally this chapter goes over the equipment and software used to measure particles velocity and substrate's temperature.

4.2. Low Pressure SST-EP System

The following section summarizes and describes each of the main components present in the low pressure SST-EP system manufactured by Centerline (Windsor) Ltd. These components are: the spraying chamber, the spray gun (gas heater), the nozzle, the powder feeder and the driving gas supply.

4.2.1. Spraying Chamber

One part of a CGDS system is the spraying chamber (cabinet). The function of the spraying chamber is to collect all the powder that did not adhere to the substrate. Figure Figure 4.1a shows the spray cabinet that restricts powder from contaminating the laboratory. Figure 4.1b presents the powder filter that is connected to the spray cabinet. This device is used to vent away the powder collected at the bottom of the spraying chamber and filter it with water. The main advantage of the 5000 cfm sized wet filtration system is that it traps powder in water to avoid powder to react and inflame. An EPA

filter is also located over the water reservoir to ensure particles are not released in ambient air.

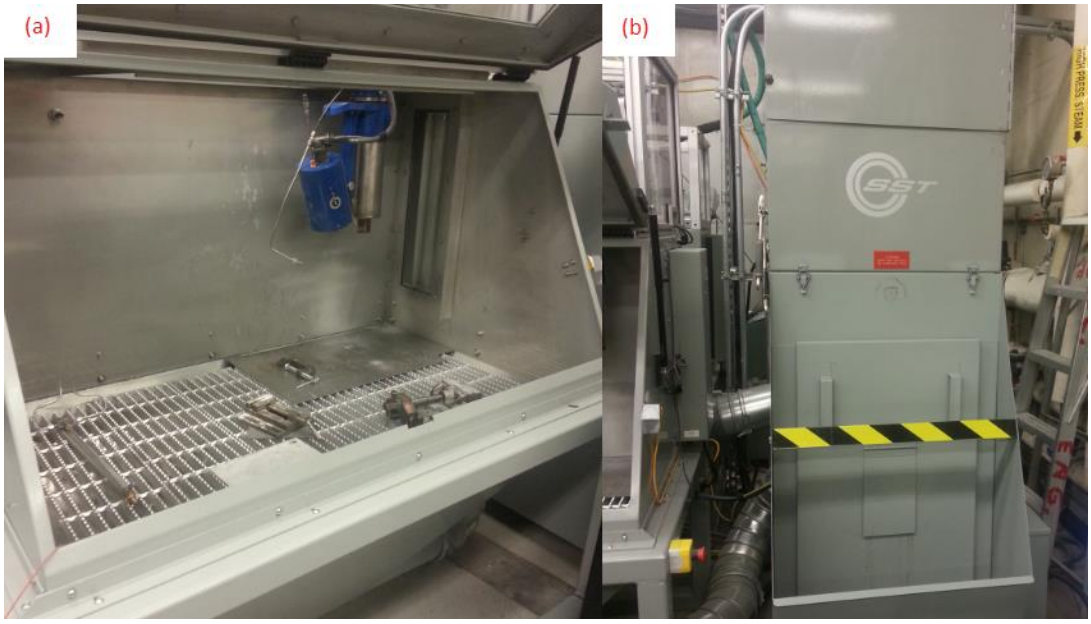

Figure 4.1: Spray chamber of the SST-EP system, a) system spray cabinet, b) powder filter

4.2.2. Spray Gun

The spray gun is shown in figure Figure 4.2. The assembly consists of a 10 kW gas heater (figure Figure 4.2a) that can heat the gas up to a temperature of 500^{o}C at maximum gas pressure of 3.45 MPa (500 psi). The SST-EP system is also equipped with a powder pre-heater (figure Figure 4.2b) that warms the powder up to 500 ^{o}C prior to it being injected in the spray nozzle. Figure 4.2c presents the powder injection line that is disconnected from the nozzle assembly. Figure Figure 4.2d shows the driving gas flow meter used to regulate the amount of gas injected in the process. Temperature of both devices are controlled digitally with a custom interface as shown on figure Figure 4.2e. Stagnation pressure of the system is controlled by a valve located on the right side of the cabinet.

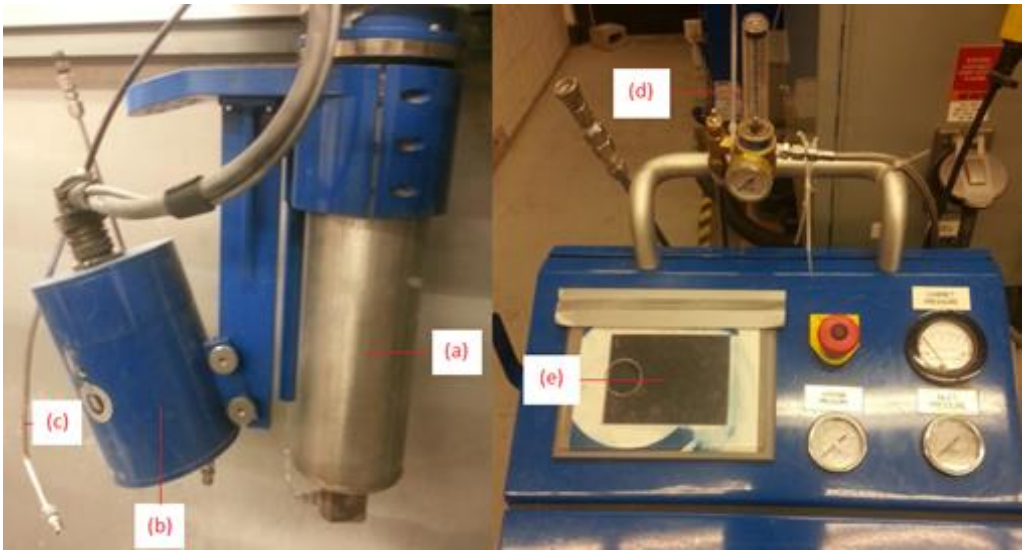

Figure 4.2: Spraying gun system, a) powder injection line, b) powder heater, c) gas heater, d) driving gas flow meter, e) system parameters input

The spray gun (Figure 4.3a) is controlled with an X-Y robot from IAI America Inc (Figure 4.3b). This robot is using stepper motors capable of reaching velocities between 1 mm/s and 500 mm/s. Robot's parameters are changed with the interface provided by IAI (Figure 4.3c).

Figure 4.3: a) X-Y robot, b) spray gun c) X-Y robot interface

4.2.3. Spray Nozzle

The nozzle assembly is responsible for the acceleration of the driving gas to supersonic speed as well as injecting the powder in the stream. Figure 4.4a shows the converging section of the nozzle and the exterior threads used to connect the assembly to the gas heater. A detailed cross-section of the nozzle with all its inner dimensions is shown in chapter 7. Figure 4.4b presents the location of the 2 mm throat area. The fixture shown on Figure 4.4c connects to the powder feeder line shown in Figure 4.2b. Powder is dragged down the line by the carrier gas regulated by the gas flow meter shown in Figure 4.2d and is injected in the gas stream at 11 mm after the throat area. A diverging nozzle (shown in Figure 4.4d) is attached to the assembly. A rapid expansion occurs within the 6 first mm after the throat area. The area varies from 2 mm to 3.73 mm.. The diverging nozzle is responsible for accelerating the gas to supersonic speed. The nozzle is manufactured out of Polybenzimidazole. This high temperature resistant polymer is used for this application to reduce nozzle clogging. It was determined by the manufacturer that metallic particles did not bond to the nozzle even after hours of spraying.

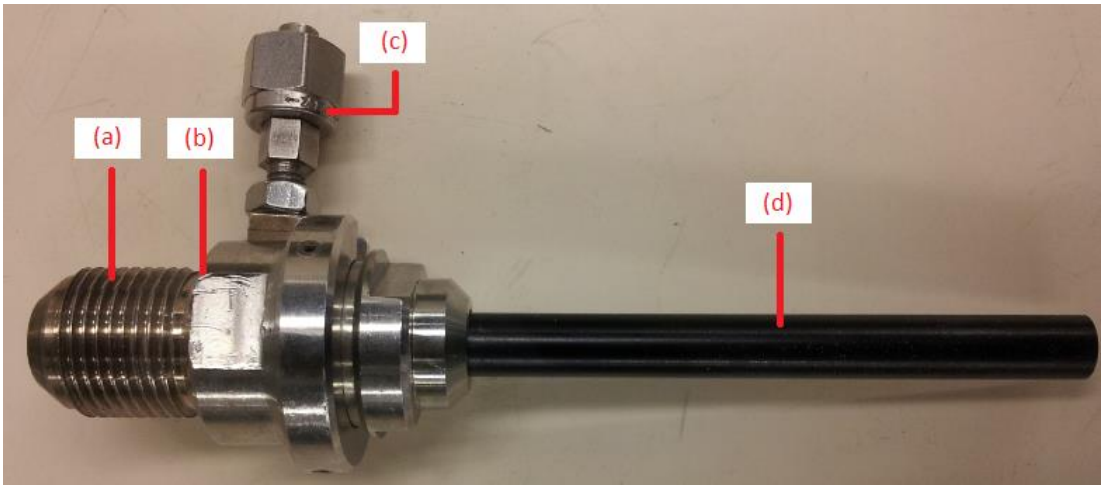

Figure 4.4: Converging-diverging nozzle of the SST-EP system a) converging section, b) the throat area, c) powder injection fitting, d) divirging section made of polymer

4.2.4. Powder Feeder

In order to inject a specific amount of powder in the gas stream, a commercial powder feeder (Thermach) (shown in Figure 4.5) was used in this study. The apparatus consists of a pressurized cylindrical canister holding the feedstock material.

Figure 4.5: Overview of the powder feeder

A control system modulates the angular velocity of a rotary wheel containing holes (Figure 4.6a) that is located at the bottom of the canister. The holes get filled with powder as the wheel turns. The powder is then pushed in an opening and is dragged towards the nozzle. A carrier gas is used to pressurize the canister and force the powder in the feeding line. The purpose of the hammer (Figure 4.6b) is to knock the wheel periodically to dislodge the powder and prevent clogging.

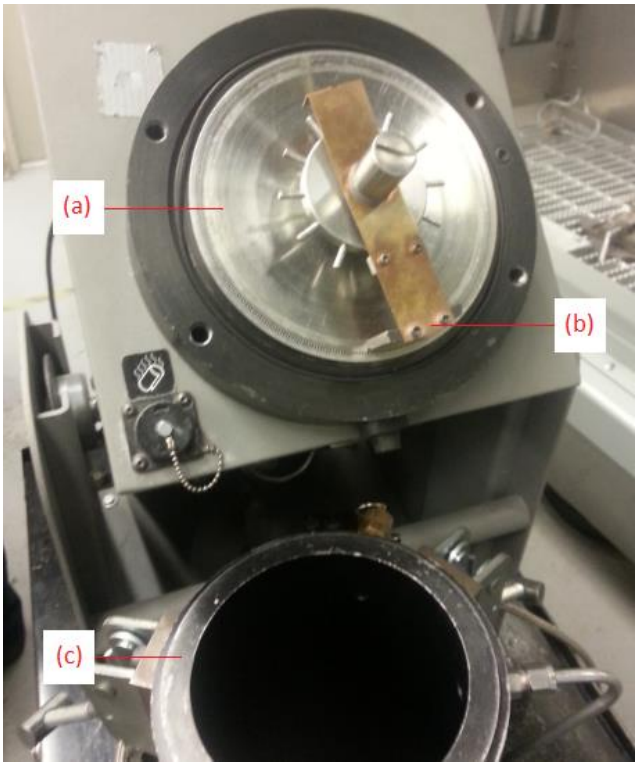

Figure 4.6: Disassembly of Thermach powder feeder, a) rotary wheel, b) powder hammer, c) powder canister

4.2.5. Driving and Carrier Gas Supply

Pressurized gas is a major element of the CGDS process. At the University of Ottawa cold spray laboratory, gas supply is maintained in a bulk pack as shown in Figure 4.7. Each pack contains 11 bottles of nitrogen or helium pressurized at up to 16 MPa. These packs are connected to the system main valve and to the powder feeder. The pressurized gas main purpose is to feed the system and produce a supersonic flow in the nozzle. Its secondary purpose is to pressurize the powder feeder and carry the feedstock material to the injection point.

Figure 4.7: Driving Gas Supply

Figure 4.8 represents the primary pressure regulator. This device is used to reduce the system inlet pressure to 650 psi. A flow meter is also used to modulate the carrier gas flow rate before entering the powder feeder canister.

Figure 4.8: Primary pressure regulator

4.3. Powder and Coating Analysis Equipment

4.3.1. Microscopic Observation

Prior to analysing coatings and powder microstructure, samples are prepared with the equipment shown in Figure 4.9. The saw shown on Figure 4.9a (Secotom-10, Struers) is used to cut the cross-section of the samples to be analyzed. Samples are then mounted in an epoxy resin cylinder to facilitate the polishing process. This instrument is the LaboPress-3 (Struers) and is shown on Figure 4.9b. Once the samples are mounted in epoxy resin, the apparatus shown on Figure 4.9c (Struers Tegrapol, TegraForce-5 and TegraDoser-5) is used to polish the cross-section of the coatings.

Figure 4.9: Equipment used to prepare samples prior to analysis, a) Cut-off saw (Struers Secotom-10), b) Epoxy resin mounting equipment (Struers LaboPress-3), c) Polishing apparatus (Struers Tegrapol, TegraForce-5 and TegraDoser-5)

Coatings and substrates microstructures are then analysed with the two different optic microscopes available at the University of Ottawa Cold Spray Laboratory. The first one is a 2D optical microscope equipped with a digital camera and connected to a computer to display the image (Figure 4.10a). Clemex Vision Lite image analysis software is used to determine the coating porosity level, coating thickness and particle deformation.

Figure 4.10b shows the 3D digital microscope (Keyence VHX-2000 series) used to accomplish similar tasks as the 2D microscope, however the camera can move in the vertical axis to produce 3D images. These images can be used to determine the surface roughness of a substrate for example.

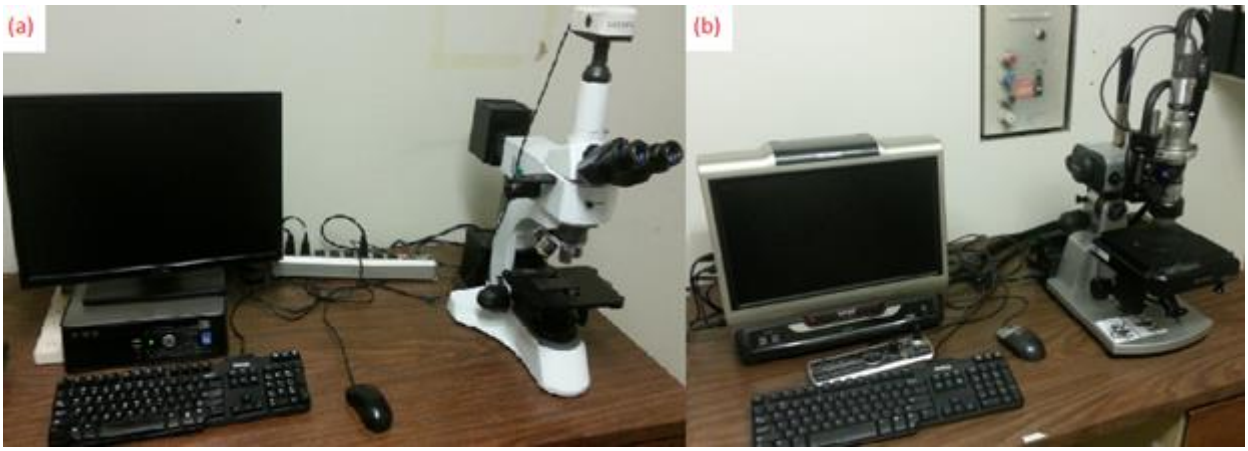

Figure 4.10: Optical microscopes, a) 2D optical microscope equipped with a digital camera (Kingdak NMM-800TRF and Clemex Vision Lite Software), b) 3D optical microscope (Keyence VHX-2000 series)

Optical microscopes are limited to a focus of 1000X. A scanning electron microscope (SEM) can be used for larger magnification. SEM images can only be produced on conductive samples. A sputterer (shown on Figure 4.11) from Denton Vaccum is used to create a thin conduction layer of gold over the sample and the epoxy resin to allow the electrons to flow across the surface.

Figure 4.11: Cold plasma gold sputtering apparatus

The scanning electron microscope used in this study (EVO-MA10, Zeiss, UK) is shown on Figure 4.12. The SEM is equipped with energy dispersive spectroscopy (EDS), electron backscatter diffraction (EBSD), secondary electron (SE) and X-ray computed tomography (CT) detectors.

The secondary electron device was used to take highly defined images of coatings cross-sections, powders and single particle bonded on a substrate. SE was used to identify the oxide layer on anodized aluminum coatings.

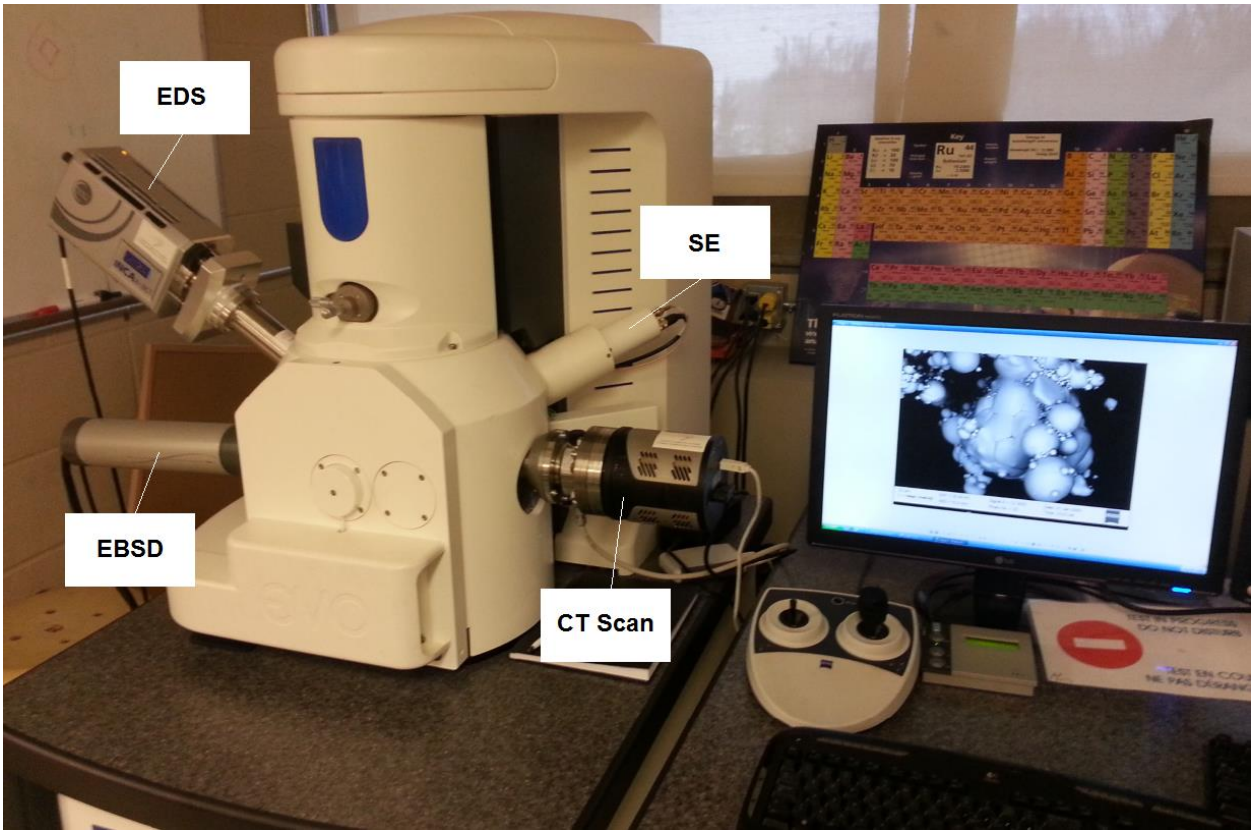

Figure 4.12: Scanning electron microscope (Zeiss Evo10)

4.3.2. Hardness Test

Microhardness measurements were obtained by the instrument shown in Figure 4.13 (Struers Duramin-1). The analysis consists of a diamond indenter that penetrates a polished substrate for 10 seconds. The width and the height of the diamond indentation are measured. The two values are put in a formula established by the manufacturer to obtain the hardness value of the studied material.

Figure 4.13: Struers Duramin-1 hardness apparatus

4.4. Coating Characterization Equipment and Method

4.4.1. Adhesion Strength

Adhesion strength of coatings were evaluated according to ASTM Standard C-633: Standard Test Method for Adhesion of Cohesion Strength of Thermal Spray Coatings [46]. This test consists of producing a coating on a one inch diameter rod. The coating is then milled down to 400 μm and glued (using FM-1000 Elastomeric Adhesive, Cytec Engineering Materials) with another rod facing down. Figure 4.14 shows the assembly before and after the test.

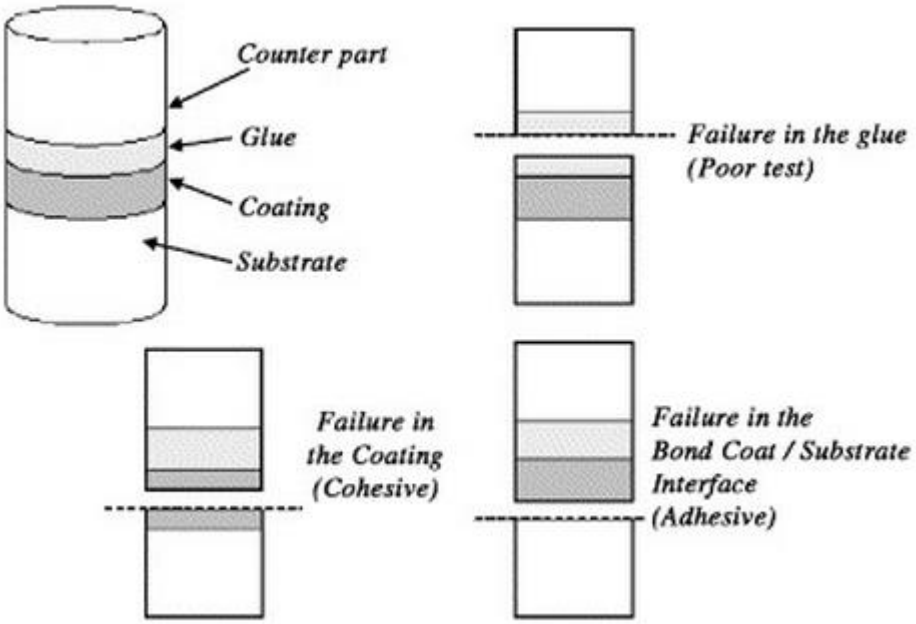

Figure 4.14: Bond plugs prior and after the adhesion test [47]

It is observed that there are three different modes of failure: failure of the glue, failure of the coating (cohesive failure) and failure of the coating/substrate interface (adhesive). Figure 4.15 shows the dimensions of the substrates used in this experiment.

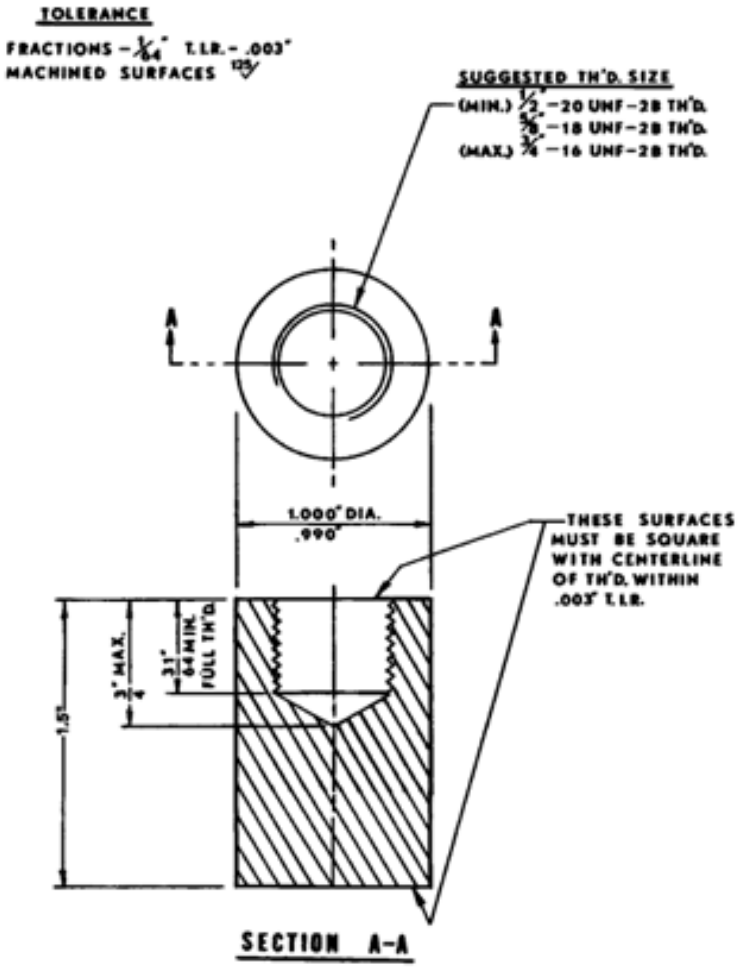

Figure 4.15:Dimensions of a substrate (bond plug) [46]

Bond plugs are pulled using the Instron machine shown in Figure 4.16. This device exerts a tensile load at a constant rate of cross-head travel of 0.02 mm/s until failure. The ultimate tensile load is given by the Instron's interface. The adhesion strength of the coatings is measured by dividing the load over the coating area.

Figure 4.16: Instron apparatus

4.4.2. Taber Abrasion Test

The repaired components are subjected to a wear test in order to evaluate the quality of the oxide film built on the coatings. This testing follows the ASTM D4060: Standard Test Method for Abrasion Resistance of Organic Coatings by the Taber Abraser [48]. The Taber Abrasion test set-up is shown in Figure 4.17.

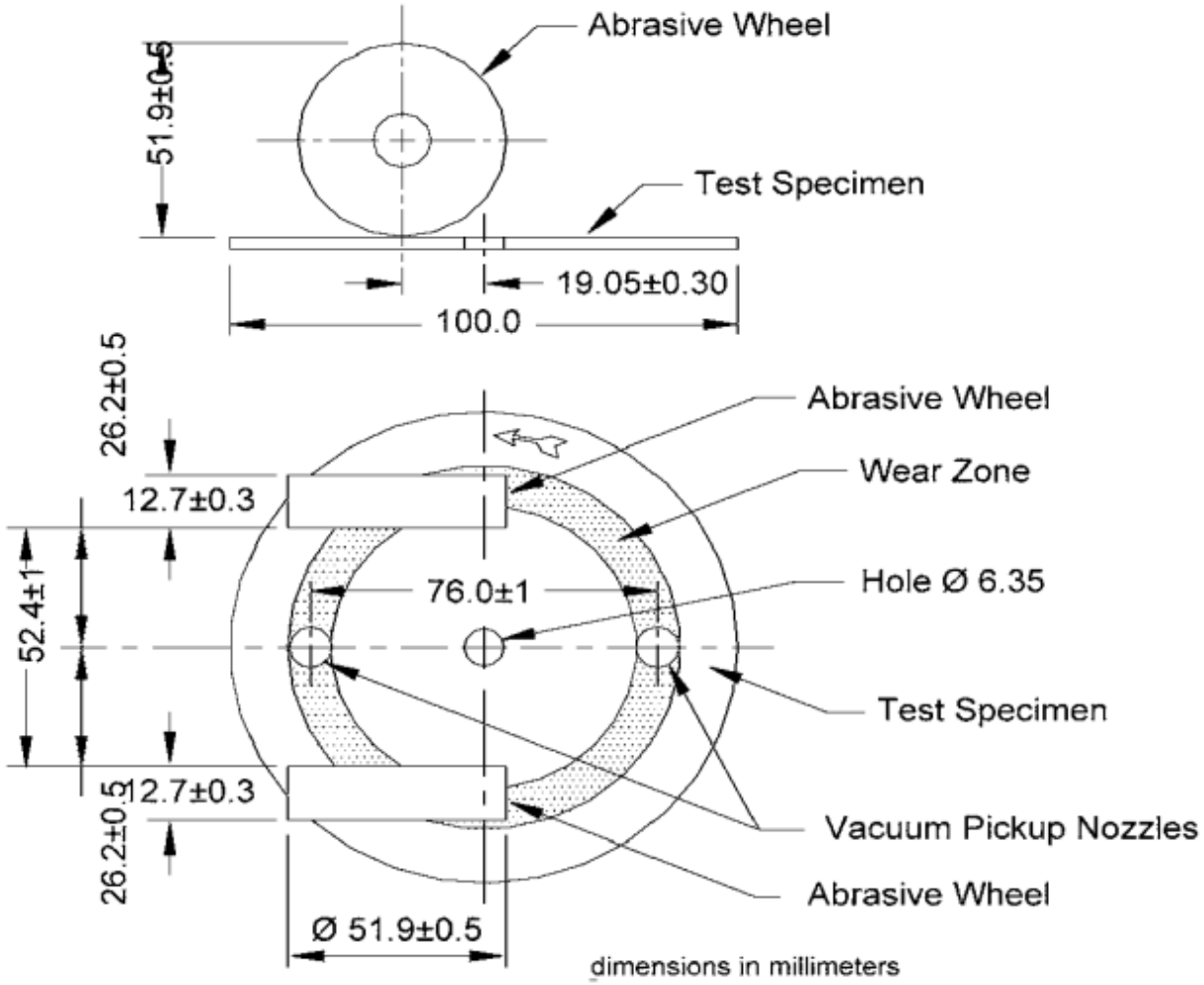

Figure 4.17: Diagrammatic arrangement of the Taber Abraser test set-up [48]

The aluminum coatings on aluminum 7075-T6 substrate (6.35 mm thick) are subjected to the anodizing process prior to be tested for 10,000 cycles on the Taber Abraser Model 140 CS with a wheel rotating at 70 rpm. The samples are weighted before and after the test to measure the amount of material loss. A maximum weight loss of 20 milligrams per sample is set by the industry.

5. Feasibility Study, Spray Parameters Optimization and Coating Properties

5.1. Introduction

This chapter will describe the feasibility study of producing aluminum 7075 and pure aluminum coatings on aluminum 7075-T6 substrates using the SST-EP system. Once this is demonstrated, spray parameters will be optimized in order to obtain the best coating quality. These coatings will then go through series of test in order to meet industry standards as well as specific ASTM standards.

5.2. Aluminum 7075

5.2.1. Powder Characterization

Aluminum 7075 powder was used in this study to repair non-structural aluminum 7075-T6 aircraft parts. The powder for this project is AA7075-200 mesh bought from Valimet (Stockton, CA, USA). The particles are gas atomized and spherical and can be observed in Figure 5.1. Laser diffraction analysis (Microtac S3500, Nikkiso, Japan) was used to determine the particle size. The results showed a mean particle size based on volume (MV) of 42.12 µm, number of particles (MN) of 13.46 µm and area (MA) of 29.62 µm. It is to be noted that these are mainly used as input parameters when using the cold spray meter.

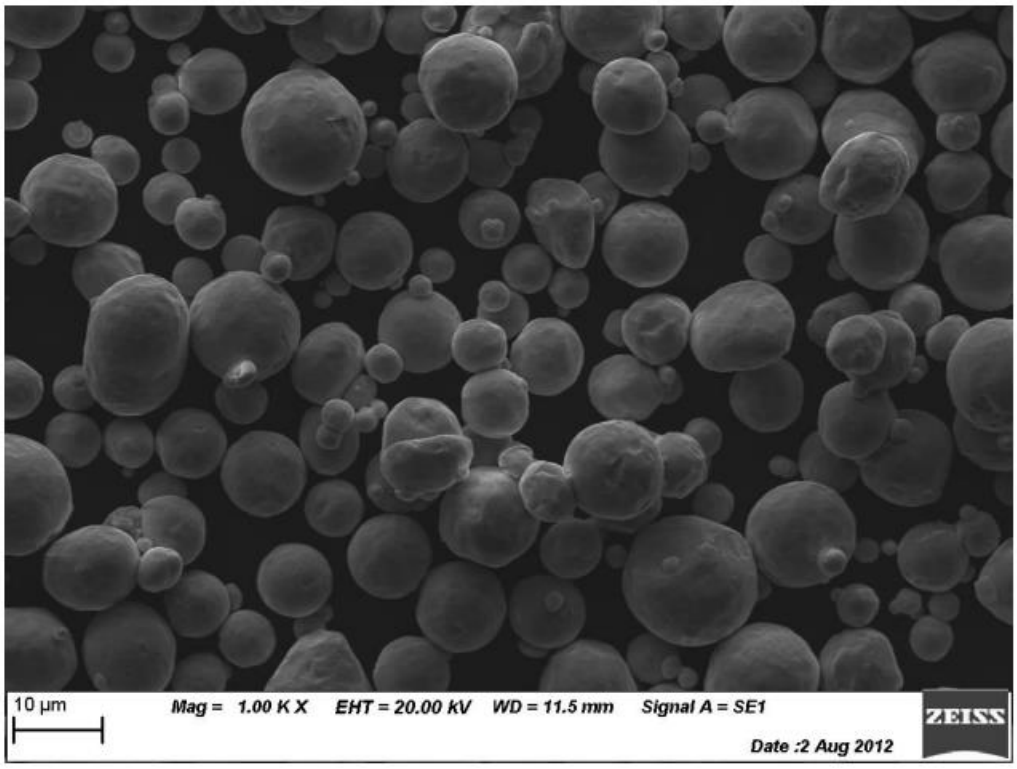

Figure 5.1: SEM image of aluminum 7075 powder (AA7075-200 mesh (Valimet) [45]

5.2.2. Substrate Characterization

6.35 mm aluminum 7075-T6 plates were used as substrates in this study. All substrate surfaces were subjected to a grit blasting procedure prior to be sprayed and the parameters are found in Table 5.1. The grit blasting unit uses air as the process gas and a hand held gun with a 5.2 mm steel nozzle area kept at approximately 50 mm from the substrate at a 45 degree angle. A fine abrasive was used to prepare the aluminum 7075-T6 substrates in order to pursue the procedures established by McDonald [45] . The abrasive is a fine grit (80 mesh) aluminum oxide (Opta Minerals Inc.). After grit blasting, all substrates were cleaned with acetone and dried with compressed air.

Table 5.1: Surface preparation procedure for aluminum 7075 on aluminum 7075-T6 substrates

Parameters	
Gas Pressure	413 kPa (60 psi)
Gas Nature	Compressed Air
Grit Nature	Aluminum Oxide
Grit Size	80 mesh
Spray Angle	45°
Standoff Distance	2 inch

Figure 5.2 shows a 3D image of the aluminum 7075-T6 substrate surface after being prepared using the procedure of Table 5.1. This surface preparation procedure resulted in surface roughnesses of 1.52 µm (Ra) and 16.73 µm (Rt). It is to be noted that the roughness average (Ra) is expressed as the arithmetic average value of the departure from profile from the center line whereas Rt is simply the maximum peak to valley height.

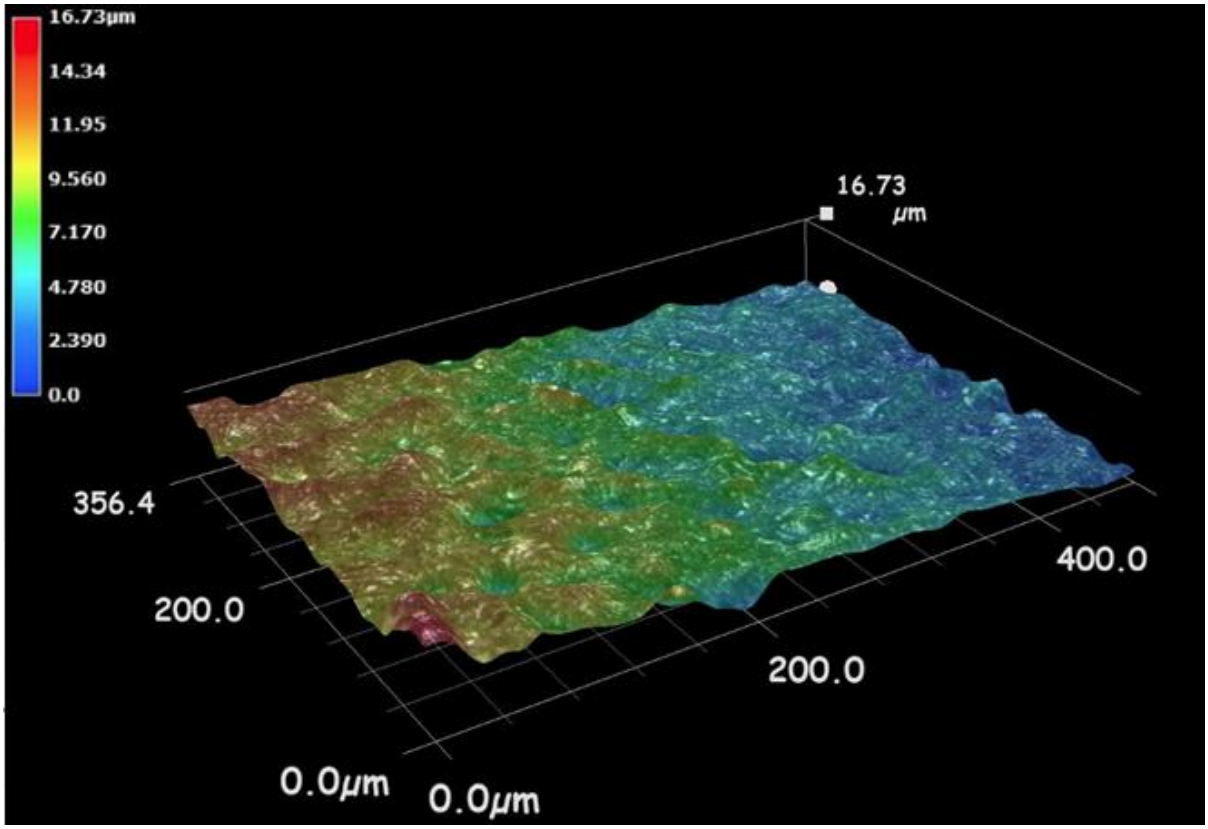

Figure 5.2: 3D image of aluminum 7075-T6 substrate after grit blasting fusing the parameters indicated in Table 5.1

5.2.3. Feasibility Study using the SST-EP System

It was previously established by McDonald [45] that helium needed to be used as the driving gas to produce aluminum 7075 coatings in order to prevent damaging the substrate heat treatment. The deposition efficiency was very low when using nitrogen even when high driving gas temperature was used. A low deposition efficiency (thus long spraying time) combined with high driving gas temperature resulted in change of substrate microstructure. As mentioned in Chapter 3, the heat treatment of the substrate needs to be maintained in order to meet industry requirement. However, the aerospace industry wants to avoid helium due to its high cost and rarity. The new SST-EP system

can operate with a higher stagnation pressure that should result into higher deposition efficiency and a decreased spraying time and allow using nitrogen as the driving gas.

The first step was to investigate the feasibility of producing aluminum 7075 coatings sprayed with the new SST-EP system and nitrogen as the driving gas. Coatings were produced using the optimized spray parameters established by Trahan [49], shown in Table 5.2. It is noted that these parameters were used to produce aluminum 7075 coatings with the SST-P system and a hydro formed stainless steel nozzle (HFSS) (its inner geometry is presented in chapter 6).

Table 5.2: Optimized parameters for aluminum 7075 on aluminum 7075-T6 using the SST-P system

Parameter Selection	*Optimized Value*
Gas Pressure	1.72 MPa (250 psi)
Gas Nature	Nitrogen
Gas Temperature	500°C (932°F)
Standoff Distance	15 mm (590 thou)
Nozzle Type	120 mm SS Nozzle (4.7 in)
Orifice Diameter	2 mm (78.7 thou)
Powder Feeder Wheel Type	120 Hole
Powder Feeder Rate	3 RPM
Powder Feeder Gas Flow Rate	15 SCFM
Powder Feeder Gas Nature	Nitrogen
Traverse Velocity	15 mm/s (590 thou/s)
Step Size	1 mm

The experiment was completed using the SST-EP polymer nozzle and the HFSS nozzle. Aluminum 7075 coating on aluminum 7075-T6 substrate using the SST-EP system and the SST-EP polymer nozzle is shown in Figure 5.3 left. Figure 5.3 right shows the coating produced with the HFSS nozzle.

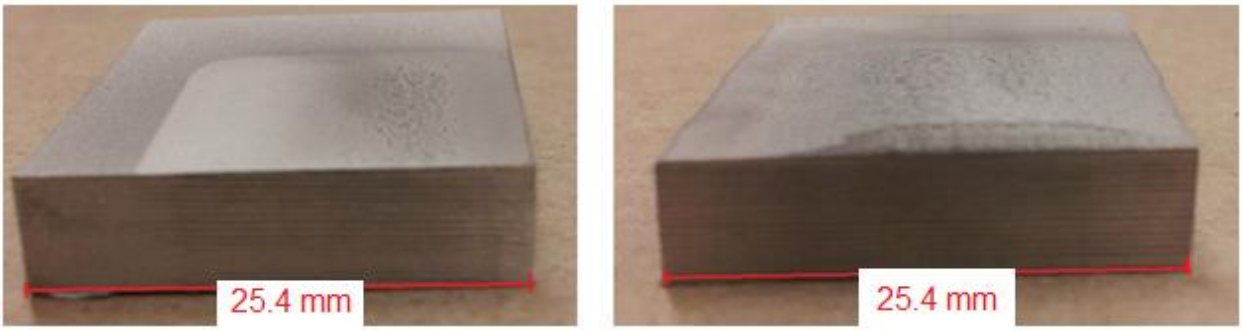

Figure 5.3: Aluminum 7075 coatings produced with the SST-EP system and the SST-EP polymer nozzle (left), HFSS nozzle (right)

The cross-sections of the coatings are respectively shown in Figure 5.4.

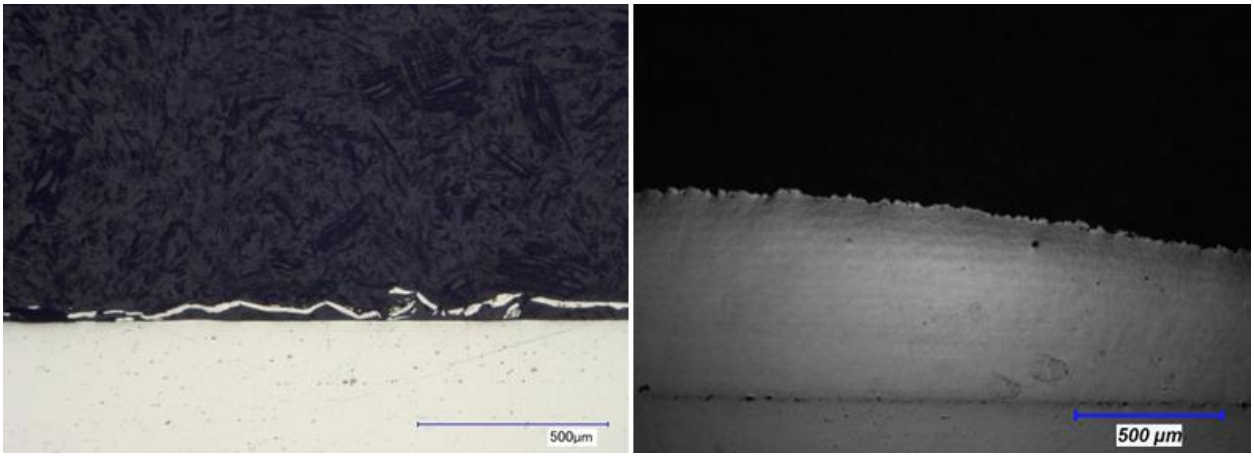

Figure 5.4: Cross-section of aluminum 7075 coatings produced with the new SST-EP system and the SST-EP polymer nozzle (left), HFSS nozzle (right)

Very low deposition of aluminum 7075 is found on the substrate when using the SST-EP polymer nozzle despite the fact that a 200 µm thick coating is obtained when using the HFSS nozzle.

It is to be noted that the geometry of the SST-EP polymer nozzle is different than the geometry of the HFSS nozzle. The SST-EP polymer nozzle is manufactured with steps while the HFSS nozzle has a smooth inner surface (their inner dimensions are presented in Chapter 6). The powder injection also occurs downstream in the SST-EP polymer nozzle. The HFSS nozzle is outperforming the SST-EP polymer nozzle but was discarded for this study due to clogging. After only few minutes of spraying time, aluminum 7075 particles would stick to the nozzle's inner wall and accumulate. This phenomenon is well known in cold spray and makes certain materials (usually soft metals) difficult to spray with metallic nozzles. Nozzle clogging prevented the HFSS nozzle to be used industrially.

Many spray trials have been performed with the SST-EP polymer nozzle using a wide range of spray parameters. The objective was to get any kind of coatings on the substrates. However, there was still very low deposition on the substrate when using the maximum pressure and temperature of the spray system. The results of these trials indicate that both nozzles are performing poorly.

5.2.4. Conclusion

The SST-EP system did not successfully produce an aluminum 7075 coatings on aluminum 7075-T6 substrate when using the SST-EP polymer nozzle and nitrogen as the driving gas. Table 5.3 presents coatings' thickness produced with the HF SS nozzle and the SST-EP polymer nozzle when using different stagnation pressures and temperatures. It is to be noted that all other parameters were held constant and coatings were produced using 4 passes. The HFSS nozzle would clog after few passes. Powder preheating was not tested with the HFSS nozzle due to intense clogging.

Table 5.3: Coatings produced with two different nozzles at different spray parameters

Powder Preheating (400 °C)	*Gas Pressure (MPa)*	*Gas Temperature (°C)*	*Coating Thickness (µm) when using the SST-EP Polymer Nozzle*	*Coating Thickness (µm) when using the Hydro Formed SS Nozzle*
No	1.72	500	No coating	1000
No	3.45	500	No coating	2200
Yes	1.72	500	No coating	Not attempted
Yes	3.45	500	No coating	Not attempted

These results show that the SST-EP polymer nozzle cannot produce aluminum 7075 coating even when using system's maximum parameters. Research on aluminum 7075 was discarded by the industry because no commercially available CGDS system (from Centerline due a partnership) can produce aluminum 7075 coatings without clogging.

Chapter 6 will present the investigation completed on the different nozzles' in order to evaluate the reason both nozzles are performing differently and establish an alternative to successfully produce aluminum 7075 coatings.

5.3. Pure Aluminum

5.3.1. Powder Characterization

Pure aluminum powder was chosen in this study to repair non load-bearing aluminum 7075-T6 parts on aircrafts. The SST-A5001 pure aluminum powder is bought from

Centerline (Windsor) Ltd. The powder is irregularly shaped which usually indicates that the powder is water atomized (see Figure 5.5). However, the supplier specifies that the powder is gas atomized.

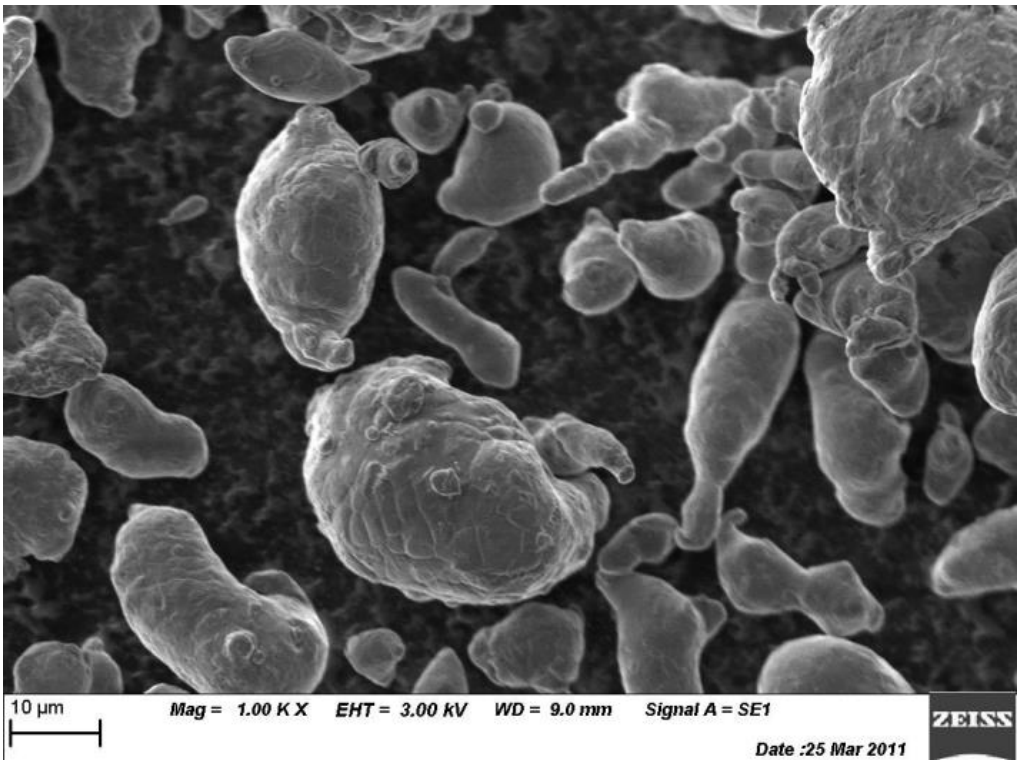

Figure 5.5: SEM image of pure aluminum powder (SST A5001)

5.3.2. Substrate Characterization

6.35 mm thick aluminum 7075-T6 substrates were initially prepared the same way as the substrates used to spray aluminum 7075 coatings. All the surface preparation parameters can be found in chapter 5.2.2.

5.3.3. Feasibility Study using the SST-EP System

Pure aluminum was sprayed using the SST-EP system. The first objective was to duplicate coatings sprayed previously with the SST-P system using the optimized spray

parameters previously established by MacDonald [45] (see Table 5.4). This experiment was conducted to verify if both systems behaved similarly.

Table 5.4: Optimized Parameters for Pure Aluminum using the SST-P Cold Spray System

Parameter Selection	***Optimized Value***
Gas Temperature	350°C (662°F)
Gas Pressure	1.72 MPa (250 psi)
Gas Nature	Nitrogen
Standoff Distance	15 mm (590 thou)
Feed Rate	14 rpm
Feed Wheel Type	320 small hole
Powder Feeder Gas Flow Rate	25 SCFM
Powder Feeder Gas Nature	Nitrogen
Nozzle Type	120 mm Ultiflow Nozzle (4.7 in)
Orifice Diameter	2 mm (78.7 thou)
Traverse Velocity	10 mm/s (400 thou/s)
Step Size	1 mm

Figure 5.6 (left) shows the 1 mm thick pure aluminum coating on aluminum 7075-T6 substrate produced with the SST-EP system. Figure 5.6 (right) shows the cross-section of the coating.

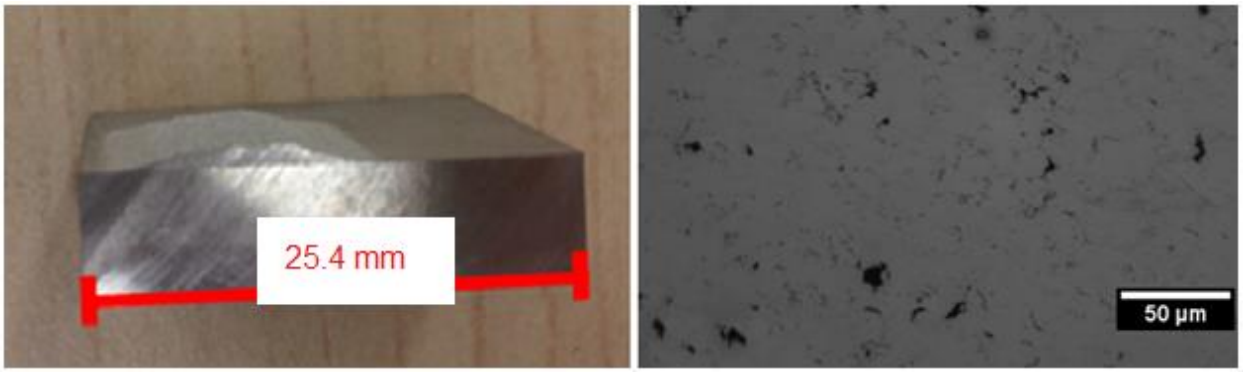

Figure 5.6: Pure aluminum coating produced with the SST-EP system (left), its cross-section (right)

It was determined that the pure aluminum coatings obtained with the SST-EP system are comparable to the ones obtained previously with the SST-P system. The pure aluminum coatings produced with the SST-P system can be seen in MacDonald's thesis [45].

5.3.4. Influence of Stagnation Temperature and Pressure on Pure Aluminum Coatings and Aluminum 7075-T6 Substrates

In order to find optimized spray parameters for pure aluminum on aluminum 7075-T6, 25 samples have been produced using different gas stagnation pressures and temperatures (see Table 5.5). With these tests optimal gas pressure and temperature can be determined in order to obtain the lowest porosity level in the coating while conserving the heat treatment of the substrate.

Table 5.5: Gas pressure and temperature used to optimized the quality of the pure aluminum coatings

Gas Pressure	***Gas Temperature (°C)***				
(MPa)	**300**	**350**	**400**	**450**	**500**
2.07 (300 psi)	Sample 1	Sample 6	Sample 11	Sample 16	Sample 21
3.41 (350 psi)	Sample 2	Sample 7	Sample 12	Sample 17	Sample 22
2.76 (400 psi)	Sample 3	Sample 8	Sample 13	Sample 18	Sample 23
3.10 (450 psi)	Sample 4	Sample 9	Sample 14	Sample 19	Sample 24
3.45 (500 psi)	Sample 5	Sample 10	Sample 15	Sample 20	Sample 25

Other spray parameters were maintained constant and were established by MacDonald and the cold spray industry's recommendation (see Table 5.6). It is to be noted that the powder mass flow rate was set to be relatively low (7 grams/minute). Prior experiments showed that a high powder mass flow rate increased coating thickness while decreasing its density. This phenomenon occurs because the pure aluminum powder tends to adhere easily. Large pure aluminum particles do not always have enough energy to fully deform but still stick to the surface. This creates porosity throughout the coating that has been shown to be detrimental to Taber abrasion test performance.

Table 5.6: Parameters held constant and used to produce pure aluminum coatings on aluminum 7075-T6 substrates.

Parameter Selection	*Optimized Value*
Gas Nature	Nitrogen
Vibrator	No
Standoff Distance	15 mm (590 thou)
Nozzle Type	120 mm SSP-EP polymer nozzle (4.7 in)
Orifice Diameter	2 mm (78.7 thou)
Powder Feeder Wheel Type	320 Holes
Powder Feeder Rate	8 RPM
Powder Feeder Gas Flow Rate	30 SCFH
Powder Feeder Gas Nature	Nitrogen
Traverse Velocity	50 mm/s (1968 thou/s)
Step Size	1 mm
Number of Cycles*	6
Number of Passes*	5
Substrate Size	¼ X 1 X 1.5 inches

*Note that the number of cycles refers to number of time the gun has to travel back and forth to cover the substrate with coating and the number of passes refers to the number of time the substrate was covered.

5.3.4.1 Effect on Coating Thickness

Figure 5.7 shows the effect of the stagnation temperature and pressure of the driving gas on the pure aluminum coating thickness.

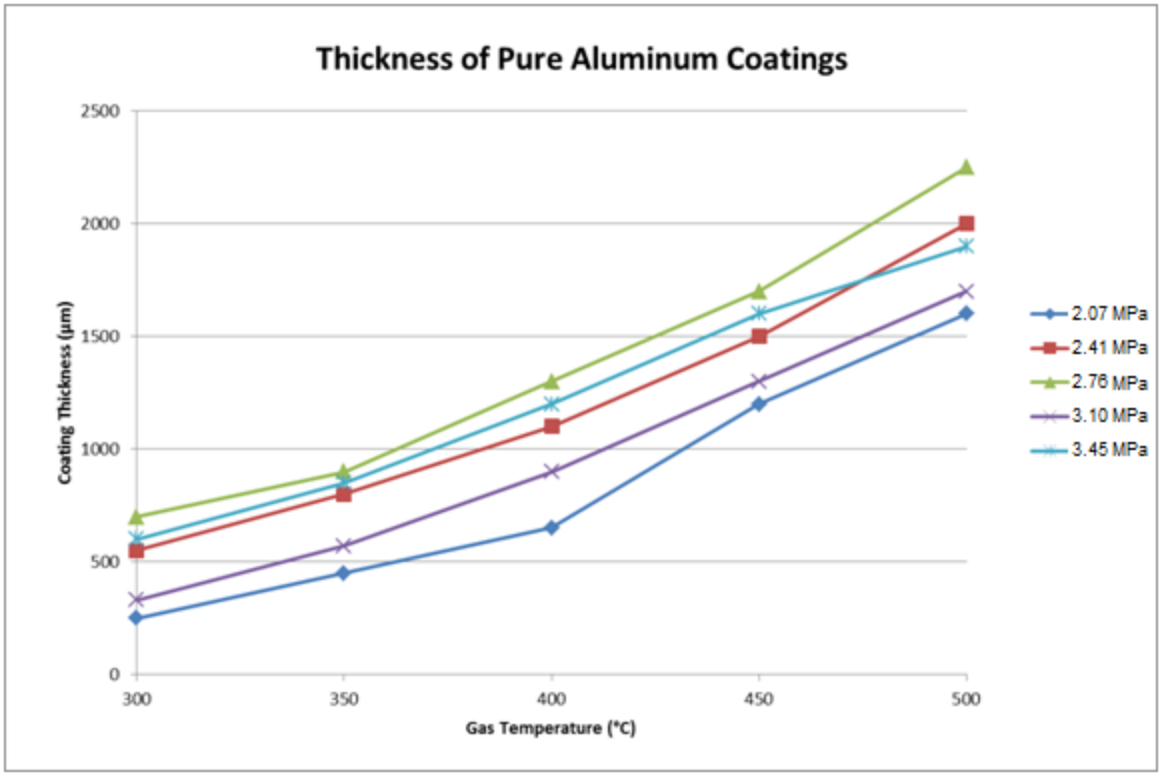

Figure 5.7: Thickness of pure aluminum coatings (lowest height throughout the cross-section) on aluminum 7075-T6 substrate

The gas pressure increases the deposition efficiency (thus coating thickness) by increasing the density of the gas. The drag force is directly proportional to the gas density. By increasing the drag force on the pure aluminum powder, more particles reach the critical velocity to adhere to the substrate. However, the 10 samples sprayed at 3.10 MPa and 3.45 MPa are thinner than the samples sprayed at 2.76 MPa. These samples were sprayed on a different day than the 2.07, 2.41 and 2.76 MPa tests which were all sprayed one after the other. It has been noticed that the substrate holder (steel) becomes hot after few sprays. Heat transfer occurs between it and the samples. A new substrate that is about to be sprayed has time to be preheated by the warm holder. The deposition efficiency increases with substrates temperature by allowing more particles to deform and adhere to the surface [50]. This is a well-known concept in CGDS. For

this reason the first few tests (before the temperature in the holder is stable) will produce thinner coatings. This could explain why the 3.10 and 3.45 MPa coatings are thinner even though higher gas pressure and temperature were used.

These results were biased due to differences in the experimental setups between the first 15 samples sprayed and the remaining 10 samples. However, the experiment showed that increasing the stagnation temperature results in higher gas velocity and particle temperature. The DE is increased when rising the gas stagnation temperature. It was observed that increasing the gas stagnation pressure influences the deposition efficiency because the gas density is higher throughout the process. By increasing the gas density, the drag force exerted on the particle is higher and greater velocities are obtained. It also demonstrated how the substrate temperature influences the deposition efficiency of pure aluminum and how critical controlling it during the experiment is.

The substrate holder has been insulated with carbon fibre plates in order to reduce the heat transfer with the substrates and get more consistent results. All future experiments have been completed with the insulated substrate holder. It is to be noted that the same 25 samples were analyzed to present the results of the following sections.

5.3.4.2 Effect on Coating Porosity Level

Figure 5.8 shows a direct relation between stagnation temperature and pressure and porosity level. Comparing Figure 5.7 and Figure 5.8, it is observed that the deposition efficiency correlates with the coating porosity level. Higher deposition efficiency

produces more porous coatings. This phenomenon occurs because larger pure aluminum particles have enough energy to adhere to the surface, but do not completely deform. This creates voids between particles and increase porosity in coatings.

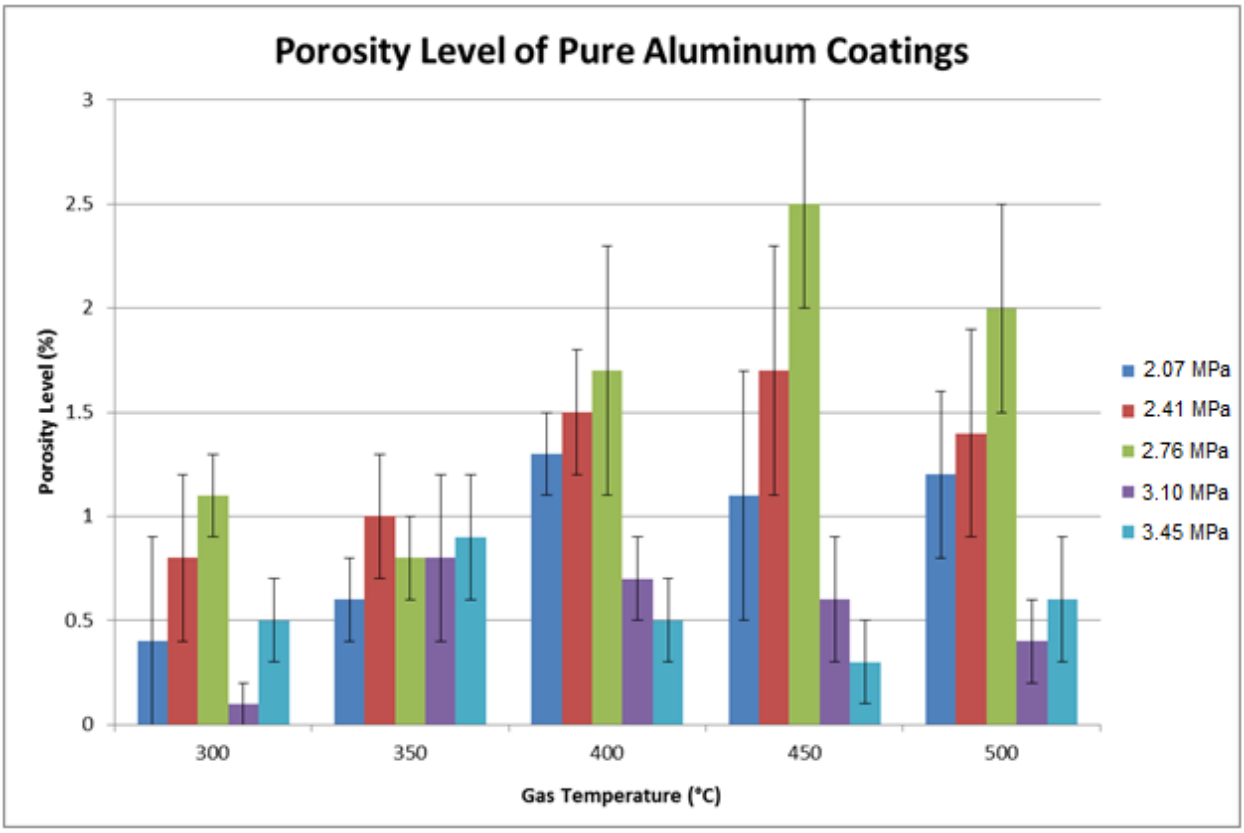

Figure 5.8: Porosity level of pure aluminum coatings on Al 7075-T6 substrate

Samples sprayed at 3.10 MPa and 3.45 MPa have drastically lower porosity levels. This is caused by the low deposition efficiency (due to reasons mentioned in section 5.3.4.1). Therefore a larger amount of big particles did not reach the critical velocity to adhere to the surface. Smaller gaps are created between the particles due to higher deformation. Consequently, the porosity level was lowered.

5.3.4.3 Effect on 7075-T6 Substrate Hardness

Figure 5.7 indicates that in order to obtain thick coatings, a high pressure and temperature should be used. However, it was determined that high spray parameters

could damage the heat treatment of the aluminum 7075-T6 substrate. Figure 5.9 shows the hardness values of the 25 7075-T6 substrates after the coating process. It is to be noted that the hardness value of the bulk aluminum 7075-T6 plates used for the experiment varied between 190 and 210 Vickers.

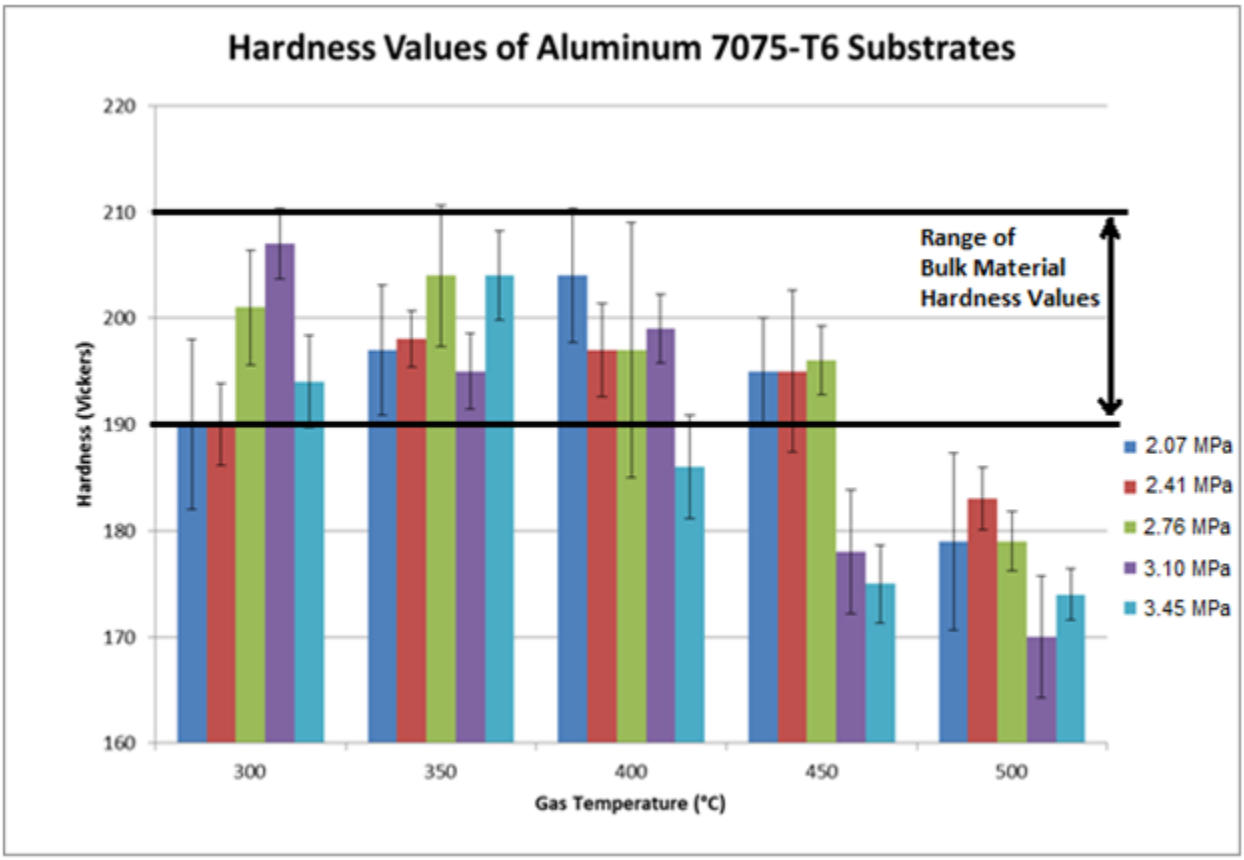

Figure 5.9: Hardness values of aluminum 7075-T6 substrates coated with pure aluminum

Figure 5.9 demonstrates that pure aluminum on aluminum 7075-T6 substrates can only be sprayed safely at 300°C or 350°C. At 400°C, 450°C and 500°C, the heat treatment of the substrates is compromised at some point. Even if the samples sprayed at; (2.07 MPa, 400°C), (2.41 MPa, 400°C), (2.76 MPa, 400°C), (3.10 MPa, 400°C), (3.45 MPa, 450°C), (2.41 MPa, 450°C) and (2.76 MPa, 450°C) do not seem to lose their heat treatment, it is assumed that spraying for a long period of time with these temperatures

would potentially damage the heat treatment even when using a low gas pressure. Furthermore it appears that the increase in pressure, but mainly temperature, allows more particles to adhere to the substrate, creating higher porosity coatings. Since this is not wanted, a maximum temperature of 350^{o}C is selected to maintain the porosity level below 1%.

5.3.4.4 Summary of the Effect of Stagnation Gas Temperature and Pressure

It was determined that using lower gas temperature and pressure reduces the deposition efficiency of pure aluminum. By reducing the deposition efficiency the porosity level in the coating is lowered. The maximum gas temperature that can be used in order to avoid damaging the heat treatment of the aluminum 7075-T6 substrate is 350°C. However, Figure 5.8 showed that when using a lower stagnation temperature and higher stagnation pressure denser pure aluminum coatings were produced (below 0.5% porosity). The most suitable gas stagnation pressure and temperature for this application are 300 °C and 3.10 MPa (450 psi).

Moreover, all future experiments will be completed using an insulated substrate holder in order to reduce the heat transfer occurring between substrate and the holder. More consistent results are to be expected.

5.3.4.5 Most Suitable Spray Parameters for the Application

Table 5.7 shows the summarized spray parameters that will be used to produce the Taber abrasion panels.

Table 5.7: Most Suitable Spray Parameters to produce Pure Aluminum coatings on Aluminum 7075-T6

Parameter Selection	*Optimized Value*
Gas Pressure	3.10 MPa (450 psi)
Gas Temperature	300 °C
Gas Nature	Nitrogen
Vibrator	No
Standoff Distance	15 mm (590 thou)
Nozzle Type	120 mm New Ultiflow Nozzle (4.7 in)
Orifice Diameter	2 mm (78.7 thou)
Powder Feeder Wheel Type	320 Holes
Powder Feeder Rate	8 RPM
Powder Feeder Gas Flow Rate	30 SCFH
Powder Feeder Gas Nature	Nitrogen
Traverse Velocity	50 mm/s (1968 thou/s)
Step Size	1 mm

Figure 5.10 shows the cross-section of the pure aluminum coating on aluminum 7075 produce using the optimized parameters found in Table 5.7. It is observed that the porosity located on the upper section of the coating can be milled off to obtain a smooth surface. A more uniform oxide layer is expected to grow when anodized. Better wear resistance results are expected when using the optimized spray parameters found Table 5.7 to produce pure aluminum coatings on aluminum 7075-T6 substrate.

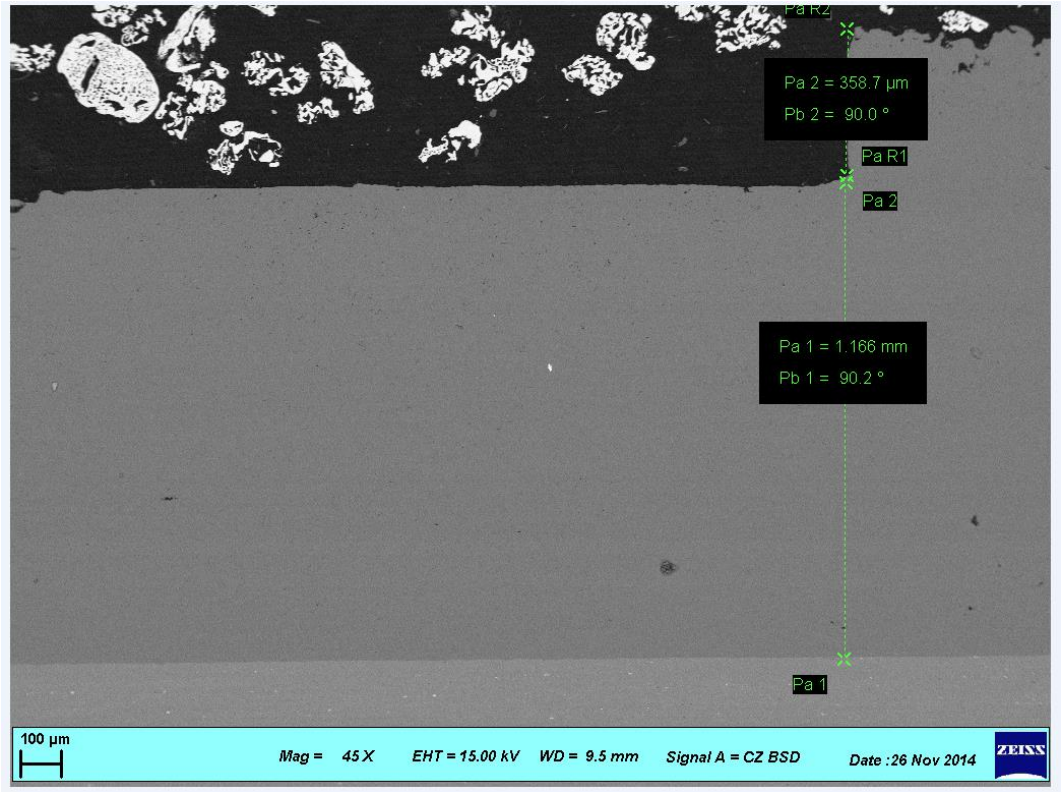

Figure 5.10: Cross-section of pure aluminum coating sprayed with a gas stagnation pressure of 3.10 MPa and temperature of 300°C

5.3.5 Adhesion Strength of Pure Aluminum on Aluminum 7075-T6 substrates

5.3.5.1 Comparison with Previous Adhesion Test Results

The spray parameters were established in the previous section to reduce porosity in coatings while maintaining the heat treatment of the substrate. The adhesion strength must be evaluated. It is to be mentioned that MacDonald's previous adhesion strength results [45] of pure aluminum on aluminum 7075-T6 showed an average of 40.5 +/- 4.4 MPa. This result exceeds the industry requirement of 13.8 MPa.

A pure aluminum coating was sprayed on five aluminum 7075-T6 bond plugs (see Figure 5.11) using the optimized spray parameters and surface preparation procedure described in sections 5.3.3 and 5.3.2. These coatings were milled down to 400 µm thick to meet ASTM-C633 adhesion test standard.

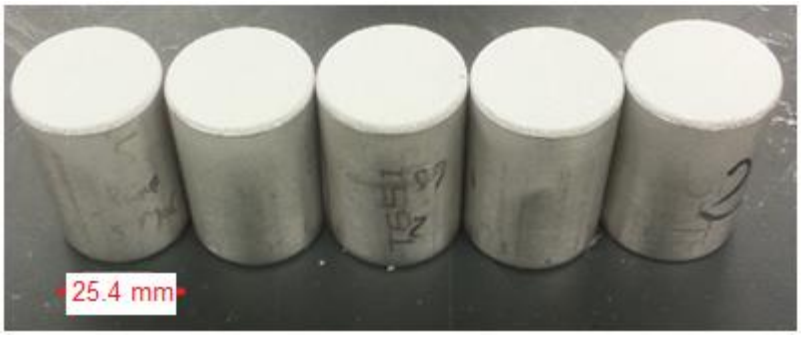

Figure 5.11: Pure aluminum coatings produced on aluminum 7075-T6 bond plugs

The average adhesion strength of the 5 pure aluminum coatings was 13.1 +/- 2.6 MPa which is lower than the industry requirement. Figure 5.12 shows a comparison of the adhesion strength of pure aluminum coatings produced with the new spray parameters and MacDonald`s spray parameters.

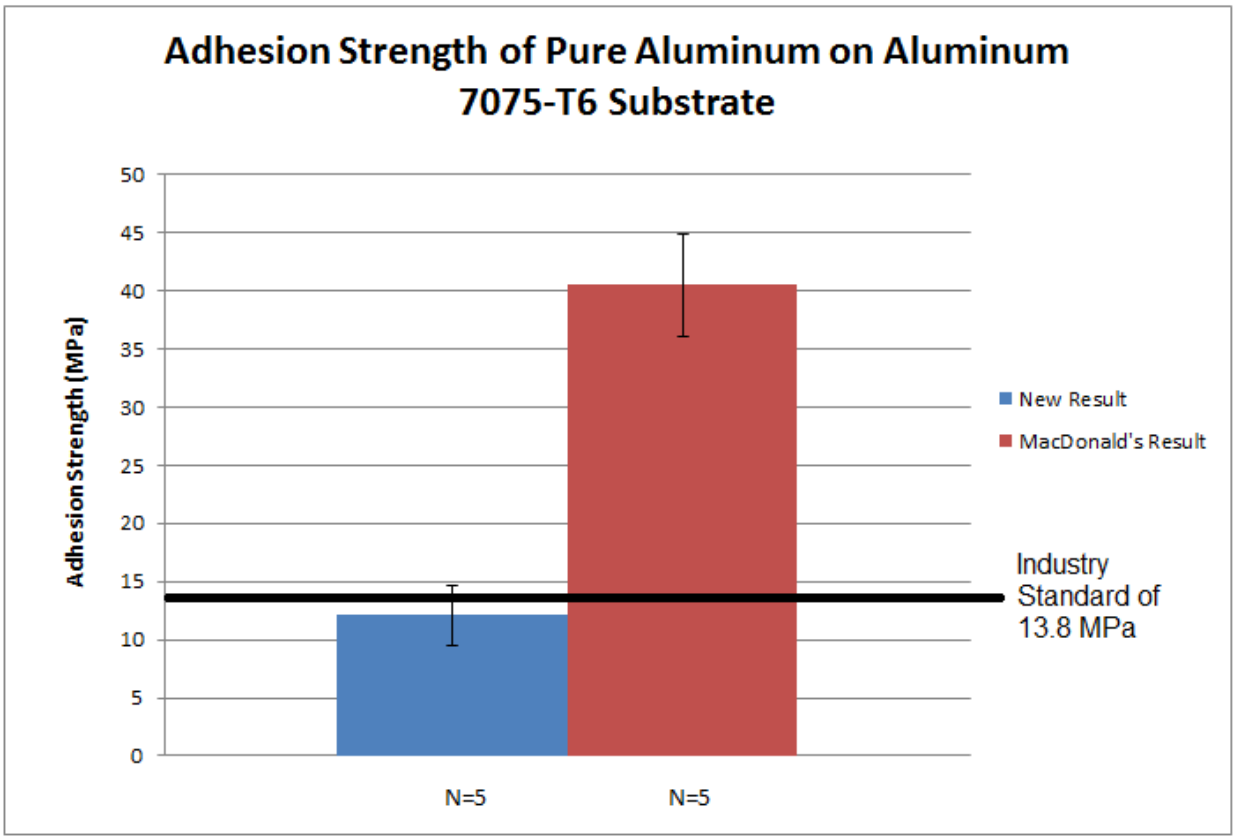

Figure 5.12: Comparison between the adhesion strength of the pure aluminum coatings produced with the new spray parameters and MacDonald`s spray parameters

The surface preparation procedure used was the same for both experiments. It is noticed that the new adhesion strength result is drastically lower than MacDonald's result. All samples failed in adhesion and Figure 5.13 shows a pure aluminum coating after failure.

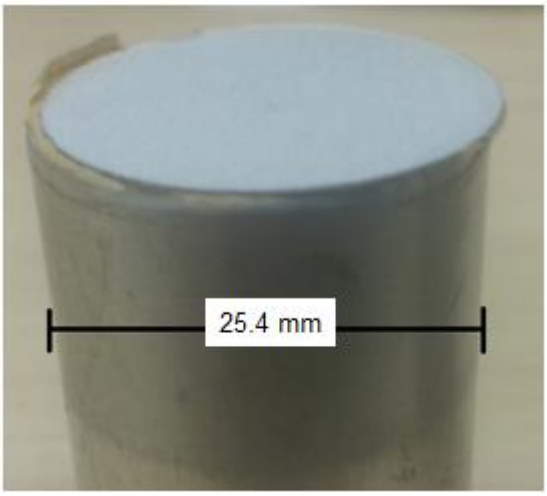

Figure 5.13: Pure aluminum coating that failed in adhesion (between the coating and the substrate)

The failure mechanism (adhesion) shows that the adhesion strength can be improved by potentially changing the surface preparation procedure and increase the contact area between the coating and the substrate.

5.3.5.2 Pure Aluminum Low Adhesion Strength Explanation

Low adhesion strength of pure aluminum on aluminum 7075-T6 found in the previous section is directly related to the fact that new spray parameters were used to produce the coatings. It is to be mentioned that MacDonald's pure aluminum coatings were produced with the previous SST-P system which uses a maximum stagnation temperature of 350°C at 1.70 MPa (250 psi). New pure aluminum coatings were evaluated to be denser when using a gas stagnation temperature of 300°C and pressure of 3.10 MPa (450 psi). The decrease in adhesion strength of the new pure aluminum coatings is potentially caused by an increase in compressive residual stress in the coatings when using higher gas stagnation pressure. It is to be mentioned that

stress relief heat treatment could not be used on the coatings in order to maintain the substrate's mechanical properties. Higher stagnation pressure results in a higher drag force and higher particle velocity. The pure aluminum powder impacts the substrate with higher kinetic energy resulting into more deformation and an increase in residual stress. Figure 5.14 shows the average particle velocity (499 m/s) when using MacDonald's spray parameters.

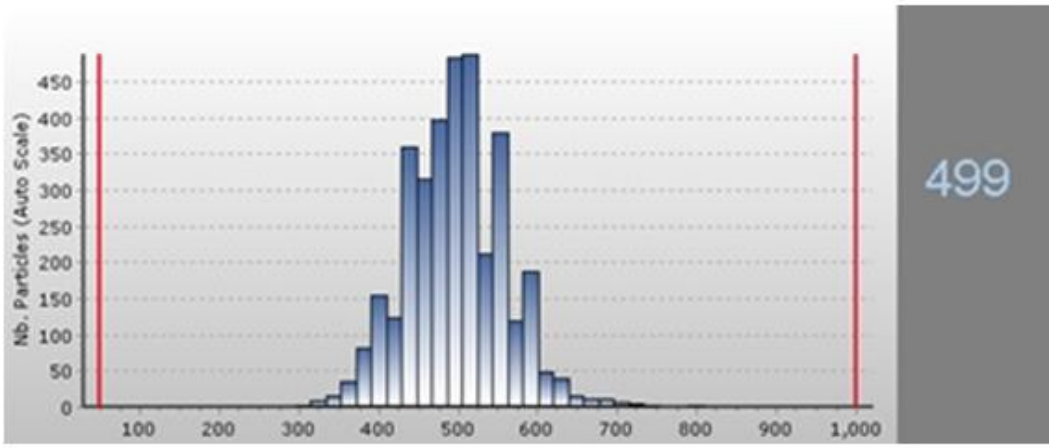

Figure 5.14: Histogram of pure aluminum particle velocity (m/s) using MacDonald's spray parameters

Figure 5.15 shows the average particle velocity (560 m/s) when using the new spray parameters to produce pure aluminum coatings on aluminum 7075-T6 substrate.

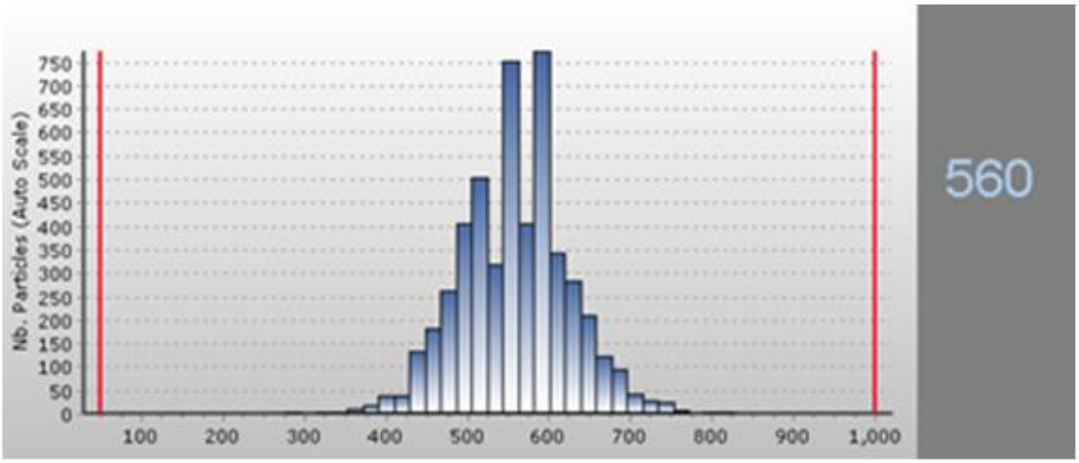

Figure 5.15: Histogram of pure aluminum particle velocity (m/s) using new optimized spray parameters

It is observed the particles are travelling at a faster velocity, prior to impacting the substrate, when using the new optimized spray parameters. The new parameters promote more hammering effect to obtain dense coatings. The lowered porosity level in new pure aluminum coatings is due to higher deformation of the particles. Higher deformation results into more compressive residual stresses in the coating. These stresses tend to lower adhesion strength in CGDS. In order to solve the low adhesion strength issue without modifying the spray parameters, new substrate preparation procedures will be used and analyzed.

5.3.5.3 Improving Adhesion Strength of Pure Aluminum Coatings

The objective of the tests completed in this section is to improve the adhesion strength of pure aluminum coatings on aluminum 7075-T6 substrates in order to meet the industry standard of 13.8 MPa (2000 psi). Table 5.8 shows the grit blasting parameters previously used to prepare the substrates.

Table 5.8: Previous Grit Blasting Parameters

Property	***Parameters***
Pressure	413 kPa (60 psi)
Gas Nature	Compressed Air
Grit Nature	Black Alumina
Size	80 Grit
Angle	45°

New surface preparation procedures were established in order to improve the adhesion strength of pure aluminum coatings on aluminum 7075-T6 substrate. It was decided to

increase the surface roughness (Ra) of the substrates prior to spraying in order to increase the contact area between the coating and the substrate. Table 5.9 shows three different grit blasting parameters used to enhance the surface roughness (Ra) of the substrate.

Table 5.9: New Grit Blasting Parameters

Grit blasting procedure #	***1***	***2***	***3***
Pressure	1.37 MPa (200 psi)	413 kPa (60 psi)	413 kPa (60 psi)
Gas Nature	Nitrogen	Compressed Air	Compressed Air
Grit Nature	Steel	Steel	Copper Slag
Size	25-40 grit	25-40 grit	20 Grit
Angle	45°	45°	45°

After the grit blasting procedure was performed, the substrate surface roughness was determined. The following 3D images represent the surface profile of aluminum 7075-T6 substrates after being grit blasted with the 3 different procedures. Figure 5.16 presents the surface profile of aluminum 7075-T6 when using the grit blasting procedure 1 (resulting in a Ra value of 5.90 µm and Rt value of 73.77 µm).

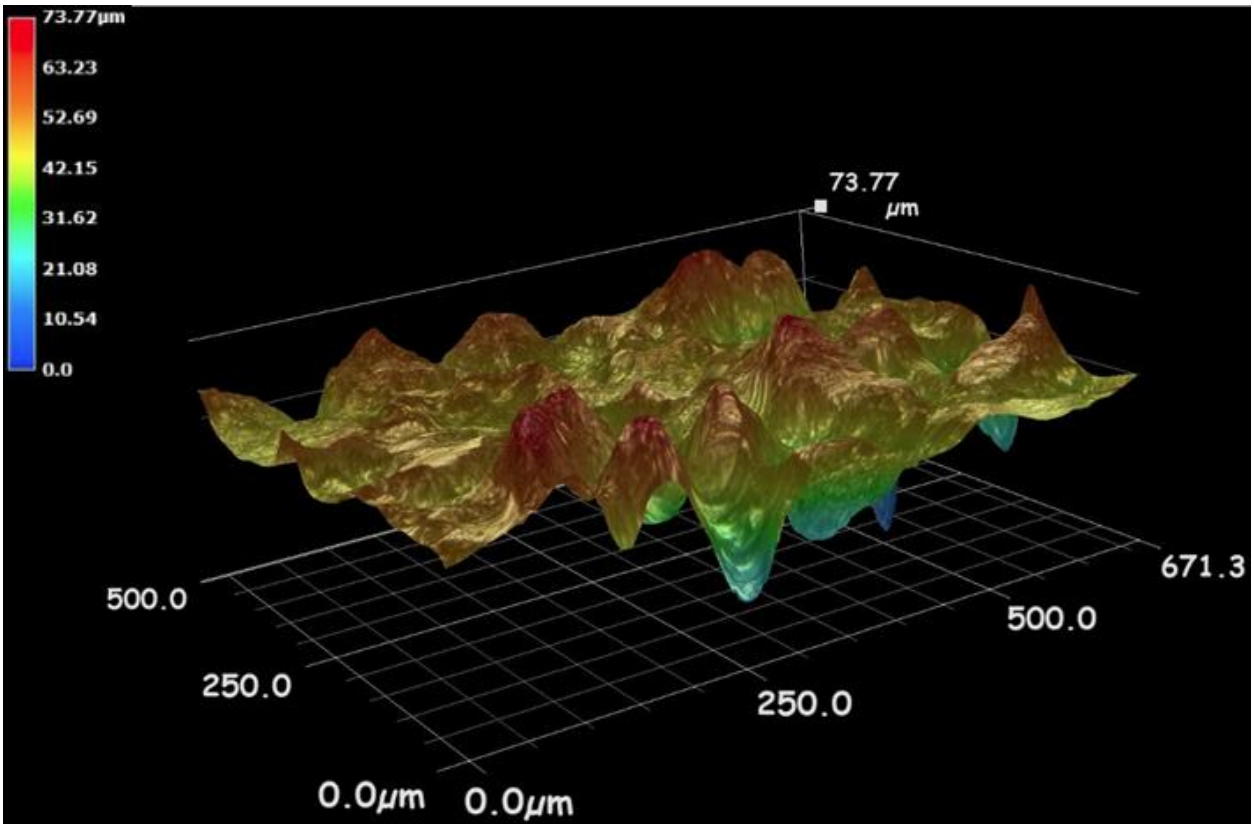

Figure 5.16: 3D image of aluminum 7075-T6 after grit blasted with steel grit at 1.37 MPa (200 psi)

Figure 5.17 represents the surface roughness of aluminum 7075-T6 when using the grit blasting procedure 2 (resulting in a Ra value of 4.19 µm and Rt value of 57.14 µm).

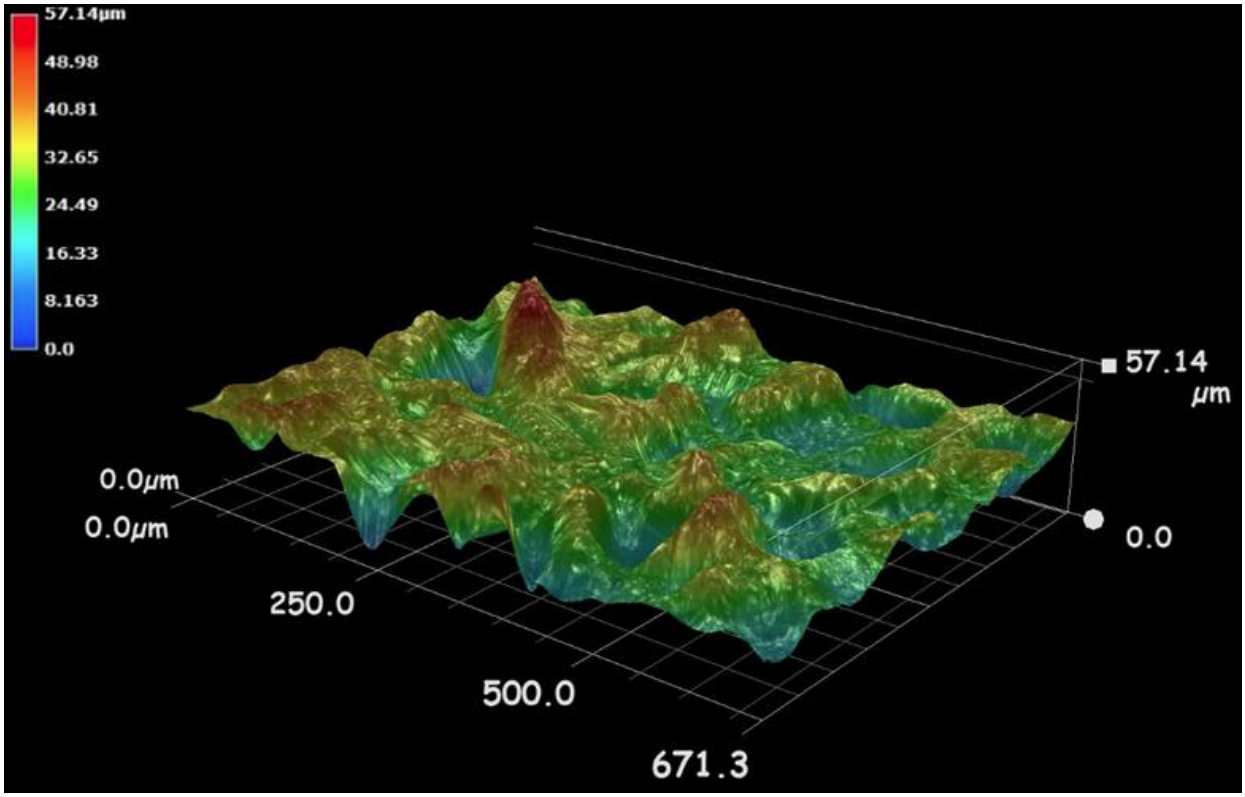

Figure 5.17: 3D image of aluminum 7075-T6 after grit blasted with steel grit at 413 kPa (60 psi)

Figure 5.18 represents the surface roughness of aluminum 7075-T6 when using the grit blasting procedure 3 (resulting in a Ra value of 3.32 µm and Rt value of 35.19 µm).

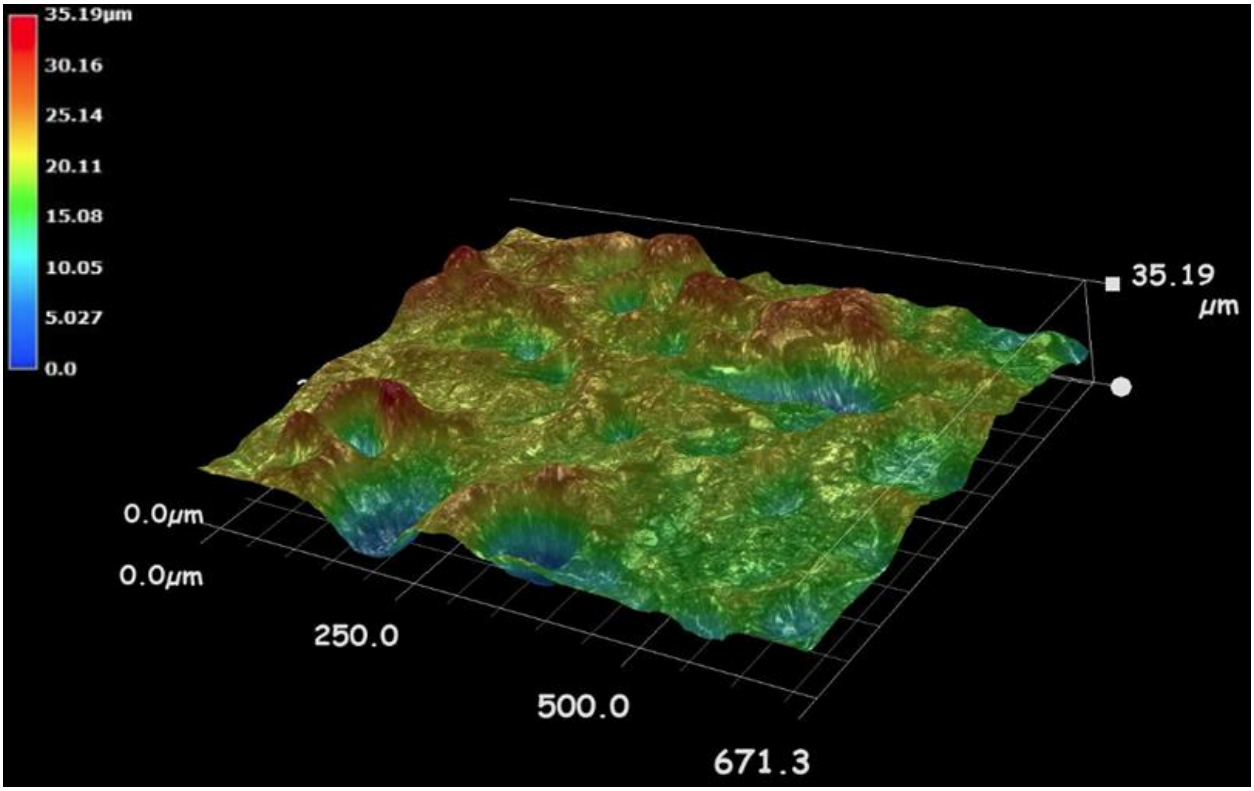

Figure 5.18: 3D image of aluminum 7075-T6 after grit blasted with 20 grit at 413 kPa (60 psi)

Pure aluminum coatings were deposited on aluminum 7075-T6 bond plugs. 5 bond plugs per surface preparation procedure were produced. Coatings were milled down to 400 µm thick to meet ASTM-C633 adhesion test standard.

Figure 5.19 shows the adhesion strength of pure aluminum coatings sprayed on aluminum 7075-T6 bond plugs with different surface roughness values.

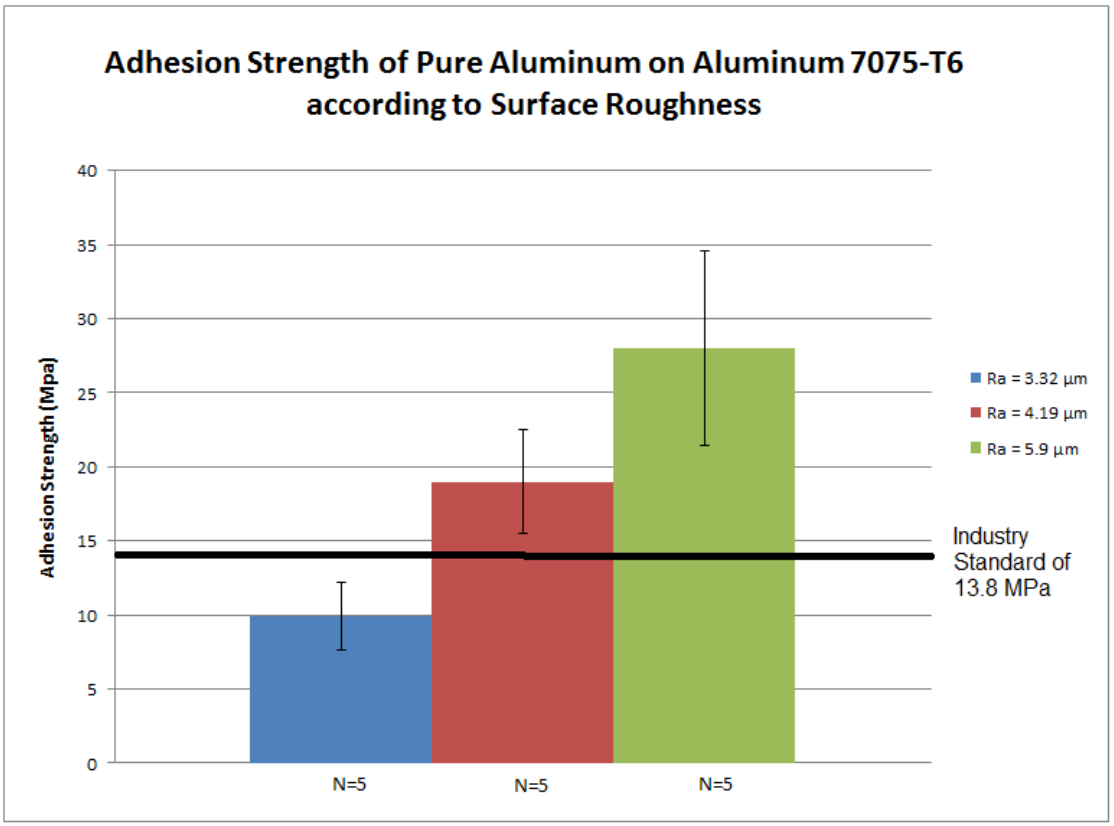

Figure 5.19: Adhesion strength of pure aluminum on aluminum 7075-T6 with respect to surface roughness

It is observed that the adhesion strength is directly related to the substrate surface roughness, confirming that the adhesion is predominantly due to mechanical anchoring. The first grit blasting parameter (steel grit at 1.37 MPa) produced the highest Ra value and adhesion strength. This is due to the higher surface of contact between the pure aluminum coating and the substrate. A rougher surface also allows aluminum particles to get trapped in cavities and act as anchors. The first grit blasting procedure was chosen to prepare the Taber abrasion panels.

The large standard deviations can be due to imbedded grits that lower the adhesion strength of the coatings. Imbedded grits can be reduced by leaving the substrates in an ultrasonic bath for about 10 to 15 minutes.

5.3.6 Taber Abrasion Test of Pure Aluminum on Aluminum 7075-T6 substrates

Spray parameters to produce pure aluminum coatings on aluminum 7075-T6 substrates were optimized to reduce the porosity level as well as maintaining the heat treatment of the substrate. The adhesion strength of the coating was increased to exceed the industry requirement of 13.8 MPa (2000 psi) by changing the surface preparation procedure. The last step to qualify the coatings is to perform the Taber abrasion test. This test consists of producing a 101.6 mm X 101.6 mm pure aluminum coating (between 1 and 1.5 mm thick) on aluminum 7075-T6 substrate (6.35 mm thick). The coating is then anodized at industry facility and followed by the Taber abrasion test presented in chapter 4.4.2 (ASTM D4060-10).

5.3.6.1 Previous Taber Abrasion Test Results

Figure 5.20 shows a Taber abrasion panel previously produced by MacDonald [45] that has failed to meet the industry requirement.

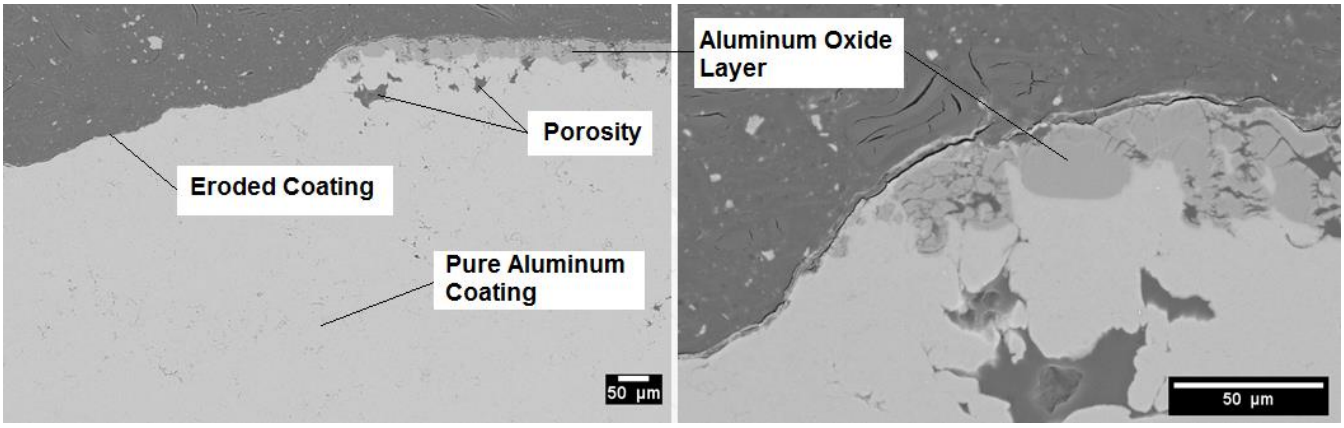

Figure 5.20: Cross-section of a pure aluminum Taber abrasion panel presented by MacDonald (adapted from [45])

The panel had a total weight loss of 550 mg after the wear test which is considerably higher than the industry maximum acceptable level of 20 mg. It is observed that the aluminum oxide layer has completely worn out during the test, even exposing the aluminum coating. It was established that the poor wear resistance of the aluminum oxide was caused by the non-uniform aluminum oxide layer built on the coating after being anodized. This non-uniformity can be observed on Figure 5.20. The oxide layer was not able to grow uniformly due to the high porosity in the coating. Taber abrasion test results were to be improved by producing denser pure aluminum coatings that would produce a more uniform oxide layer.

5.3.6.2 Taber Abrasion Panel

Figure 5.21 shows the experimental setup used to produce the Taber abrasion panels. The panel was insulated with carbon fiber plates to reduce heat transfer with the laboratory jack.

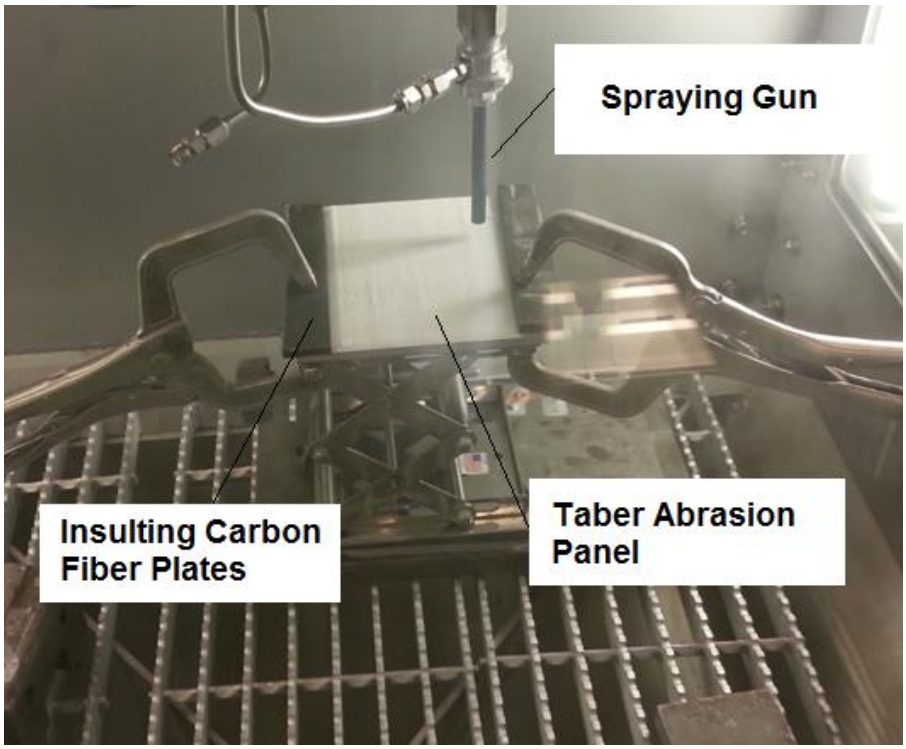

Figure 5.21: Experimental setup to produce the Taber abrasion panels

Figure 5.22 presents the aluminum 7075-T6 panel after being coated with pure aluminum. It is observed that the CGDS process produces a coating with rough surface.

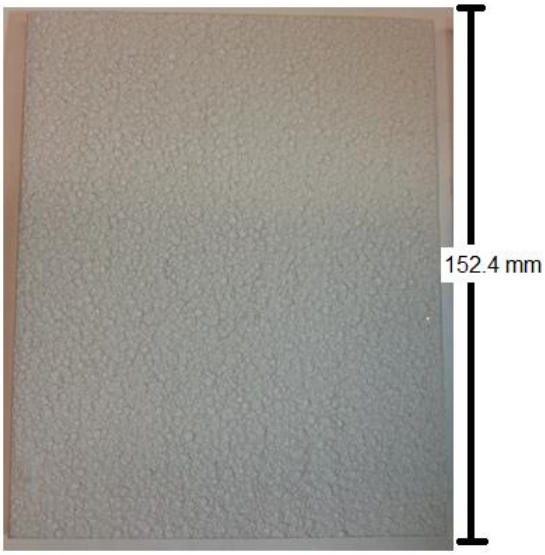

Figure 5.22: Taber abrasion panel prior to milling process

The coating is milled down to the required thickness (between 1 mm and 1.5 mm) to obtain a smooth and uniform surface. Figure 5.23 shows the final Taber abrasion panel that is sent to the industry`s facility to perform the anodizing process and the Taber test (ASTM D4060).

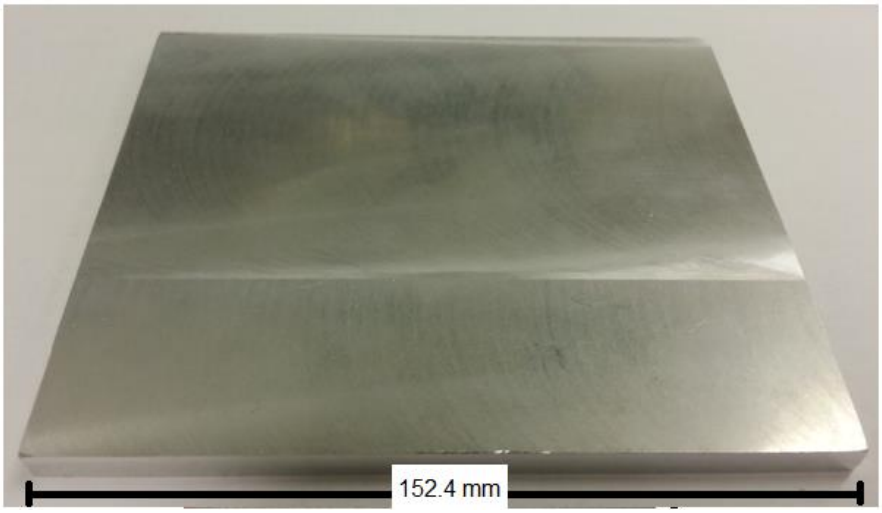

Figure 5.23: Taber abrasion panel after being machined down to the required thickness

5.3.6.3 Taber Abrasion Test Results

Four panels coated with pure aluminum were sent to the industry facilities. The samples were subjected to the anodizing process prior to perform the abrasion test. Table 5.10 presents the material loss after 10 000 cycles. It is to be noted that the test starts after 1000 cycles in order to remove surface imperfections.

Table 5.10: Taber panels weight loss after being subjected to the abrasion test

Panel ID	***Weight (g)***			***Weight Loss (mg)***			***Pass/Fail***
	0 cycle	1000 cycles	11000 cycles	1000 cycles	11000 cycles	**10000 cycles**	
1	172.841	172.839	172.819	2.0	22.6	**20.6**	Fail
2	168.663	168.660	168.639	3.6	24.4	**20.8**	Fail
3	151.034	151.030	151.008	3.2	25.8	**22.6**	Fail
4	174.186	174.182	174.151	3.9	35.0	**31.1**	Fail

The maximum material weight loss allowed after 10 000 cycles by the ASTM 4060-10 standard is 20 mg. It is observed that the four panels failed to meet the standard. However, an important improvement is noticed when comparing with McDonald's results which lost 550 grams during the process. Densifying the pure aluminum coatings allowed the oxide layer to grow more uniformly when anodized. The denser aluminum oxide film offered a much better wear resistance property to the coating. However, the use of CGDS for the restoration of damage aluminum parts was discarded by the aerospace industry. Improvements are still to be completed on the quality of pure aluminum coatings.

These results suggest new experiments to be completed in order to reduce porosity in pure aluminum coatings, grow a denser aluminum oxide layer and meet ASTM 4060-10 standard. These experiments might eventually be conducted on a more sophisticated CGDS system that can produce denser pure aluminum coatings. Development of new nozzles might also result in the production of denser pure aluminum coatings. Other

methods can also be used to increase the density of coatings. One of these methods is shot pinning. This process could be performed on the coating prior to the anodizing process. It would potentially decrease the porosity on the surface of the coating by hardly impinging it and improve the quality of the oxide film when anodized.

6. Nozzle Material Investigation

6.1. Observation

A feasibility analysis was performed using aluminum 7075 powder supplied by Valimet (Stockton, CA, USA) on aluminum 7075-T6 as mentioned in chapter 5.2.3. It was observed that the powder was not producing a coating on the substrate when the SST-EP polymer nozzle was used. Only few particles would adhere to the surface as seen on Figure 5.4 left. However, the HFSS nozzle produced dense coatings but eventually clogged after a few minutes of spray. The coating produced with stainless steel nozzle is shown on Figure 5.4 right.

6.2. Hypothesis

The initial hypothesis that could explain the results obtained in the previous chapter is the difference in nozzle geometries. The HFSS nozzle (see Figure 6.1 left) is produced by hydroforming manufacturing process that results in a smooth diverging section inside the nozzle (see Figure 6.2 left). The SST-EP polymer nozzle (see Figure 6.1 right) is manufactured using three different drill bit sizes that leave two steps inside of the nozzle (see Figure 6.2 right). Moreover, the exit to throat area ratio of the nozzle is slightly different causing the gas velocity to be dissimilar. Furthermore, the steps in the SST-EP

polymer nozzle might cause shockwaves that would drastically slow down the particles and affect the deposition efficiency.

It is believed that a polymer nozzle with the same geometry as the HFSS nozzle would produce identical coatings.

Figure 6.1: HFSS nozzle (left), SST-EP polymer nozzle (right)

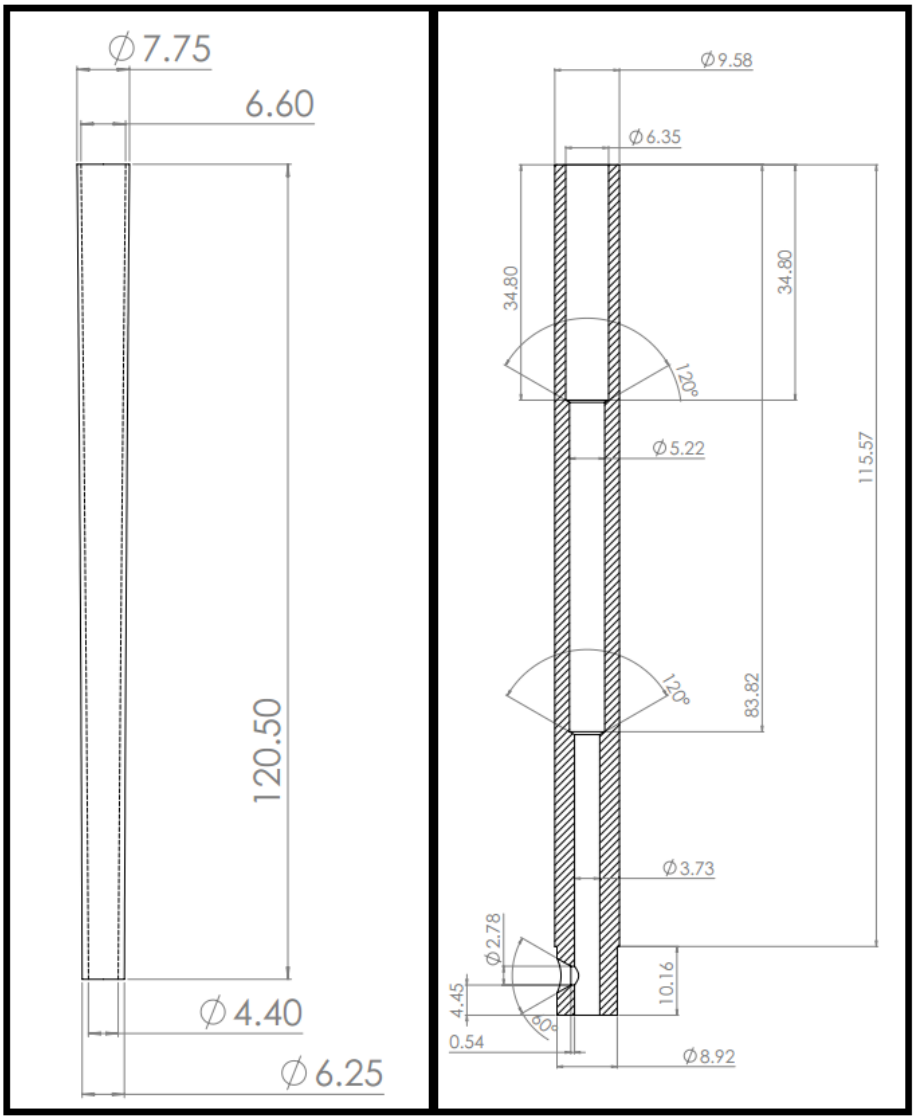

Figure 6.2: Cross-section of the HFSS nozzle (left), SST-EP polymer nozzle (right)

6.3. Experimental Setup

In order to validate the hypothesis, two nozzles with identical geometries but different materials have to be used. It was not possible to produce a polymer nozzle with the hydroforming process due to polymer low yielding property. It was chosen to manufacture a stainless steel nozzle (see Figure 6.3 right) with internal features similar to the SST-EP polymer nozzle (see Figure 6.3 left).

Figure 6.3: SST-EP Polymer nozzle (left), in-house stainless steel nozzle (right)

In a scenario where a coating would not be successfully produced with the in-house stainless steel nozzle, the geometry would be the cause of failure.

A trial using the SST-EP system equipped with the in-house stainless steel nozzle was performed. The spray parameters and the surface preparation used for the test are the same as the one found in chapter 5.2.3 and used when spraying with the SST-EP polymer nozzle.

6.4. Feasibility of Aluminum 7075 on Aluminum 7075-T6 using the in-house Stainless Steel Nozzle

In order to validate the hypothesis stated in the previous chapter (the difference in nozzle geometries affect the coating quality), an aluminum 7075 coating was produced on aluminum 7075-T6 substrate. The experiment resulted in producing a 2.45 mm thick coating (see Figure 6.4).

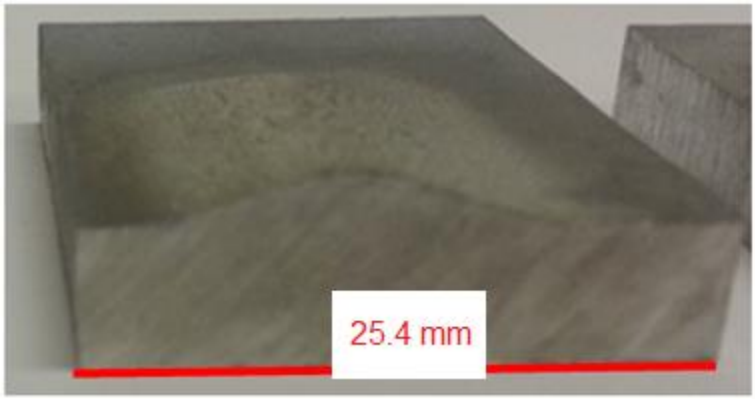

Figure 6.4: Aluminum 7075 coating on aluminum 7075-T6 substrate using the in-house stainless steel nozzle

This result discards the hypothesis that the different nozzle geometry of the SST-EP polymer nozzle is responsible for not producing coating. It rather seems to indicate that the deposition efficiency is largely influenced by the nozzle material.

6.5. New Hypotheses

The previous result demonstrates that the nozzle material has an effect on the deposition efficiency of aluminum 7075 powder. Two new hypotheses were brought up to explain the phenomenon occurring inside the nozzles. The phenomenon is most

likely occurring due to a difference in particles' kinetic energy, a difference in particles' thermal energy or a combination of both.

The first new hypothesis states that the aluminum 7075 particles hit the nozzle's wall after being injected radially with respect to the gas stream direction. The particles that bounce on the wall obtain more thermal energy from the stainless steel nozzle than the polymer nozzle. This effect would be caused by the large difference in thermal conductivity between Polybenzimidazole (0.41 W/m*K) and stainless steel 304 (16.2 W/m*K). The nozzles store thermal energy during the process. This thermal energy comes mostly from the friction occurring between the gas and the nozzle wall as well as from heat transfer between the two (convection and radiation). Thermal energy stored in the stainless steel nozzle is transferred back at a faster rate to the aluminum 7075 particles during the process.

The second hypothesis states that the polymer nozzle would soften when reaching high temperatures resulting into aluminum 7075 particles losing kinetic energy when hitting the inside wall. The critical velocity for aluminum 7075 would not be reached and particles would bounce off the substrate.

6.6. Second Experimental Setup

New nozzles were produced in order to validate or discard the hypotheses presented in the previous section. A copper nozzle (copper 110) and a ceramic nozzle (mica

ceramic) were manufactured with the exact same geometry as the SST-EP polymer and the in-house stainless steel nozzle.

The copper nozzle was produced to validate the first hypothesis due to its high thermal conductivity (401 W/m*K). If the first hypothesis is correct, a larger coating will be produce with the copper nozzle than with the in-house stainless steel nozzle.

The fourth nozzle was manufactured out of mica ceramic to validate the second hypothesis due to its low thermal conductivity of (1.47 W/m*K) and high hardness value of 250 Knoop. If the second hypothesis is accurate, particles will exit the ceramic nozzle at higher velocities and a coating will be produced. Figure 6.5 shows the four nozzles used for this experiment.

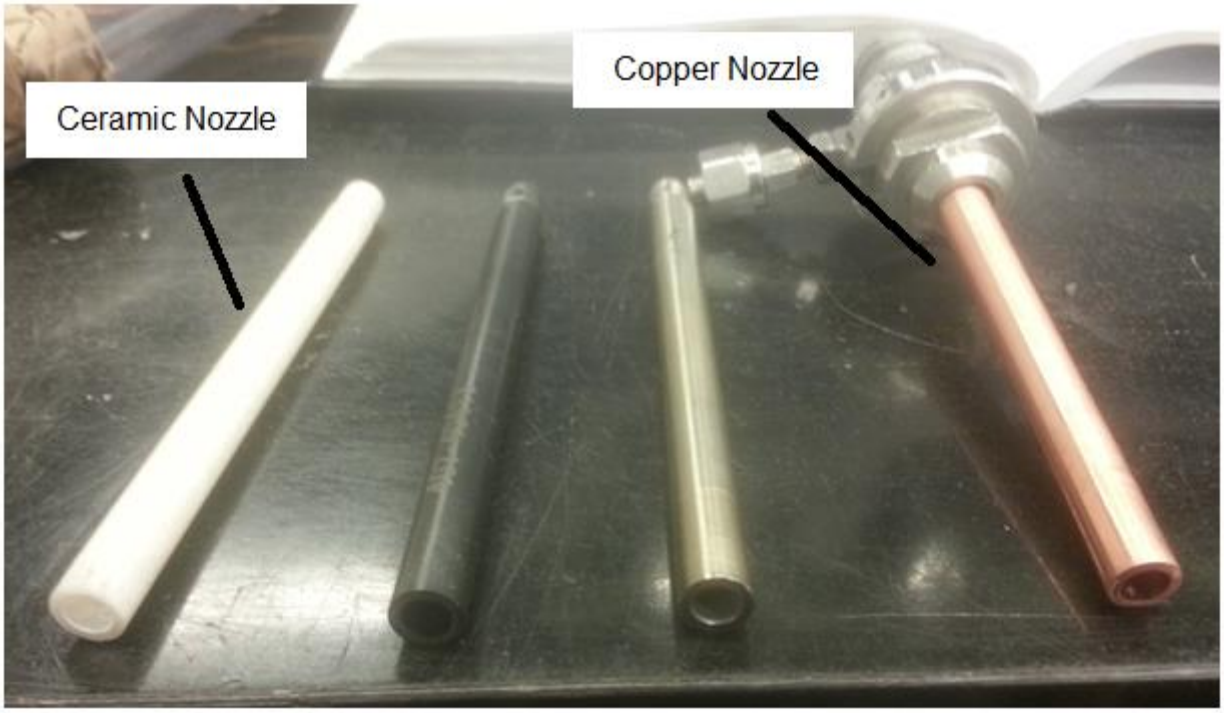

Figure 6.5: Four nozzles with the same geometry but made out of different material

6.7. Second Experimental Results

6.7.1. Coating of Aluminum 7075 Produced with the Ceramic and Copper Nozzle on Aluminum 7075-T6 Substrate

Coatings were produced using the same spray parameters and surface preparation procedure as the ones presented in chapter 5.3.3. The only variable that changed between attempts was the nozzle material. Figure 6.6 shows the aluminum 7075 coating produced on aluminum 7075-T6 substrate using the ceramic nozzle.

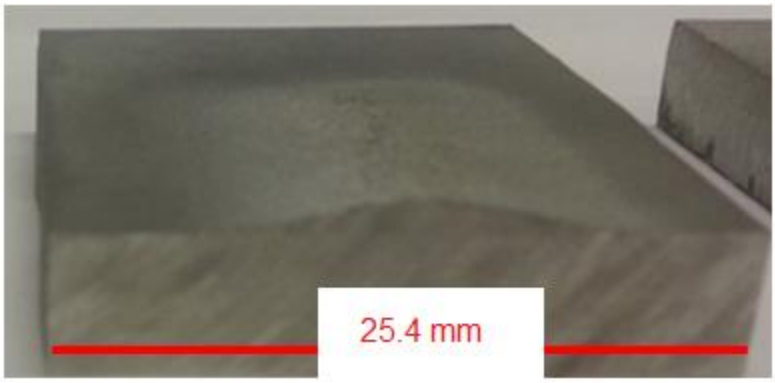

Figure 6.6: Aluminum 7075 coating on aluminum 7075-T6 substrate using the ceramic nozzle

It is demonstrated that a portion of the powder accelerated toward the substrate successfully adhered to the surface when using the ceramic nozzle to produce a 1.45 mm thick coating. This result would agree with the second hypothesis stating that the polymer nozzle slows down the particles due to its low hardness. However, the ceramic nozzle produced a thinner coating than the stainless steel nozzle even though mica ceramic and stainless steel 304 have similar hardness values (251 knoop). This phenomenon can only occur if the particles exiting the stainless steel nozzle have more energy than the ones exiting the ceramic nozzle. The particle velocity using different

nozzles is still to be determined in order to prove that the larger coating produced with the stainless steel nozzle is not caused by higher particle kinetic energy. Figure 6.7 shows the aluminum 7075 coating produced on aluminum 7075-T6 substrate using the copper nozzle.

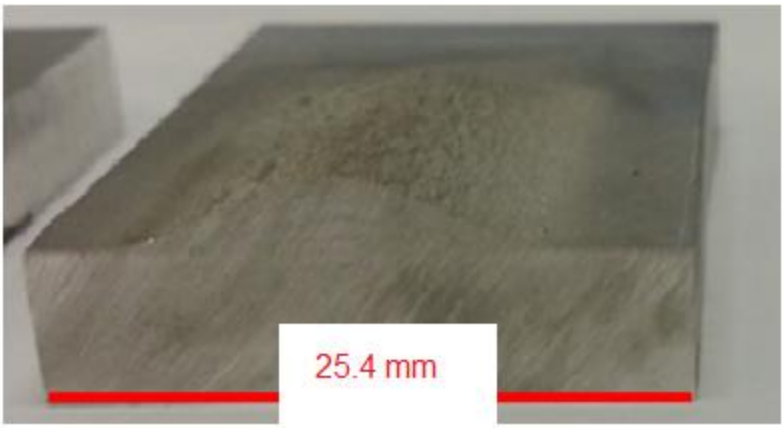

Figure 6.7: Aluminum 7075 coating on aluminum 7075-T6 substrate using the copper nozzle

It can be observed that the copper nozzle produced the thickest aluminum 7075 coating (3.08 mm). The aluminum 7075 particles have the highest amount of energy at the copper nozzle's exit. Further tests have to be performed in order to see if the particles have higher kinetic or thermal energy when exiting the copper nozzle.

6.7.2. Aluminum 7075 Coatings Microstructure

Coatings' microstructures were analyzed in order to understand the effect of the nozzle material on the quality of the coatings produced with the SST-EP system. Figure 6.8 shows the coating's cross-section produced with the polymer nozzle.

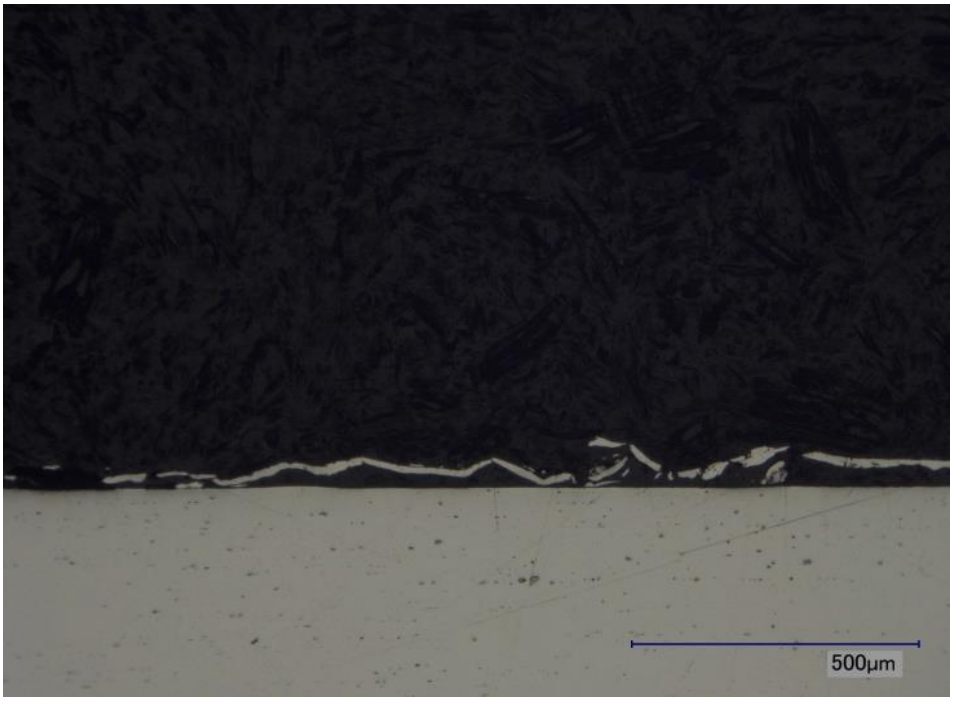

Figure 6.8: Cross-section of aluminum 7075 coatings produced with the polymer nozzle

It is observed that almost all of the sprayed particles hit the substrate and bounced off without adhering. Figure 6.9 represents the cross-section of the coating produced with the ceramic nozzle.

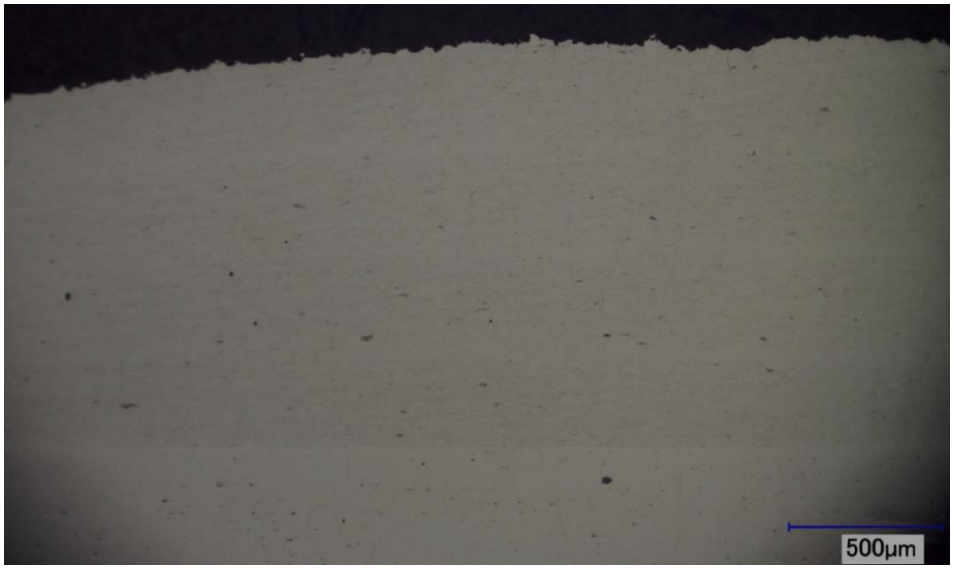

Figure 6.9: Cross-section of aluminum 7075 coatings produced with the ceramic nozzle

It can be observed that the 1.45 mm thick coating is dense and uniform. Its porosity level is below 0.5%. Figure 6.10 represents the cross-section of the coating produced with the stainless steel nozzle.

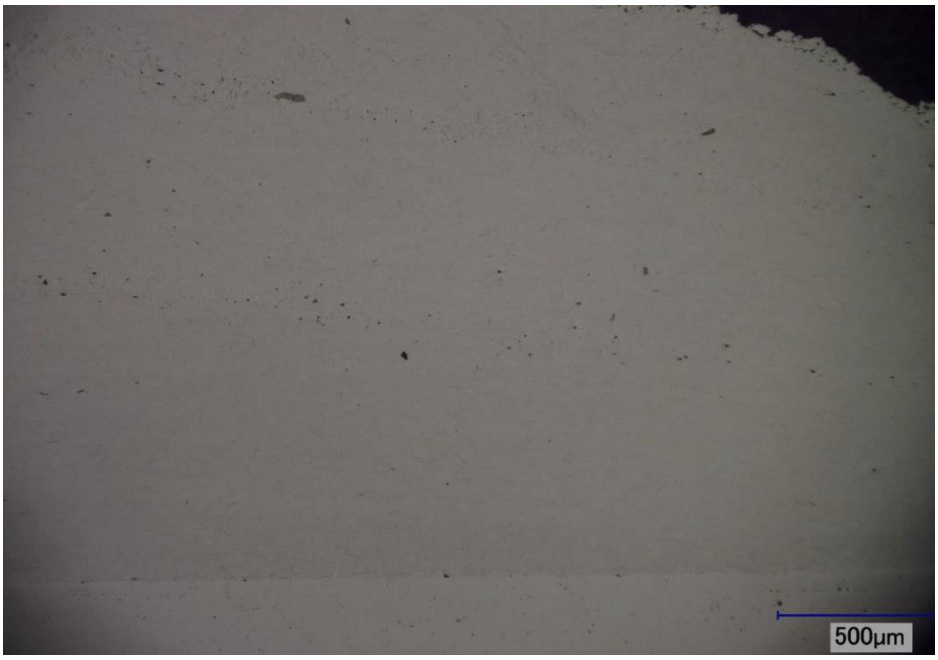

Figure 6.10: Cross-section of aluminum 7075 coatings produced with the homemade stainless steel nozzle

The 2.45 mm thick coating produced with the in-house stainless steel nozzle is slightly more porous than the coating produced with the ceramic nozzle. Its porosity level is also well below 0.5 %.

Figure 6.11 presents the cross-section of the coating produced with the copper nozzle.

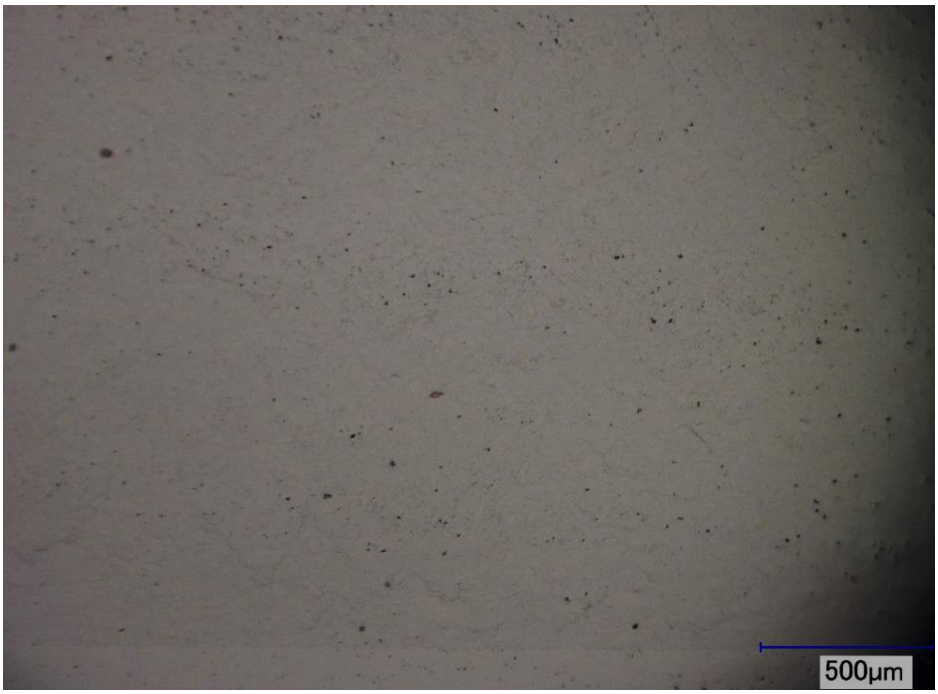

Figure 6.11: Cross-section of aluminum 7075 coatings produced with the copper nozzle

It is observed that the porosity level increased in the aluminum 7075 coating produced with the copper nozzle. The 3.08 mm thick coating reached a porosity level close to 0.5%.

Previous cross-section images demonstrate the correlation between coating thickness and porosity level. This phenomenon usually occurs in CGDS because larger particles don't get heat up as much as the smaller particles causing them to impinge the coating and bounce off. When impinging the coating, they deform the smaller particles and a denser coating is produced. This is called the hammering effect. It can be assumed that particles exiting the ceramic nozzle do not get warmed up as much as the particles exiting the copper nozzle resulting into lower deposition efficiency (thinner coating) but

with an increase of impingement that densifies the coating. Further tests have to be performed to explain this phenomenon.

6.7.3. Particle Velocity Analysis

The previous section suggested that the particles exiting the copper nozzle have the most energy resulting in higher deposition efficiency. In order to explain whether the increase in deposition efficiency was caused by higher kinetic or thermal energy, particle velocity measurements were performed using the four different nozzles. This experiment was performed using Tecnar Cold Spray Meter. Table 6.1 shows the average particle velocity exiting the four different nozzles, with the respective coating thickness obtained.

.

Table 6.1: Average particle velocity exiting the four different nozzles and coating thickness

Nozzle Material	***Average Particle Velocity (m/s)***	***Coating Thickness (mm)***
Polymer	624 +/- 64	~0
Ceramic	549 +/- 103	1.45
Stainless Steel	545 +/- 90	2.45
Copper	466 +/- 108	3.08

It is observed that the particle velocity measurements are inversely proportional to the deposition efficiency (coating thickness). The particles with less kinetic energy produced

the thicker coatings. These results are in contradiction with what is usually experienced in CGDS. These results bring up two more questions. Why would the particles exiting more conductive nozzles be slower? Why would the slowest particles adhere more efficiently to the substrate?

6.7.4. Tests Performed with Insulated Stainless Steel and Copper Nozzles

The particle velocity measurements were performed once again using the in-house stainless steel and copper nozzles but with insulation on the nozzle's exterior wall. The goal was to find an explanation to the first question asked in the previous section. The driving gas is potentially giving away more heat through conduction and convection when using highly conductive materials. This would result in a lower driving gas temperature and velocity and could explain why particles exiting the copper nozzle are considerably slower. Table 6.2 shows the results of particle velocity and coating thickness using the insulated nozzles.

Table 6.2: Average particle velocity and coating thickness using insulated stainless steel and copper nozzles

Nozzle Material	***Average Particle Velocity (m/s)***	***Coating Thickness (mm)***
Insulated Stainless Steel	562 +/- 81	2.77
Insulated Copper	487 +/- 93	4.21

It is observed that insulating nozzles did not have a large influence on the particle velocity. This demonstrates that the driving gas energy lost through conduction and convection is very low with respect to its total energy.

However, insulating nozzles resulted in an increase in coating thickness. This is most likely caused by the interaction between the nozzle inner wall and the particles through the process. The insulated nozzle inner wall temperature is greater, allowing particles to gain additional thermal energy. Warmer particles result in higher deposition efficiency and greater coating thickness. This effect is amplified when a highly conductive material is used. For instance, the insulated in-house stainless steel nozzle produced a coating 320 µm thicker, but insulating the copper nozzle resulted in a coating thickness increase of 1130 µm.

6.7.5. Thermal Diffusivity of the Nozzles

Previous results demonstrated the importance of the interaction between particles and nozzle inner wall. It was observed that the deposition efficiency of aluminum 7075 on aluminum 7075-T6 seems to correlate with the thermal conductivity of the nozzle's material. The thermal conductivity can also be expressed in terms of thermal diffusivity which represents the ability of a material to give away heat over its ability to store it:

$$\alpha = \frac{k}{\rho C_p} \tag{6.1}$$

where k represents the thermal conductivity of the material, ρ its density and C_p its specific heat capacity. Table 6.3 shows the correlation between the coating thickness of aluminum 7075 and the thermal diffusivity of the nozzle's material.

Table 6.3: Correlation between coating thickness and nozzle thermal diffusivity

Nozzle Material	*Thermal Diffusivity (m^2/s)*	*Coating Thickness (mm)*
Polymer	3.39×10^{-7}	~0
Ceramic	1.31×10^{-6}	1.45
Stainless Steel	3.75×10^{-6}	2.45
Copper	1.15×10^{-4}	3.08

It is observed that the coating thickness is not linearly proportional to the thermal diffusivity. Even though copper has a thermal diffusivity almost 88 times higher than mica ceramic, the coating produced is only twice the thickness. This is mainly caused by the lower average particle velocity exiting the copper nozzle. More experiments were performed using the four different nozzles in order to explain the large average particle velocity difference.

6.7.6. Single particle tests

Single particle tests were performed using aluminum 7075 powder on polished aluminum 7075-T6 substrates. This experiment is done by moving the spray gun at high speed over the substrate in order to catch single particle impacting the substrate.

The goal of these tests is to demonstrate if particle/nozzle wall interaction can lead to particle deformation while in the nozzle (smearing effect). This could occur when

particles hit the inner nozzle's wall and get soften or/and deformed prior to hitting the substrate. As a result of those interactions, the particles could potentially lose momentum at the expense of plastic deformation of the particles upon impact and would explain the difference in average particle velocity exiting the 4 different nozzles. Figure 6.12 (left) shows an SEM image of the aluminum 7075 powder and Figure 6.12 (right) shows an SEM image of a single aluminum 7075 particle that has impacted the aluminum 7075-T6 substrate when using the SST-EP polymer nozzle.

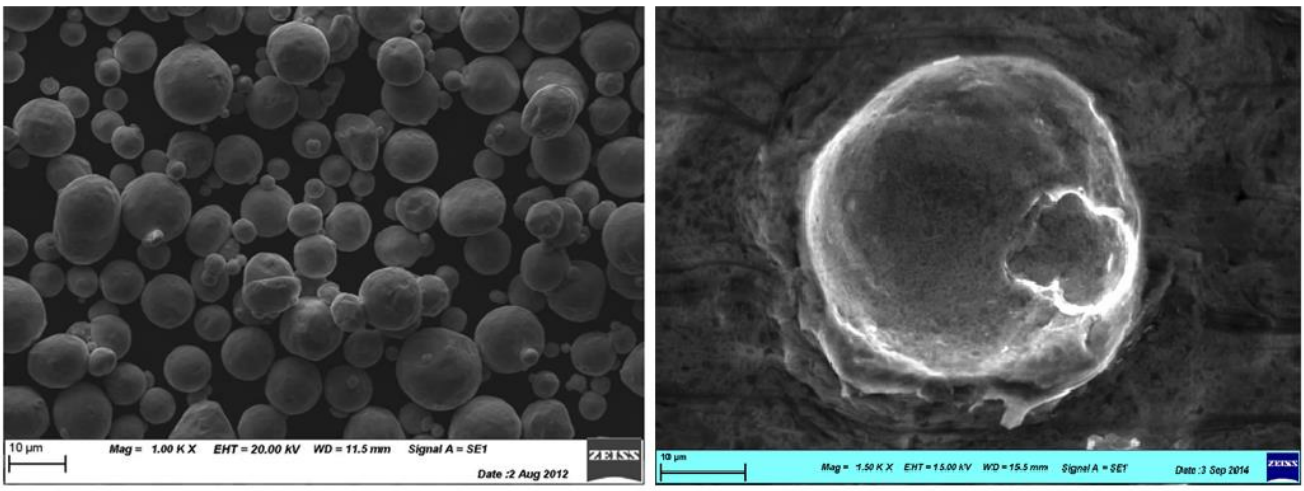

Figure 6.12: SEM image of aluminum 7075 powder (AA7075-200 mesh (Valimet) (left), SEM image of an aluminum 7075 particle on aluminum 7075-T6 substrate sprayed with the SST-EP polymer nozzle (right)

It is observed that the particle did not deform upon impact with the substrate. It has rather penetrated in the substrate. Particle jetting can be seen around the particle. This picture describes what is occurring when aluminum 7075 is sprayed on aluminum 7075-T6 using the SST-EP polymer nozzle. It shows that the particle has a lot of momentum (when referring to the particle velocity analysis presented in Table 6.1) before hitting the substrate but has low thermal energy. Its thermal energy is assumed to be low because its ductility is low. The particle rather penetrates the substrate instead of deforming. This

test also shows that the particle is still spherical when exiting the nozzle and smearing effect is not occurring in the SST-EP polymer nozzle.

It was also observed that only few particles managed to adhere when using the SST-EP polymer nozzle. The larger aluminum 7075 particles did not have enough energy to adhere. Figure 6.13 shows a trace left by a large particle that bounced off the substrate.

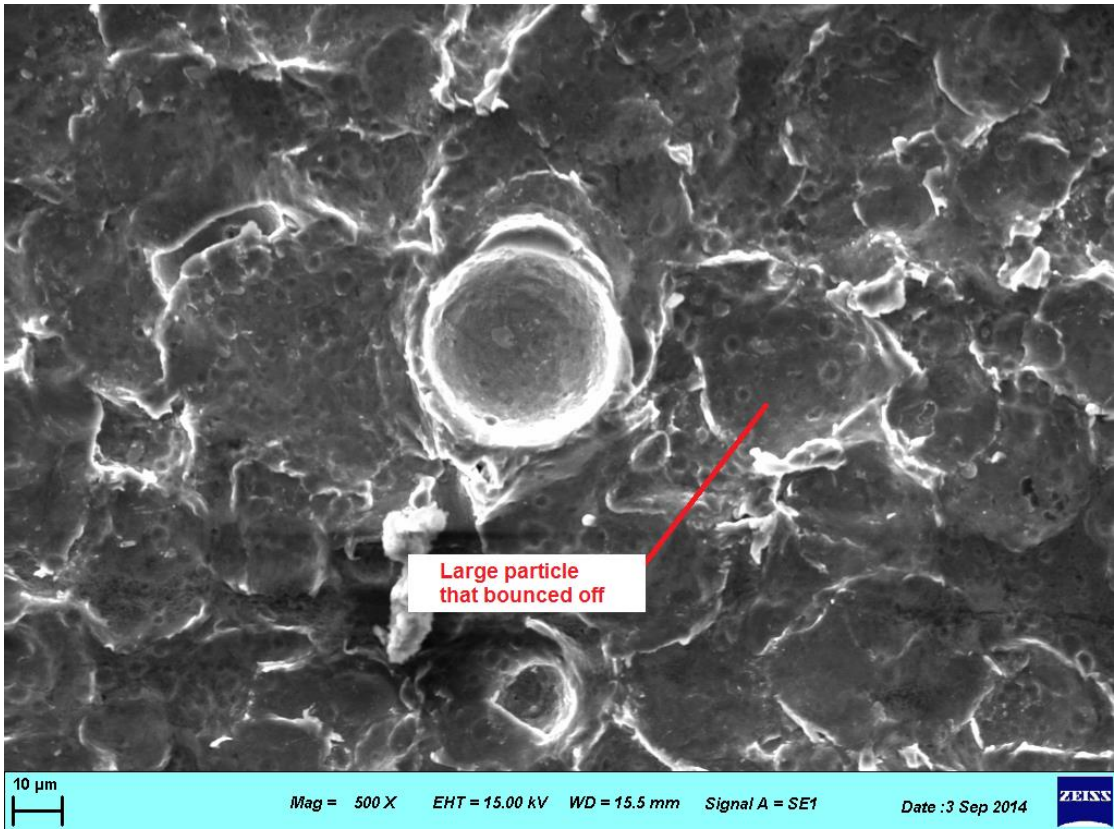

Figure 6.13: SEM image of a large aluminum 7075 particle that bounced off the substrate after impact

This test explains why coatings are not successfully formed when using the SST-EP polymer nozzle. In fact, even if particles exiting the nozzle reach higher velocities, they cannot pick up enough heat when hitting the polymer nozzle's wall (due to its low thermal diffusivity) to form a coating. It was mentioned in Chapter 2 that the critical

velocity of a material, in cold spray, is proportional to its temperature. There is still no technology available to experimentally measure the particles' temperature exiting the nozzle. However, by showing the interaction between a particle and the substrate and by knowing the particle velocity, an accurate comparison in terms of particle temperature can be done.

The single particle test was performed using the 3 other nozzles. If the powder get soften by the nozzle's wall, the particles were expected to be deformed and non-spherical. Figure 6.14, Figure 6.15 and Figure 6.16 show SEM images of a single aluminum 7075 particle that has impacted the aluminum 7075-T6 substrate using the three different nozzle.

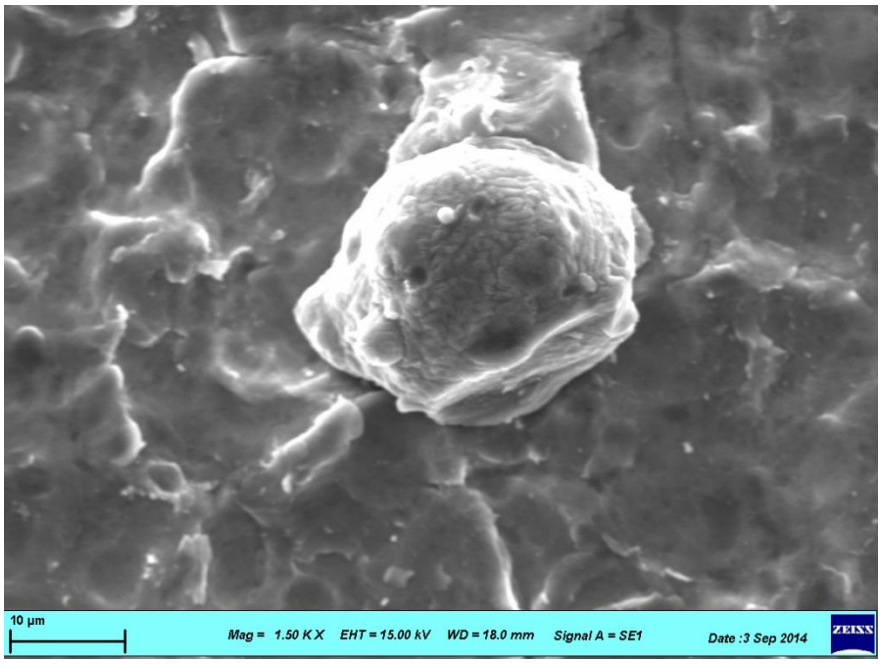

Figure 6.14: SEM image of an aluminum 7075 particle on aluminum 7075-T6 substrate sprayed with the ceramic nozzle

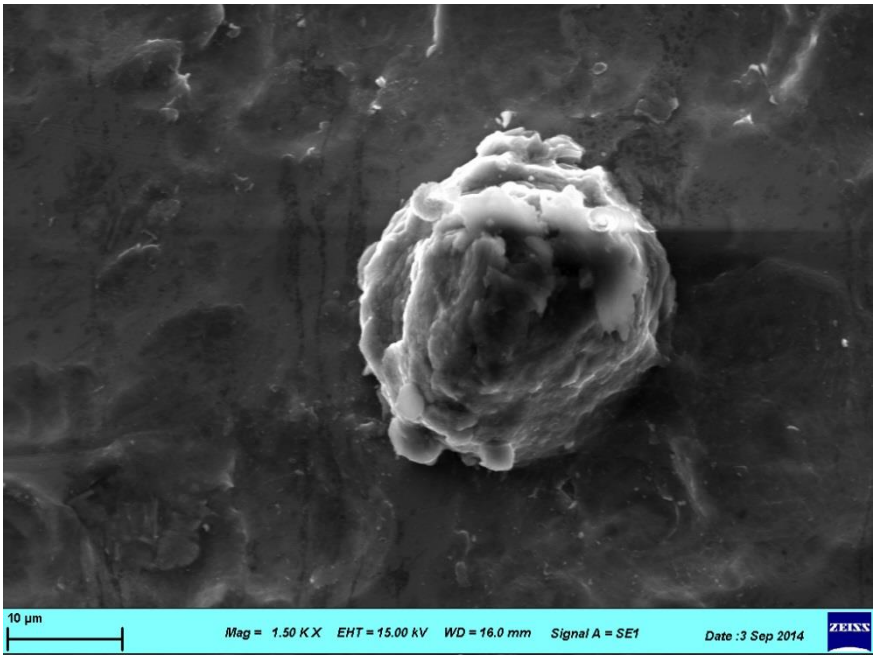

Figure 6.15: SEM image of an aluminum 7075 particle on aluminum 7075-T6 substrate sprayed with the stainless steel nozzle

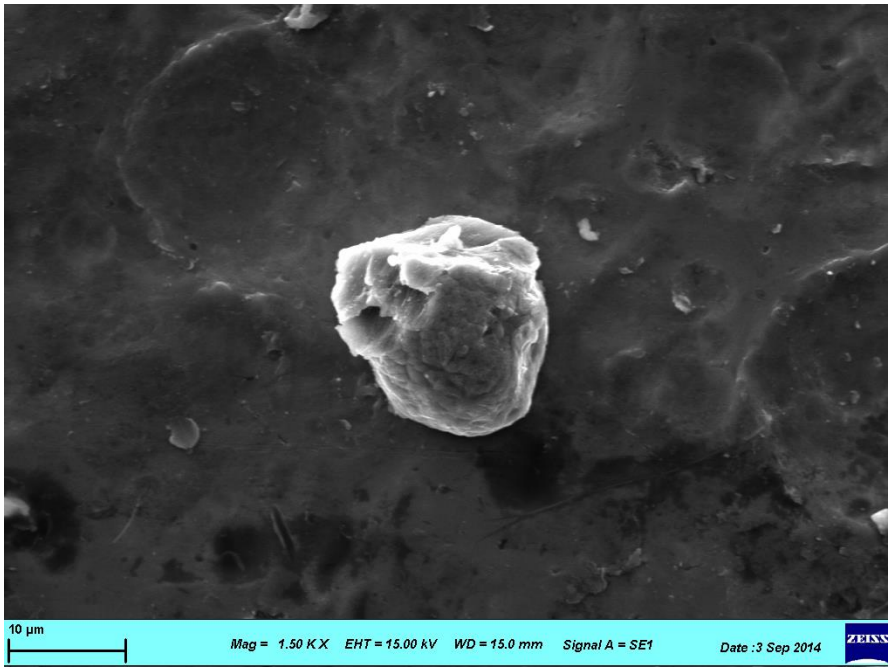

Figure 6.16: SEM image of an aluminum 7075 particle on aluminum 7075-T6 substrate sprayed with the copper nozzle

It is observed that particles have deformed upon impacts but also by potentially shearing on the nozzle's wall prior to hit the substrate. It is to be noted that substrate jetting is no longer apparent on these three images. This is mainly caused by a combination of two factors. The particles have less kinetic energy upon impact and they have higher thermal energy due to the interaction they have with the nozzle wall (in comparison with the results obtained using the SST-EP polymer nozzle). The softened particles hit the substrate and deform. The substrate does not get hammered as much by the particles resulting in unapparent substrate jetting.

However, thermal energy lowers the critical velocity of the particles and allows the particles to adhere to form a coating. The deposition efficiency is higher when using the copper nozzle for instance because it is assumed that the particles are warmer, even if they have less kinetic energy.

It is also observed that smearing effect occurs on particles inside the ceramic, stainless steel and copper nozzle. Particles hit the nozzle's wall, heat up, deform and consequently lose kinetic energy. Figure 6.17 shows the potential trajectory of an aluminum 7075 particle inside the nozzle.

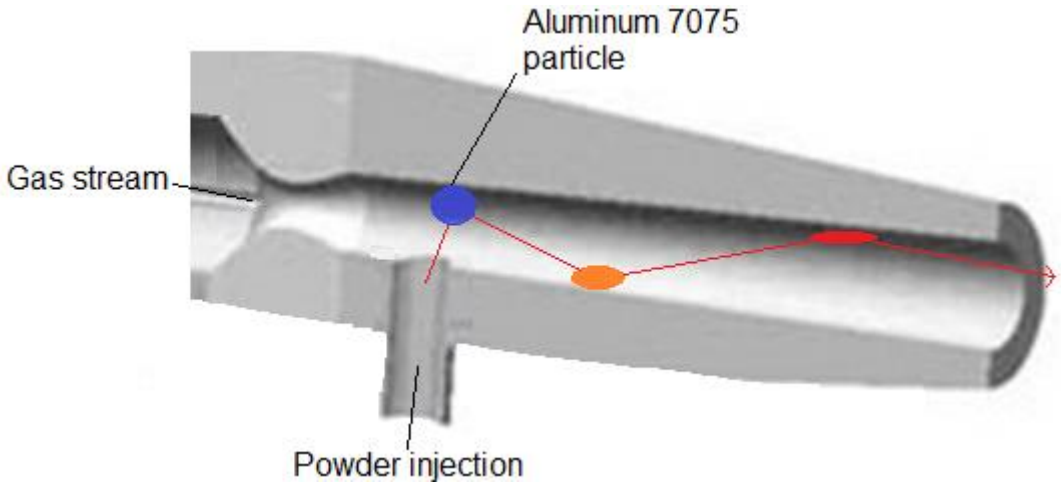

Figure 6.17: Trajectory of an aluminum 7075 particle when bouncing on the nozzle's wall

The particle enters the diverging section of the nozzle at low temperature. It then hits the nozzle's wall due to its initial axial velocity. The nozzle's wall, which is theoretically at stagnation gas temperature, gives away some of his energy to the particle. By warming up, the particles become softer and deform upon subsequent impacts slowing them down. This explains the correlation between nozzle material's thermal diffusivity (affects particles temperatures), deposition efficiency (warmer particles requires less kinetic energy to adhere to the surface) and particles velocity (warmer particles deform more upon impact and do not accelerate as much inside the nozzle).

This summarizes the effect of nozzle material on deposition efficiency and coating quality of aluminum 7075 on aluminum 7075-T6 substrate.

6.7.7. Erosion in the Polymer Nozzle

The previous section concluded with the importance of the interaction between particles and the nozzle wall. It was determined that the particles were gaining heat when hitting the wall and also deforming as a result of these interactions, thus losing momentum. However, it was observed that erosion occurred inside the SST-EP polymer nozzle after hours of spraying time. Figure 6.18 shows a cross-section of the SST-EP polymer nozzle.

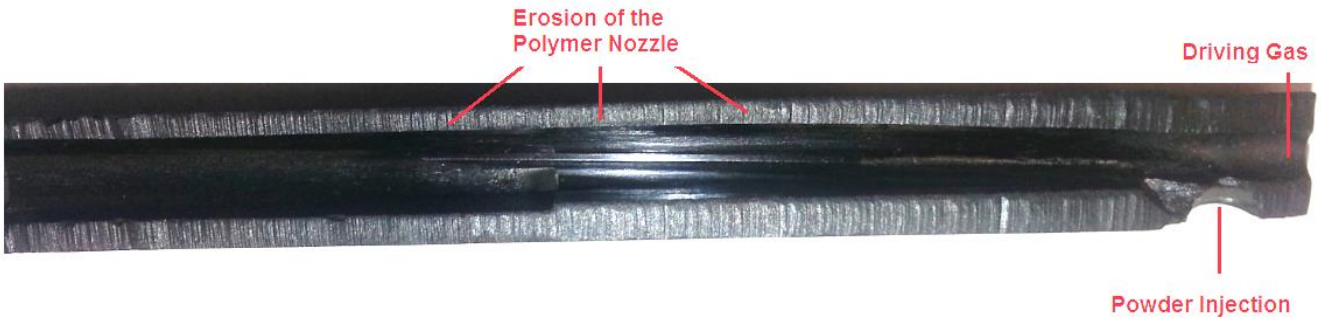

Figure 6.18: Erosion occurring inside the polymer nozzle

It is observed that erosion occurs on the opposite side of the powder injection point. This shows that particles tend to slide along the nozzle's wall as opposed to bounce. This discovery agrees with the theory that states that the particles gain heat by contacting the nozzle inner wall, but lose momentum due to friction and smearing effect. However, it shows that the particles are in contact with the nozzle wall for a much longer period of time. It also demonstrates that the interaction between the particles and the nozzle is a major aspect of the cold spray process. This aspect has been not been investigated before and potentially opens a new field of research on the effect of nozzle erosion on the spray quality.

6.8. Final Explanation

Chapter 6 discussed of a phenomenon that was never mentioned in CGDS. Emphasis has always been on nozzle geometry and spray parameters. The interaction of the particles with the nozzle wall was never investigated before.

The final explanation is that the particles, being injected axially, tend to slide along the nozzle's wall while being accelerated. In this process, high thermal diffusivity of the nozzle results in an increase in particles' temperature. The smearing effect tends to lower the kinetic energy of warm particles. However, even though warm particles are exiting the nozzle with less velocity, their critical velocity has been lowered enough to still increase the deposition efficiency.

It is to be mentioned that the in-house stainless steel and copper nozzles tend to clog after few minutes of spraying time. The polymer nozzle erodes over time but powder doesn't adhere to its wall. The ceramic nozzle doesn't seem to erode rapidly when using aluminum 7075 as feedstock material and the nozzle did not clog during all the tests performed. It is to be mentioned that the clogged nozzles were cleaned by using a sodium hydroxide solution to dissolve the aluminum.

As for industrial purposes, the ideal nozzle would be made out of a material that has high thermal diffusivity and would not clog. Ceramic does not have the highest thermal diffusivity, but there be advantages of using it commercially instead of the polymer nozzle. Firstly, it is possible to produce coatings with a wider range of feedstock

materials, for instance aluminum 7075. But it could also be possible to duplicate coatings sprayed with the polymer nozzle (similar DE) using lower stagnation temperature and pressure. Cold spray systems could be down sized and the energy consumption lowered.

7. Concluding Remarks

7.1. Conclusions

The research project was motivated by MacDonald`s previous work. The main goal was to improve the quality of the aluminum 7075 and pure aluminum coatings in order to obtain a denser and more uniform oxide layer once anodized. A denser oxide layer should increase the wear resistance of the coating in order to meet the industry requirement of a maximum weight loss of 20 mg when subjected to ASTM D4060 standard test.

The first part of the thesis conducted a feasibility study on producing pure aluminum and aluminum 7075 coatings using the new SST-EP system and nitrogen as the driving gas. It was found that aluminum 7075 coatings were not successfully produced when using the new CGDS system with its SST-EP polymer nozzle. On the other hand, the quality of the pure aluminum coatings were improved when using a high gas stagnation pressure (3.1 MPa) and a low gas stagnation temperature (300°C). The formation of these dense coatings depends on impingement effect. Smaller particles get faster and warmer and adhere to the substrate while the larger particles hammer the coating and

bounce off. This result in a low deposition efficiency process with high residual stress induced in the coatings. That caused the adhesion strength of the pure aluminum coatings to fall below the industry requirement (13.8 MPa) when using these new parameters. A new surface preparation procedure was implemented to increase the roughness of the substrate and enhance the surface contact area with the coating.

The section part of the thesis considered the influence of the nozzle material on the deposition efficiency of aluminum 7075 on aluminum 7075-T6 substrate. It was discovered that the nozzle material`s thermal diffusivity had a major impact on the DE. The interaction between the particles and the nozzle`s wall has been neglected previously by the CGDS industry. It was showed that the particle`s critical velocity was lowered with an increase in particle temperature. The particles get preheated by shearing on the nozzle`s wall. Higher the thermal diffusivity of the nozzle, the higher temperature the particles reach before hitting the substrate.

7.2. Recommendations and Future Work

This research project has provided results and answers to CGDS principals. Further work could be performed to expand the theory behind the effect of nozzle material in CGDS.

1. It was determined that the particles exiting the copper nozzle were a lot slower than the particles exiting the polymer nozzle. The cause of this phenomenon is

still not well understood. Further work could be completed on the effect of the nozzle`s inner wall surface roughness on the particle`s velocity.

2. It would be interesting to also evaluate the effect of the nozzle material on other types of powder.
3. Simulations could be performed to evaluate the interaction of the powder with the nozzle's wall. The powder injection axial velocity might have a large influence on the spray and was neglected by the CGDS industry.
4. It would be interesting to evaluate if the deformation of the particles in the ceramic, stainless steel and copper nozzles is caused by the heat gained by the particles, the surface roughness of the inner nozzle's wall or a combination of both.
5. Other materials could be used to manufacture the nozzle in order to optimize its thermal diffusivity, while minimizing clogging and nozzle erosion. A nozzle could be coated with a diamond layer (high thermal conductivity) to maximize deposition efficiency and minimize erosion/clogging issue.

References

[1] A. Heinz, A. Haszler, C. Keidel, S. Moldenhauer, R. Benedictus, and W. S. Miller, “Recent development in aluminium alloys for aerospace applications,” *Mater. Sci. Eng. A*, vol. 280, no. 1, pp. 102–107, Mar. 2000.

[2] A. C. Okafor, N. Singh, U. E. Enemuoh, and S. V. Rao, “Design, analysis and performance of adhesively bonded composite patch repair of cracked aluminum aircraft panels,” *Compos. Struct.*, vol. 71, no. 2, pp. 258–270, Nov. 2005.

[3] T. Dursun and C. Soutis, “Recent developments in advanced aircraft aluminium alloys,” *Mater. Des.*, vol. 56, pp. 862–871, Apr. 2014.

[4] E. A. Starke Jr. and J. T. Staley, “24 - Application of modern aluminium alloys to aircraft,” in *Fundamentals of Aluminium Metallurgy*, R. Lumley, Ed. Woodhead Publishing, 2011, pp. 747–783.

[5] J. R. Davis, *Handbook of Thermal Spray Technology*. ASM International, 2004.

[6] “Boeing delivers first 787 Dreamliner,” *Reinf. Plast.*, vol. 55, no. 6, p. 4, Nov. 2011.

[7] M. Peters and C. Leyens, “Aerospace and Space Materials,” *Materials Science and Engineering*, vol. Vol. III.

[8] W. D. C. Jr and D. G. Rethwisch, *Materials Science and Engineering: An Introduction*, 8th edition. Hoboken, NJ: John Wiley and Sons, 2009.

[9] O. Jilani, N. Njah, and P. Ponthiaux, “Corrosion properties of anodized aluminum: Effects of equal channel angular pressing prior to anodization,” *Corros. Sci.*, vol. 89, pp. 163–170, Dec. 2014.

[10] Z. Gao, H. Li, Y. Lai, Y. Ou, and D. Li, “Effects of minor Zr and Er on microstructure and mechanical properties of pure aluminum,” *Mater. Sci. Eng. A*, vol. 580, pp. 92–98, Sep. 2013.

[11] F. C. Campbell, *Elements of Metallurgy and Engineering Alloys*. ASM International, 2008.

[12] G. E. Totten and D. S. MacKenzie, *Handbook of Aluminum: Volume 2: Alloy Production and Materials Manufacturing*. CRC Press, 2003.

[13] A. D. Juhl, “Overview of anodizing in the aerospace industry,” *Met. Finish.*, vol. 108, no. 2, pp. 20–21, Feb. 2010.

[14] I. Tsangaraki-Kaplanoglou, S. Theohari, T. Dimogerontakis, Y.-M. Wang, H.-H. (Harry) Kuo, and S. Kia, “Effect of alloy types on the anodizing process of aluminum,” *Surf. Coat. Technol.*, vol. 200, no. 8, pp. 2634–2641, Jan. 2006.

[15] C. A. Grubbs, “Anodizing of aluminum,” *Met. Finish.*, vol. 105, no. 10, pp. 397–412, 2007.

[16] P. Reybet Degat, Z. R. Zhou, and L. Vincent, “Effect of chromic acid anodizing treatment on fretting behaviour during fretting tests on pre-stressed specimens,” *Thin Solid Films*, vol. 298, no. 1–2, pp. 170–176, Apr. 1997.

[17] L.-M. Berger, “Application of hardmetals as thermal spray coatings,” *Int. J. Refract. Met. Hard Mater.*

[18] H. Herman, S. Sampath, and R. McCune, “Thermal Spray: Current Status and Future Trends,” *MRS Bull.*, vol. 25, no. 07, pp. 17–25, 2000.

[19] M. R. Dorfman, “19 - Thermal Spray Coatings,” in *Handbook of Environmental Degradation of Materials (Second Edition)*, M. Kutz, Ed. Oxford: William Andrew Publishing, 2012, pp. 569–596.

[20] G. Mauer, A. Hospach, and R. Vaßen, “Process development and coating characteristics of plasma spray-PVD,” *Surf. Coat. Technol.*, vol. 220, pp. 219–224, Apr. 2013.

[21] M. Gell, L. Xie, X. Ma, E. H. Jordan, and N. P. Padture, “Highly durable thermal barrier coatings made by the solution precursor plasma spray process,” *Surf. Coat. Technol.*, vol. 177–178, pp. 97–102, Jan. 2004.

[22] A. P. Newbery and P. S. Grant, “Oxidation during electric arc spray forming of steel,” *J. Mater. Process. Technol.*, vol. 178, no. 1–3, pp. 259–269, Sep. 2006.

[23] C. Sun, L. Guo, G. Lu, Y. Lv, and F. Ye, “Interface bonding between particle and substrate during HVOF spraying,” *Appl. Surf. Sci.*, vol. 317, pp. 908–913, Oct. 2014.

[24] S.-W. Myoung, Z. Lu, Y.-G. Jung, B.-K. Jang, and U. Paik, “Control of bond coat microstructure in HVOF process for thermal barrier coatings,” *Surf. Coat. Technol.*, vol. 260, pp. 63–67, Dec. 2014.

[25] T. H. Van Steenkiste, J. R. Smith, R. E. Teets, J. J. Moleski, D. W. Gorkiewicz, R. P. Tison, D. R. Marantz, K. A. Kowalsky, W. L. Riggs II, P. H. Zajchowski, B. Pilsner, R. C. McCune, and K. J. Barnett, “Kinetic spray coatings,” *Surf. Coat. Technol.*, vol. 111, no. 1, pp. 62–71, Jan. 1999.

[26] V. K. Champagne, *The Cold Spray Materials Deposition Process: Fundamentals and Applications*. Elsevier, 2007.

[27] A.P. Alkhimov, A.N. Papyrin, V.F. Kosarev, N.I. Nesterovich, M.M. Shushpanov, US Patent 5 302 414, “Gas-Dynamic Spraying Method for Applying a Coating”, April 12, 1994.

[28] A. Papyrin, V. Kosarev, S. Klinkov, A. Alkhimov, and V. M. Fomin, *Cold Spray Technology*. Elsevier, 2006.

[29] E. Irissou, J.-G. Legoux, A. N. Ryabinin, B. Jodoin, and C. Moreau, “Review on Cold Spray Process and Technology: Part I—Intellectual Property,” *J. Therm. Spray Technol.*, vol. 17, no. 4, pp. 495–516, Dec. 2008.

[30] H. Ye and J. Wang, “Preparation of aluminum coating on Lexan by cold spray,” *Mater. Lett.*, vol. 137, pp. 21–24, Dec. 2014.

[31] M. Grujicic, J. R. Saylor, D. E. Beasley, W. S. DeRosset, and D. Helfritch, “Computational analysis of the interfacial bonding between feed-powder particles and the substrate in the cold-gas dynamic-spray process,” *Appl. Surf. Sci.*, vol. 219, no. 3–4, pp. 211–227, Dec. 2003.

[32] S. Grigoriev, A. Okunkova, A. Sova, P. Bertrand, and I. Smurov, “Cold spraying: From process fundamentals towards advanced applications,” *Surf. Coat. Technol.*

[33] T. Schmidt, H. Assadi, F. Gärtner, H. Richter, T. Stoltenhoff, H. Kreye, and T. Klassen, “From Particle Acceleration to Impact and Bonding in Cold Spraying,” *J. Therm. Spray Technol.*, vol. 18, no. 5–6, pp. 794–808, Dec. 2009.

[34] J. Wu, H. Fang, S. Yoon, C. Lee, and H. Kim, “Critical velocities for high speed particle deposition in kinetic spraying,” *Mater. Trans.*, vol. 47, no. 7, p. 1723, 2006.

[35] J. Anderson, *Modern Compressible Flow: With Historical Perspective*, 3 edition. Boston: McGraw-Hill Science/Engineering/Math, 2002.

[36] A. H. Shapiro, *The Dynamics and Thermodynamics of Compressible Fluid Flow, Vol. 1*, Volume 1 edition. New York: Wiley, 1953.

[37] J. A. Jr, *Hypersonic and High-Temperature Gas Dynamics, Second Edition*, 2 edition. Reston, Va: AIAA, 2006.

[38] E. Sansoucy, “Development of Aluminum-Based Coatings Produced by Cold Gas Dynamic Spraying.” May-2008.

[39] H. Katanoda, Y. Miyazato, M. Masuda, and K. Matsuo, “Pitot pressures of correctly-expanded and underexpanded free jets from axisymmetric supersonic nozzles,” *Shock Waves*, vol. 10, no. 2, pp. 95–101, May 2000.

[40] M. Grujicic, “9 - Particle/substrate interaction in the cold-spray bonding process,” in *The Cold Spray Materials Deposition Process*, V. K. Champagne, Ed. Woodhead Publishing, 2007, pp. 148–177.

[41] M. Grujicic, C. L. Zhao, W. S. DeRosset, and D. Helfritch, “Adiabatic shear instability based mechanism for particles/substrate bonding in the cold-gas dynamic-spray process,” *Mater. Des.*, vol. 25, no. 8, pp. 681–688, Dec. 2004.

[42] T. Hussain, D. G. McCartney, P. H. Shipway, and D. Zhang, “Bonding Mechanisms in Cold Spraying: The Contributions of Metallurgical and Mechanical Components,” *J. Therm. Spray Technol.*, vol. 18, no. 3, pp. 364–379, Sep. 2009.

[43] P. Richer, “Development of Conventional and Nanocrystalline Bond Coats by Cold Gas Dynamic Spraying for Aerospace Thermal Barrier Coatings.” Jan-2010.

[44] H. Assadi, F. Gärtner, T. Stoltenhoff, and H. Kreye, “Bonding mechanism in cold gas spraying,” *Acta Mater.*, vol. 51, no. 15, pp. 4379–4394, Sep. 2003.

[45] D. MacDonald, “Restoration of Aluminum Aerospace Parts and Coatings using Cold Gas Dynamic Spraying.” Apr-2014.

[46] “ASTM C 633-01: Standard Test Method for Adhesion or Cohesion Strength of Thermal Spray Coatings,” vol. 3, p. 7, Jul. 2001.

[47] C. R. C. Lima and J. M. Guilemany, “Adhesion improvements of Thermal Barrier Coatings with HVOF thermally sprayed bond coats,” *Surf. Coat. Technol.*, vol. 201, no. 8, pp. 4694–4701, Jan. 2007.

[48] “ASTM D4060-95: Standard Test Method for Abrasion Resistance of Organic Coatings by the Taber Abraser,” pp. 1–3.

[49] P. Trahan, “Corrosion Protection of Friction Stir Welded Al 7075 Panel for use in Aerospace Applications using Cold Gas Dynamic Spray.” May-2013.

[50] S. Yin, X. Suo, Z. Guo, H. Liao, and X. Wang, “Deposition features of cold sprayed copper particles on preheated substrate,” *Surf. Coat. Technol.*